The Dissertation Committee for Shirin Mozaffari
certifies that this is the approved version of the following dissertation:

Spin-Orbit Interaction and Kondo Scattering at the $PrAlO_3/SrTiO_3$ Interface: Effects of Oxygen Content

Committee:

John T. Markert, Supervisor

Alex De Lozanne

Alexander A. Demkov

Zhen Yao

John B. Goodenough

Spin-Orbit Interaction and Kondo Scattering at the $PrAlO_3/SrTiO_3$ Interface: Effects of Oxygen Content

by

Shirin Mozaffari

DISSERTATION

Presented to the Faculty of the Graduate School of

The University of Texas at Austin

in Partial Fulfillment

of the Requirements

for the Degree of

DOCTOR OF PHILOSOPHY

THE UNIVERSITY OF TEXAS AT AUSTIN

December 2017

To my family,

for their never-ending love and support

Acknowledgments

First and foremost, I would like to express my deepest gratitude to my advisor and mentor Prof. John T. Markert. I joined his group as a volunteer in 2010 and I was so fascinated by his wealth of knowledge, and the diversity and the profound physics underlying each experiment in his lab, that I stayed there since. His calm attitude toward solving problems, giving the students the freedom to find their own direction as scientists, and motivating them without being a micromanager is admirable. Thanks, Dr. Markert, for giving me the opportunity to work in your lab and learn from you; I have extremely enjoyed being your student, and I will forever be indebted to you.

I would like to express my gratitude to Mark Monti, who piqued my interest in oxide thin films early on. Mark was a tremendous mentor in teaching me a lot of skills necessary to run the experiments in the lab. I am grateful to all the members in the Markert's lab, especially Rosa Cardenas. Rosie was the first face I met at UT. She was extremely friendly to help me with everything when I just had come in. Isaac and Jeremy were always happy to help in any way possible. Dan Tennant was a great classmate and labmate to discuss physics with. I was so fortunate to meet and collaborate with Alex Rettie, who taught me a great deal about epitaxial thin films. Gregorio Ponti was amazingly helpful during my last year at UT. I would like to thank him for invaluable source of help while I was writing my thesis. Chatting with Madison Foreman, Aimee Sixta, and Derrick Morin made the experimental work in the lab so enjoyable.

I am especially thankful to Samaresh Guchhait and Rik Dey in Prof. Banerjee group for their help with the PPMS machine.

I would like to thank the members of my committee for being very nice to review my thesis on a very short notice. I would like to thank Prof. MacDonald and Prof. Shih for their funding to repair the PLD laser. I would like to thank Dr. Stacia Rodenbusch, the director Freshman Research Initiative (FRI) program for the financial support of our physics stream.

I have been blessed to be given a big head-start by having an incredible family. I am grateful for my parents for always giving me lots of love, enrichment, and independence. I couldn't have gotten to this point without their constant reassurance and helpful advice. Thank you both for raising me up to more than I could ever be and for every sacrifice you made for me to be where I am now. Words cannot describe the unconditional support of my lovely sister Maryam. I am extremely lucky to have you as my sister and my best friend. We never missed a day to talk to each other, even though we were thousands of miles away. Finally, I would like to thank my supportive husband Mehdi for setting a perfect example of a hard-working physicist and for all his help in physics since the first day we met at the University of Tehran.

Spin-Orbit Interaction and Kondo Scattering at the $PrAlO_3/SrTiO_3$ Interface: Effects of Oxygen Content

Publication No. _____

Shirin Mozaffari, Ph.D.
The University of Texas at Austin, 2017

Supervisor: John T. Markert

The broken translational symmetry at an interface between complex metal oxides gives rise to a number of remarkable phenomena with rich physics often due to charge, spin, orbital, or atomic reconstruction, such as superconductivity, metal-insulator transitions, and giant magnetoresistance. These phenomena can be entirely different from those innate to the constituent materials. A recent example of such interface phenomena is the two-dimensional electron gas (2DEG) at the interface of $LaAlO_3$ (LAO) and TiO_2-terminated $SrTiO_3$ (STO). Despite that LAO and STO are both band insulators and non-magnetic, their interface is found to be conductive, superconductive, ferromagnetic, and exhibits an electric-field tunable metal-insulator transition, which all are the result of electronic reconstruction at the interface. It is generally agreed that the electron gas is formed by transfer of electrons from the polar layers of LAO to the top TiO_2 layer of STO. In addition to the electronic reconstruction at the interface, doping the interface by interdiffusion of La/Sr atoms and by the presence of oxygen vacancies that are created in the STO substrate during thin film deposition contribute to the conductivity.

We examined, in detail, the effects of oxygen content on the electrical and magnetic properties of $PrAlO_3$ (PAO) on STO. Among the aluminates, PAO has the closest lattice constant to LAO (due to the multivalency of Ce, it is hard to make stable thin films of $CeAlO_3$), and thus this helps to lessen the effect of strain as much as possible. Also, the effective magnetic moment of the Pr^{3+} f electron states is 3.6 Bohr magnetons, due to often hybridized, while closed shell La^{3+} is diamagnetic, thus this rare-earth substitution can lead to magnetic properties in an aluminate structure. PAO is known to be paramagnetic in bulk and has mostly been studied for its structural transitions below room temperature which are absent in LAO. We report the effects of oxygen pressure during growth (P_{O_2}) on the electronic and magnetic properties of $PrAlO_3$ films grown on TiO_2-terminated $SrTiO_3$ substrates. Resistivity measurements show an increase in the sheet resistance as P_{O_2} is increased. The saturation of the sheet resistance down to 0.3 K is consistent with Kondo theory for $P_{O_2} \geq 10^{-5}$ torr. Resistivity data fits indicate Kondo temperatures of 16–18 K. For the 10^{-4} sample, we measured a moderate positive magnetoresistance (MR) due to a strong spin-orbit (SO) interaction at low magnetic fields that evolves into a larger negative MR at high fields due to the Kondo effect. Analysis of the MR data permitted the extraction of the SO interaction critical field for the $P_{O_2} = 10^{-5}$ torr interface (H_{SO} =1.25 T). We observed high positive MR for the least oxygenated sample, where a fraction of the n-type carriers are derived from oxygen vacancies and possible cation interdiffusion; for this 6×10^{-6} torr sample, Hall effect data indicate a thick conducting layer. Its extremely high MR ($\sim 400\%$) is attributed to classical behavior due to a distribution of mobilities.

Table of Contents

Acknowledgments **v**

Abstract **vii**

List of Tables **xii**

List of Figures **xiii**

Chapter 1. Introduction **1**

1.1 Interfaces of complex oxides 1

1.2 Novel phenomena at oxide interfaces 4

1.3 Outline of the thesis 7

Chapter 2. The $RAlO_3/SrTiO_3$ Interface **9**

2.1 Bulk ABO_3 perovskite compound 9

2.1.1 $SrTiO_3$ (STO) 11

2.1.2 $LaAlO_3$ (LAO) 14

2.1.3 $PrAlO_3$ (PAO) 15

2.1.4 Terraces and termination control of $SrTiO_3$ 17

2.2 The $LaAlO_3/SrTiO_3$ interface: 2D electron gas at the interface 18

2.3 Mechanism for interfacial conduction 20

2.3.1 The polarization catastrophe picture 20

2.3.2 Oxygen vacancies 23

2.3.3 Cation intermixing 25

2.4 Coexistence of superconductivity and magnetism 25

2.5 Spin-Orbit interaction 30

2.6 Weak Localization (WL) 34

2.7 Kondo mechanism 41

Chapter 3. Equipment and Characterization Techniques **43**
3.1 Pulsed Laser Deposition (PLD) . . . 43
3.1.1 Growth parameters . . . 45
3.2 Target preparation . . . 47
3.3 Surface analysis: Atomic Force Microscopy (AFM) . . . 49
3.4 Substrate preparation . . . 50
3.5 Structural characterization: X-Ray Diffraction (XRD) . . . 54
3.5.1 Profile measurement: Out-of-plane diffraction measurements . . . 56
3.5.2 X-Ray Reflectivity (XRR) measurement . . . 58
3.5.3 Rocking curve measurement . . . 60
3.6 Electrical transport measurements . . . 61

Chapter 4. Effects of Oxygen Content on the $PrAlO_3/SrTiO_3$ Interface **65**
4.1 Introduction . . . 65
4.2 $PrAlO_3$ thin films growth parameters . . . 66
4.3 Surface analysis of the $PrAlO_3$ thin films . . . 67
4.4 Crystal structure of the $PrAlO_3$ thin films . . . 67
4.5 Sheet resistance and Kondo effect . . . 69
4.6 Sheet carrier density and mobility . . . 74
4.7 Magnetoresistance and spin orbit interaction . . . 77
4.8 Summary . . . 83

Chapter 5. Multiband Conduction at the $PrAlO_3/SrTiO_3$ Interface **86**
5.1 Introduction . . . 86
5.2 Thin film fabrication and characterization . . . 87
5.3 Dependence of the sheet resistance on the magnetic field orientation . . . 87
5.4 Nonlinear Hall resistance . . . 89
5.4.1 Sheet carrier density and mobility using two-band model . . . 92
5.5 Anisotropy in magnetoresistance . . . 94
5.6 PAO/LAO/STO bilayers . . . 97

Chapter 6. Conclusions and Future Work **102**
6.1 Conclusions 102
6.2 Future work 103
6.2.1 Studying the role of magnetic moment of Pr 104
6.2.2 Studying the effect of mechanical pressure on the PAO/STO interface 104
6.2.3 Investigation of the superconductivity at the PAO/STO interface . . . 107

Bibliography **110**

Vita **128**

List of Tables

2.1 Summary of the physical properties of STO. 14

4.1 PLD parameters used in thin film growth of $PrAlO_3$ 66
4.2 Out-of-plane lattice constants for thin films of $PrAlO_3$ grown at different P_{O_2}. 69
4.3 Parameters obtained from fitting sheet resistance data of Fig. 4.3 to Eq. 4.1 and 4.2. 73
4.4 Parameters extracted from fitting the MR data in Fig. 4.6 to Eq. 4.8. 82

List of Figures

2.1 (a) Unit cell for crystal structure of a ABO_3 perovskite. (b) Visualization of the structure in terms of the BO_6 octahedra which share corners. (c) Layered structure (AO and BO_2) of the ABO_3 perovskite, along the (001) direction. . 11

2.2 The orbital hybridization of STO. The conduction band consists of Ti $3d$ orbitals. The valence band is mainly composed of the $2p$ orbitals of oxygen. [49] 12

2.3 (a) Superconducting transition temperature as a function of carrier concentration for $SrTiO_3$ [50]. (b) Hall mobility as a function of temperature for $SrTiO_3$ doped by Nb or oxygen vacancies [51]. 13

2.4 Energy levels of V_0 (neutral oxygen vacancy), V^+, and V^{++}, charged oxygen vacancies in (a) STO and (b) LAO with respect to maximum of the valance band (VBM) and minimum of the conduction band (CBM) [53]. 15

2.5 The sequence of structural transitions as a function of temperature for $PrAlO_3$ [52]. 15

2.6 Field cooled $M(H)$ curves of as-grown and annealed $PrAlO_3$ samples at $T = 5$ K after cooling the samples in the field of 50 kOe [56]. 16

2.7 Schematic of (a) an ideal (001) surface and (b) a step-terraced surface due to an inevitable miscut angle. The dashed line in (a) shows a typical miscut. . . 17

2.8 (a) Schematic representation of the two types of LAO/STO interfaces, AlO_2-LaO-TiO_2-SrO interface and LaO-AlO_2-SrO-TiO_2 interface respectively. (b) Resistance as a function of temperature for 26 unit cells thick LAO on STO substrates with a TiO_2-terminated surface and a SrO-terminated surface both grown at 850°C and 3×10^{-5} mbar oxygen pressure 19

2.9 Electrostatic model showing the polar catastrophe based on atomic layers taken as charged planes for an n-type interface. The left panel depicts a pristine interface, together with the charge density ρ, electric filed E, and electrostatic potential V, which tends to diverge with increasing LAO film thickness. The right panel shows the stabilized system for which 0.5 e per u.c. has been transferred from the surface layer to the interface. 21

2.10 (a) Temperature dependence of sheet resistance R_{xx} for interfaces grown at different P_{O_2}. (b) The dependence of carrier density at 2 K on the P_{O_2}. The sheet carrier density corresponding to 0.5 electrons per unit cell is denoted by the dashed line. [21] 24

2.11 (a) Sheet resistance as a function of magnetic field at 0.3 K for an LAO/STO interface grown at 10^{-3} mbar. The arrows indicate the direction of the measurements [69]. Hysteresis appears in the sheet resistance. (b) Direct imaging of magnetic dipoles using scanning SQUID microscope [71]. The ferromagnetic landscape appears as many static spatially separated dipoles. Inset: Scale image of the SQUID pick-up loop used to sense magnetic flux. (c) The magnetic field dependence of the torque curves of various test samples (cantilever only, bare STO substrate and the 0 u.c. sample) and an interface sample, taken at $T = 300$ mK. Inset: A schematic representation of the cantilever set-up [70]. 27

2.12 (a) Temperature dependence of the sheet resistance for the 8-u.c. and 15-u.c. samples, explained in the text. Inset: Sheet resistance versus temperature measured in 4–300 K. Superconductivity happens at $\cong$ 200 mK for the 8-u.c. sample [22]. (b) Sheet resistance versus temperature curves for magnetic fields applied perpendicular ($H_\perp$) and parallel ($H_{||}$) to the interface plane [73]. . . 28

2.13 Effect of SOC on the *orbital* motion of crystal electrons. 30

2.14 (a) Electron confined in x-y plane moving in a static an electric field $\vec{E}$. (b) In electron's frame of reference, Lorentz transformations generate magnetic field $\vec{B}'$ which depends linearly on velocity. 32

2.15 Band structure of t_2g orbitals in bulk $SrTiO_3$ calculated by (a) DFT and by (b) a tight binding model. In the absence of spin-orbit coupling, yz, zx, and xy are degenerate at the Γ point. SOC splits the sixfold-degenerate orbitals [80]. (c) Band structure for the 2DEG at the LAO/STO interface. Color-coded subbands are bands that are formed from the corresponding d orbitals shown above [84]. The figure is adapted according to Ref. [85]. 33

2.16 Schematic of different electronic transport regimes in solids. The open circles represent impurities and arrows shows the trajectories that electron traveled. 36

2.17 Schematic of WL and WAL in two dimensions in (a) magnetoconductivity, defined as $\delta\sigma \equiv \sigma(B) - \sigma(0)$, and (b) temperature dependence of the conductivity σ. B is the magnetic field and T is temperature. Adapted from Ref. [92]. 38

2.18 The magnetoresistance of a thin Mg- film at 4.5 K for different coverages with Au. The Au thickness is given in % of an atomic layer on the right side of the curves. The coating with Au increases the spin-orbit scattering. The points are experimental data and the full curves are obtained with the HLN theory. The ratio on the left side gives the strength of the adjusted spin-orbit scattering. It is essentially proportional to the Au-thickness. L_{00} is the universal conductance. 40

3.1 Schematic of pulsed laser deposition; Ota master thesis [108], modified. The image is not drawn to scale. 44

3.2 X-ray diffraction pattern of the polycrystalline $LaAlO_3$ (top panel) and $PrAlO_3$ (bottom panel) targets. $*$ shows the peak positions for the impurity phase of Pr_6O_{11}, which can be removed by grinding for longer times and annealing at higher temperatures. 47
3.3 Schematic of Atomic Force Microscopy. 49
3.4 (a) Schematic illustration of as as-received $SrTiO_3$ substrate; the termination is a mixture of SrO and TiO_2. (b) Schematic illustration of the desired TiO_2 termination which could be achieved by suitable chemical etching and thermal treatments. 50
3.5 (a) An AFM image of a terminated STO substrate (b) A line scan taken perpendicular to the terraces that verifies the unit cell step size between terraces, indicating single termination. (c) 3D AFM image of the substrate. 51
3.6 (a) and (b) Round deep features that sometimes appear at the edge of the terraces with large width. (c) Step bunching that is shown by a circle in the AFM image. 53
3.7 Schematic illustration of (a) the Rigaku Ultima IV, and (b) sample alignment, showing various angles and axis. The figures are taken from Rigaku website. 55
3.8 XRD data for thin films of PAO grown on STO. 57
3.9 A typical XRR spectrum. 59
3.10 XRR scans for PAO and LAO thin films with different thickness on STO. . . 59
3.11 A schematic illustration of rocking curve measurement. An epitaxial thin film produces sharp peak, whereas a non-epitaxial film produces wide peak. . . . 60
3.12 Rocking curve profile around the (001) peak for (a) PAO thin film and (b) STO substrate. The FWHM for the film and the substrate are 0.02° and 0.01°, respectively. 61
3.13 The two permutations that are used in the PPMS for determining the sheet resistance in the VDP configuration. 62
3.14 The configuration used to measure the Hall effect. To eliminated the effect of misalignments of contacts, the magnetic field was swiped from positive values to negative values. 64

4.1 AFM topography of the TiO_2-terminated STO substrate (a) before the film deposition and (b) after the PAO film deposition (PAO/STO). The film was grown at 1×10^{-4} torr. 67
4.2 (Color online) XRD data for PAO/STO samples grown at different oxygen pressures. The XRR pattern of the 10^{-3} torr sample is shown in the inset (blue symbols). The pink line is a simulation. 68
4.3 (Color online) Sheet resistance of PAO/STO interface synthesized at different oxygen pressure as a function of temperature. Solid curves are a fit using Eqs. 4.1 and 4.2. 71

4.4 Hall resistance as a function of magnetic field at 2 K for the interfaces prepared at (a) $P_{O_2} = 6 \times 10^{-6}$, (b) $P_{O_2} = 10^{-5}$ and $P_{O_2} = 10^{-4}$, and (c) $P_{O_2} = 10^{-3}$ torr. 74

4.5 (Color online) Sheet carrier density, n_s (a) and Hall mobility, μ (b) as a function of temperature. 76

4.6 (Color online) MR of PAO/STO interfaces at 2 K. The magnetic field is applied (a) out of the plane and (b) in the plane of the substrate. Insets show MR data for 6×10^{-6} torr sample. Solid curves are fits according to Eq. 4.8. 78

4.7 Dependence of magneto-conductance, expressed in units of $e^2/\pi h$, on magnetic field at 2 K for the 10^{-5} torr oxygen growth pressure sample for both field orientations. Black lines are fit to Eq. 4.7. 81

5.1 AFM images of PAO/STO thin films that were fabricated at (a) $P_{O_2} = 10^{-5}$ torr and (b) $P_{O_2} = 10^{-4}$ torr. This range of oxygen pressure during growth appears to have no effect on the topography of the samples. 87

5.2 Dependence of the sheet resistance on temperature, at different magnetic field directions for 15 monolayers of PAO on STO that were fabricated at (a) $P_{O_2} = 10^{-5}$ torr and (b) $P_{O_2} = 10^{-4}$ torr. The dotted lines distinguish the temperature regions where the magnetic field has a pronounce effect. 88

5.3 Hall resistance as a function of magnetic field for the $PrAlO_3/SrTiO_3$ interface: (a) $P_{O_2} = 10^{-5}$ torr sample and (b) $P_{O_2} = 10^{-4}$ torr sample, at different temperatures. The Hall data becomes distinctly nonlinear at $T = 20$ K and $T = 10$ K for the 10^{-4} torr sample. Black lines are fits to Eq. 5.2. 90

5.4 (a) Charge carrier densities n_1 and n_2, and (b) mobilities μ_1 and μ_2 for the 10^{-4} torr sample of $PrAlO_3/SrTiO_3$ (001). The values are obtained using a two-band model. The dotted lines are guides to the eye. 93

5.5 Arrhenius plot for the low population type of carriers. The line is an exponential fit to extract the band gap. 94

5.6 (a) Out-of-plane magnetoresistance for the 10^{-5} torr sample. (b) In-plane magnetoresistance for the 10^{-5} torr sample. Magnetic field and current are parallel. (c) In-plane magnetoresistance for the 10^{-5} torr sample. Magnetic field and current are perpendicular. (d) Out-of-plane magnetoresistance for the 10^{-4} torr sample. (e) In-plane magnetoresistance for the 10^{-4} torr sample. Magnetic field and current are parallel. (f) In-plane magnetoresistance for the 10^{-4} torr sample. Magnetic field and current are perpendicular. 95

5.7 Magneto-transport measurements for 15 unit celss of LAO on STO. The thin film was prepared at $P_{O_2} = 10^{-4}$ torr. (a) Sheet resistance as a function of temperature. (b) Hall resistance at 2 K. (c) Out-of-plane magnetoresistance ($MR_\perp$) at 2 K. (d) In-plane magnetoresistance ($MR_\parallel$) at 2 K, with magnetic field parallel (solid symbols) and perpendicular (open symbols) to the current. 98

5.8 magneto-transport measurements for 9 u.c. of PAO on top of 6 u.c. of LAO on STO, $PAO^{(9)}/LAO^{(6)}/STO$. The thin films were prepared at $P_{O_2} = 10^{-4}$ torr. (a) Sheet resistance as a function of temperature. (b) Hall resistance at 2 K. (c) Out-of-plane magnetoresistance ($MR_\perp$) at 2 K. (d) In-plane magnetoresistance ($MR_\parallel$) at 2 K, with magnetic field parallel (solid symbols) and perpendicular (open symbols) to the current. 100

5.9 (a) Sheet resistance as a function of temperature, (b) Hall resistance at 2 K, (c) out-of-plane magnetoresistance ($MR_\perp$) at 2 K, and (d) in-plane magnetoresistance ($MR_\parallel$) at 2 K, with magnetic field parallel and perpendicular (empty symbols) to the current for $LAO^{(15)}/STO$, $PAO^{(15)}/STO$, and $PAO^{(9)}/LAO^{(6)}/STO$ samples. 101

6.1 Picture of the chip carrier used for resistivity measurement under mechanical pressure for thin films. 106

6.2 Sheet resistance *vs.* temperature for PAO/STO interface for 0.5 kbar applied pressure. 106

6.3 XRD spectrum for different numbers of pulses of Ni on STO and on LAO/STO. 108

6.4 XRR patterns for 180 pulses of LAO on STO and 1200 pulses of Ni on the same thickness of LAO on STO. 109

6.5 AFM image of Ni/LAO/STO 109

Chapter 1

Introduction

1.1 Interfaces of complex oxides

Phenomena at surfaces and interfaces of solid materials have been of great interest to physicists, since the early theoretical work of Tamm [1] in 1932 and Shockley [2] in 1939. They showed that the surface of a semiconductor with a full bulk gap can possess metallic states. Since then, there have been many theoretical and experimental studies to utilize this effect, which resulted in revolutionizing our lives. Perhaps some of the most amazing examples of applying surface and interface physics are p-n junctions, Schottky contacts, and metal-oxide-semiconductor field-effect transistors (MOSFET), inside almost every every modern electronic device. The success of the semiconductor industry is not due to the bulk character of semiconducting materials; in fact, the device functionality is based on the transport of charge carriers along or across the interfaces between materials that have different doping levels.

The simplest interface is the sample surface. At surfaces and interfaces, where the dimensionality is reduced, the bulk electronic structure can change because the translational and rotational symmetry (if there is any) break; thus the atoms rearrange. This structural reconstruction compensates for the asymmetry in the forces experienced by the near-surface atoms and the changes in their chemical bondings. Moreover, point defects and dislocations

can also occur at the interface. All of these result in modifying the band structure and also result in a change in the electronic states at the surface or interface. Employing these effects at interfaces allows the design of semiconductor heterostructure devices.

Most of the current electronic devices are based on silicon-based or gallium-arsenide-based semiconductor technology. However, in the last two decades, another family of materials with remarkable functional properties that are unattainable in conventional semiconductors turned the focus of the research: the family of oxides, and in particular complex oxides. In fact, most materials naturally are in oxide form. Complex oxides are oxide compounds that contain two or more cations. Employing a transition metal in the oxide compound (transition metal oxide) could add more interesting physics to the vast zoo of physical properties already available in the oxide materials. Compared to conventional semiconductors, the bonds between the atoms in an oxide crystal tend to have a more polar nature, which means that the electrons have stronger interactions with each other; they are said to be correlated, meaning that the electrons could behave collectively in addition to individually. Moreover, different chemical elements can also be incorporated into the oxide crystals. This can tune the carrier density through doping, and also increases the flexibility in crystal composition.

From the simple binary monoxides to the more complex compounds, the oxide behaviors span a wide spectrum from insulating to semiconducting or metallic and superconductive, dielectric to ferroelectric, diamagnetic to ferromagnetic, and optically opaque to transparent. Besides, these properties can coexist and couple and result in multiple functionalities. Oxide interfaces, like their conventional semiconductor counterparts, offer the unique opportunity to control and enhance the effects by controlling the interaction between layers. This adaptability promises the application of bulk properties of oxides in smart electronic devices, and

in fact they already have earned their share in market of batteries, fuel cells, and information storage. However, the focus of this thesis in on the physics of interfaces between thin oxide films, where the surface and interface phenomena mentioned earlier come into play.

The interface is still a device! When Nobel laureate Herbert Kroemer [3] coined the famous phrase that "the interface is the device", he meant the amazing success of devices based on thin films of semiconductors used in photonic and electronic devices, that had started more than 40 years ago. Now we will have once again a similar revolution, this time for complex oxide interfaces. It is equally important in oxides to control and engineer the atomic, magnetic, and orbital symmetry at the interface. As will be discussed in the subsequent chapter, transition metal oxides host different kinds of order in their charge, spin, and orbital degrees of freedom. These order parameters meet together at the interface and are strongly affected by electronic processes such as charge-transfer, hybridization, and spin-orbital interactions, and they can lead to emergence of novel properties and functionalities.

The artificial fabrication of these interfaces is the first step to analyzing and ultimately to utilizing oxides. In fact, the properties of thin films can be totally affected by the quality of the interface. Physical Vapor Deposition (PVD) techniques such as Pulsed Laser Deposition (PLD) and Molecular Beam Epitaxy (MBE) are used for the epitaxial growth of metastable and artificial oxides. These compounds are stabilized by deposition on a lattice-matched substrate, with the control of the stacking sequence at the atomic level.

When the size of a sample is comparable to the characteristic length of its physical properties, novel phenomena can appear in the sample. The size effect can be more prominent when a transition metal is involved, often due to the interaction of electrons in the d-shell, and multivalancy. In the next section some of the experiments in which specific properties

of oxides were altered by bringing them together (heterostructures) are discussed.

1.2 Novel phenomena at oxide interfaces

The broken translational symmetry at an interface between complex metal oxides gives rise to a number of remarkable phenomena with rich physics often due to charge, spin, orbital, or atomic reconstruction, such as superconductivity [4], metal-insulator transitions [5, 6], and giant magnetoresistance [7]. These phenomena can be entirely different from those innate to the constituent materials [8, 9]. Some examples of these heterostructure that display amazing physics are briefly mentioned in the following.

Near the interface the inversion symmetry is broken, leading to a modified electronic structure distinct from the bulk. The essential feature of such symmetry breaking is the emergence of a nonzero electric field, which is absent in an otherwise inversion symmetric systems. When the electrons move in this electric field, they experience a magnetic field in their frame of motion. The coupling of the latter field to the electron's spin is dubbed as Rashba spin-orbit coupling [10, 11] and leads to spin non-degenerate electron bands near the interface. The exploration of Rashba spin-orbit coupling is now at the heart of the growing research field of spintronics that focuses on the manipulation of spins by the electrical current through the system [12].

The spin-orbit coupling can also lead to unconventional superconducting states at the interfaces. The corresponding pairing symmetries cannot be classified as conventional spin singlet and triplet states due to the lack of inversion symmetry near the surface. One example is the superconductivity in the epitaxial bilayer bismuth/nickel (Bi/Ni). The bulk rhombohedral crystalline bismuth is a semi-metal with small electron and hole pockets lo-

cated at high symmetry points in the Brillouin zone. In spite of low carrier density in Bi, the mean free path is extremely long [13]. The crystalline Bi remains in the normal state down to at least 10 mK [14]. However, a very recent experiment shows a bulk superconducting phase transition at extremely low temperature of about 0.5 mK [15] for pure Bi single crystals. A dramatic enhancement in superconducting critical temperature occurs in epitaxial bilayer bismuth/nickel [16], where a transition of 4 K is observed. Above the transition, in the normal state the majority of electron states near the Fermi energy are localized on the surface of the bismuth thin film [17, 18] with a strong Rashba spin-orbit coupling [18], leading to spin-split Fermi surfaces. Such Fermi surfaces, when coupled to the ferromagnetic fluctuations of nickel, give rise to exotic pairing states that breaks the time reversal symmetry spontaneously, and manifest itself in the optical Kerr measurements [19].

$BaCuO_2$ and $SrCuO_2$ both are not superconductors, but the artificially superlattice made by sequentially depositing the two materials superconduct at temperature as high as $\sim$ 50 K [20]. Bilayers consisting of La_2CuO_4 (an insulator) and $La_{1.55}Sr_{0.45}CuO_4$ (a metal) is a superconductor with T_c either 15 K or 30 K, depending on the layering sequence. The superconducting layer is confined within 2–3 nm of the interface. If the bilayer is exposed to ozone, T_c exceeds 50 K [4].

Perhaps, the most interesting example of these interface phenomena, which is the focus of this thesis, is the discovery of the two-dimensional electron gas (2DEG) at the interface of $LaAlO_3$ (LAO) and TiO_2-terminated $SrTiO_3$ (STO) [21] in 2004 by Ohtomo and Hwang. Despite that LAO and STO are both band insulators and non-magnetic, their interface is found to be conductive [21], superconductive [22], ferromagnetic [23] and exhibits electric-field tunable metal-insulator transition [24], which all are the result of electronic

reconstruction at the interface. It is generally agreed that the electron gas is formed by transfer of electrons from the polar layers of LAO to the top TiO_2 layer of STO [25]. In addition to the electronic reconstruction at the interface, doping the interface by interdiffusion of La/Sr atoms [26] and by the presence of oxygen vacancies that are created in the STO substrate during thin film deposition [27] contributes to the conductivity. In the electronic reconstruction model, donors ultimately originate from the surface of LAO. They come from the interface or within STO in the other two mechanisms. The reason for cation mixing is thought to be the reduction in the dipole energy at the interface, and it has been shown that $La_{1-x}Sr_xTiO_3$ ($0.05 < x < 0.95$) is metallic [26, 28]. It was also experimentally [29, 30] and theoretically [31, 32] demonstrated that varying oxygen pressure during growth results in dramatic changes in interfacial conductivity. Moreover, conductivity found at the interface of STO and amorphous LAO [33, 34] suggests that oxygen vacancies can be a dominant source of mobile carriers. Oxygen post-annealing of the amorphous samples fills the oxygen vacancies, and the interface becomes insulating. Thus, the interface electronic properties can be manipulated by the oxygen pressure during growth (P_{O_2}).

These findings encouraged us to examine the 2DEG at another aluminate interface. We studied $PrAlO_3/SrTiO_3$ (PAO/STO) interfaces that are fabricated at different P_{O_2}. Among the aluminates, PAO has the closest lattice constant to LAO (due to the multivalency of Ce, it is hard to make stable thin films of $CeAlO_3$), and thus this helps to lessen the effect of strain as much as possible. The effective magnetic moment of Pr is 3.6 Bohr magnetons, due to Pr^{3+} f electron states, often hybridized, while closed shell La^{3+} is diamagnetic [35], thus this rare-earth substitution can lead to magnetic properties in an aluminate structure. So, the main effort in this thesis is to study the effects of P_{O_2} on the PAO/STO

interface, which, unlike the LAO/STO interface, has an effective magnetic moment already present at the interface (due to Pr^{3+} f electrons).

1.3 Outline of the thesis

The focus of this thesis is to investigate the electric and magnetic properties of the 2DEG at the PAO/STO interface, that are grown at different P_{O_2}. The two compounds of PAO and STO belong to a family of materials that are called perovskites. A brief introduction to the perovskite family, their crystal structure, bulk electronic and magnetic properties are given in Chapter 2. A brief review of experimental studies on the 2DEG at the LAO/STO interface are also presented in Chapter Chapter 2. The last two sections in Chapter 2 are concerned with the effect of spin-orbit coupling and the Kondo mechanism at the LAO/STO interface.

The experimental work on fabricating PAO thin films using PLD are explained in Chapter 3. The chapter has sections concerning surface analysis of the samples using Atomic Force Microscopy (AFM) and studying the crystal structure of the samples using X-ray Diffraction (XRD). The results of oxygen pressure during growth on transport properties (electric and magnetic) are presented in the Chapter 4. We discuss the sheet resistance data in detail for the interfaces grown at different P_{O_2}, and provide some theoretical modeling. Hall effect measurement to define the types of the charge carriers and their mobilities at the interface is also done on the sample at a wide range of temperature. Magnetoresistance (MR) measurements as a function of temperature for both the out-of-plane and in-plane magnetic filed directions were done on the samples. Strong spin-orbit interactions at low magnetic fields in the MR data were observed for some of the samples. Analysis of the interaction

enabled us to quantify the spin-orbit interaction at oxide interfaces, which is expected to be substantial and is of current interest. Manifestation of the Kondo effect in some of the samples is quite clear in the MR data. The Kondo effect and its manifestation in various systems have always been the subject of sustained interest.

Finally, a summary of the important results and outcomes of the thesis, along with the outlook towards future work in this field, are given in Chapter 6.

Chapter 2

The $RAlO_3/SrTiO_3$ Interface

2.1 Bulk ABO_3 perovskite compound

The materials studied in this thesis belong to the family of perovskites oxides. An ideal Perovskite oxide is cubic with the general chemical formula of ABO_3, where A stands for a large cation, B for a small cation, and O is oxygen that bonds to both A and B. A halogen could also reside at the oxygen site. The chemical diversity of the perovskites is immense due to numerous element choices for the A and B sites, the non-stoichiometry of the cations, and the variation of the oxygen stoichiometry. In an ideal structure (with a lattice constant a), where the atoms touch each other, the A-O and B-O bond lengths are $a/\sqrt{2}$ and $a/2$. So, the relationship between the ionic radii is: $(r_A + r_O) = \sqrt{2}(r_B + r_O)$. It was found that the cubic structure is still held in ABO_3 compounds, even if this relation is not exactly followed. As a measure of the deviation from the ideal situation, a tolerance factor, $t = (r_A + r_O)/\sqrt{2}(r_B + r_O)$, was introduced by Goldschmidt. For an ideal perovskite t is unity. The perovskite structure is also found for t-values of $0.75 < t < 1.0$. If the A ion is smaller than the ideal value or if the B ion is too large, the tolerance factor becomes smaller than 1. Thus, the BO_6 octahedra will tilt to fill the space and the symmetry of the crystal structure will be lowered. An example is orthorhombic $CaTiO_3$ with $t = 0.82$. On the other hand, if A is a large ion or B is a small one, then t will be greater than 1 and a hexagonal packing of the structure is more stable, such as in $BaNiO_3$ ($t = 1.13$) [36]. Very few perovskites have t-

values very close to unity; distortions happen in many cases. ABO_3 compounds can condense into a large diversity of crystal structures. Cubic, orthorhombic, tetragonal, rhombohedral, and monoclinic structures have all been seen in perovskites. External parameters such as temperature and pressure can also induce structural phase transitions.

Another requirement, beside the tolerance facto, is charge neutrality. The charge distribution can be found in forms of $A^{1+}B^{5+}O_3^{2-}$, $A^{2+}B^{4+}O_3^{2-}$, or $A^{3+}B^{3+}O_3^{2-}$. Partial substitution of A and B sites, oxygen excess and vacancy, and cation nonstoichiometry can also occur in the ABO_3 compounds. Oxygen vacancies are more common than vacancies of cations. Oxygen excess nonstoichiometry is not as common.

The perovskite family exhibits many interesting physical properties such as ferroelectricity ($BaTiO_3$ [37]), ferromagnetism ($SrRuO_3$ [38]), antiferromagnetism ($LaCrO_3$ [39]), superconductivity ($YBa_2Cu_3O_7$ [40]), and transport properties of interest for high temperature thermoelectric power (La_2CuO_4 [41]). Thus, perovskites can show, amongst other properties, insulating, semiconducting, metallic, superconducting, magnetic, piezoelectric, ferroelectric, and multiferroic behavior.

The compounds studied in this dissertation, $SrTiO_3$, $LaAlO_3$, and $PrAlO_3$, belong to the class of perovskites. The cubic perovskite structure is shown in Fig. 2.1 (a). The unit cell drawn contains B ions at the corners, an A ion in the center, and O ions in the middle of the cube edges. As depicted in Fig. 2.1 (b) the structure can be described as a network of corner-sharing BO_6 octahedra.

For this study, Fig. 2.1 (c) is the most helpful description of the perovskite, particularly when the $LaAlO_3/SrTiO_3$ interface is introduced. Along the (001) direction

a perovskite can be viewed as alternating layers of AO and BO_2 that are stacked. In the proceeding sections, a brief review of the bulk properties of the constituent materials of this study, $SrTiO_3$, $LaAlO_3$, and $PrAlO_3$ will be discussed.

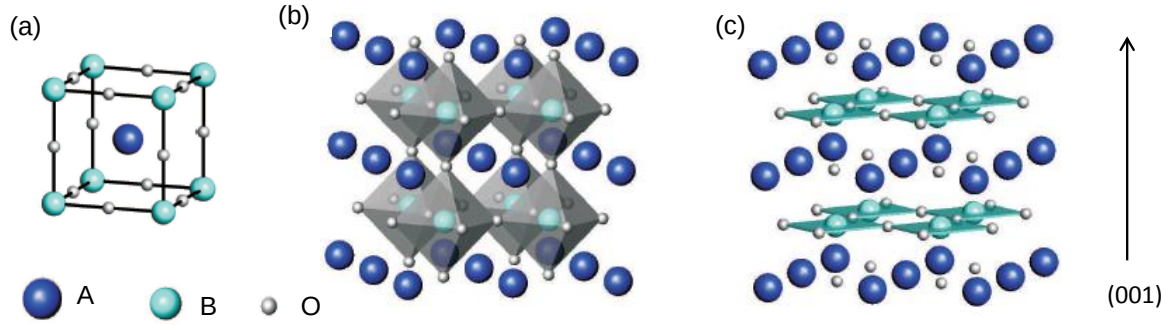

Figure 2.1: (a) Unit cell for crystal structure of a ABO_3 perovskite. (b) Visualization of the structure in terms of the BO_6 octahedra which share corners. (c) Layered structure (AO and BO_2) of the ABO_3 perovskite, along the (001) direction.

2.1.1 $SrTiO_3$ (STO)

Strontium titanate is one of the most studied perovskites. At room temperature, STO crystallizes in the cubic perovskite structure (space group $Pm\bar{3}m$) with a lattice parameter of 3.905 Å [42] and a density of $\rho = 5.12$ g/cm^3. STO undergoes a cubic to tetragonal phase transition around 100–110 K [43]. This transition happens through antiphase rotation of neighboring TiO_6 octahedra [44].

One can easily tune the transport properties of STO by introducing small compositional changes. For instance, substitution of La for Sr, or Nb for Ti [45], or

introduction of oxygen vacancies [46] can drive STO to be metallic. Stoichiometric STO is a band insulator with a wide indirect bandgap of 3.2 eV and a direct bandgap 3.75 eV, experimentally determined [47]. $2p$ orbitals of oxygens make the valence band, and Ti $3d$ orbitals compose the conduction band [47, 48]. In the cubic phase, the $3d$ orbitals split into t_{2g} and e_g [49], as shown in Fig. 2.2. Density Functional Theory (DFT) calculation of the band structure shows that the d_{xy}, d_{yz} and d_{xz} orbitals of the t_{2g} band are degenerate at the Γ point. The t_{2g} manifold splits further through spin-orbit coupling and antiferrodistortive transitions [48]. Stress and strain can tune the band structure as well. The details of the band structure are difficult to define experimentally due to the small energy scales involved.

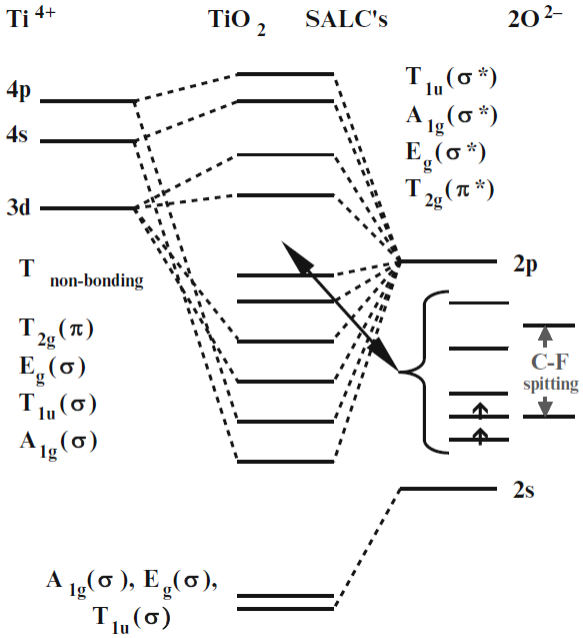

Figure 2.2: The orbital hybridization of STO. The conduction band consists of Ti $3d$ orbitals. The valence band is mainly composed of the $2p$ orbitals of oxygen. [49]

Superconductivity at ≤ 300 mK can be induced at STO, if the number of carriers is in the range of 10^{19}–10^{20} cm^{-3} [50], see Fig. 2.3 (a). At lower carrier densities the Hall mobility (μ) at low temperatures exceeds 10^4 cm^2/V $\cdot$ s [51], as shown in Fig. 2.3 (b).

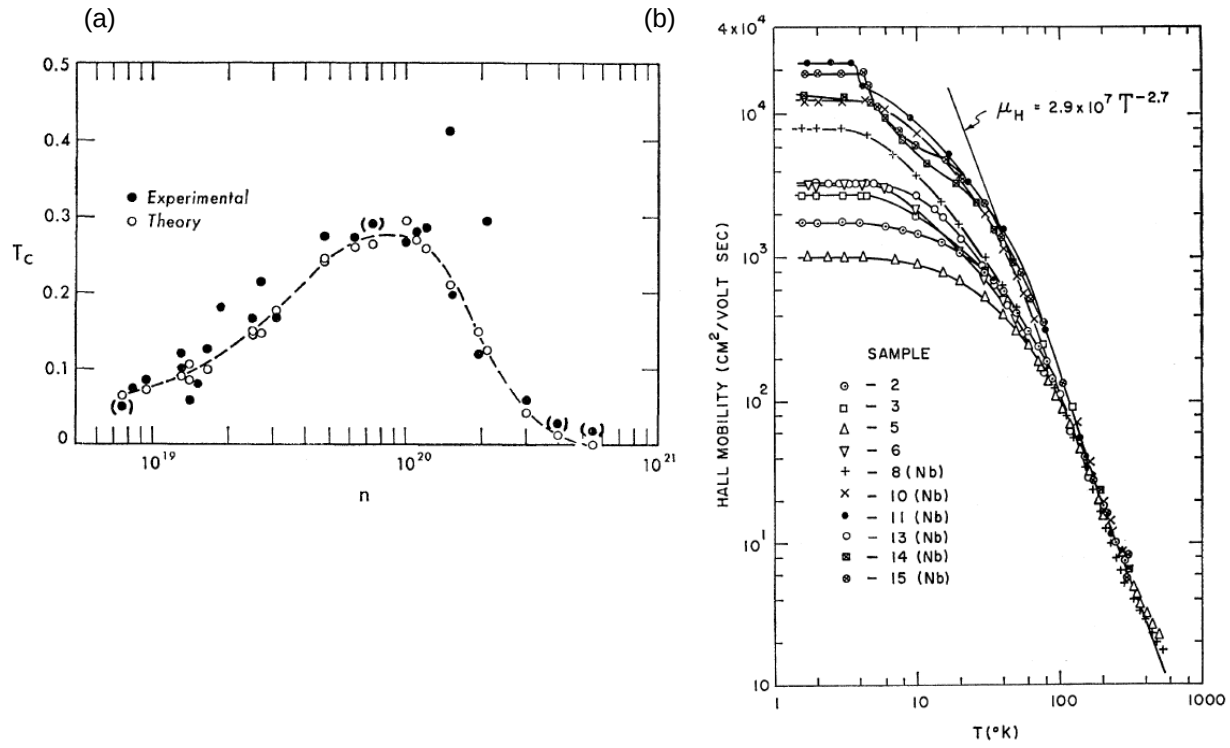

Figure 2.3: (a) Superconducting transition temperature as a function of carrier concentration for $SrTiO_3$ [50]. (b) Hall mobility as a function of temperature for $SrTiO_3$ doped by Nb or oxygen vacancies [51].

STO single crystals are transparent, sometimes with a slight yellowish hue. Small concentrations of oxygen vacancies give a greyish color STO. STO is widely used as a substrate for growing oxide thin films due to its lattice match with many oxides and its high

dielectric constant and diamagnetic nature. Some of the physical properties of STO are listed int the table below [42].

Table 2.1: Summary of the physical properties of STO.

Physical Property	Value
Lattice parameter at room temperature	3.905 Å
Bang Gap	3.2 eV
Mass density	5.12 g/cm^3
Dielectric constant	300
Thermal conductivity	6-12 W/m $\cdot$ K
Melting point	2080°C

2.1.2 $LaAlO_3$ (LAO)

At high temperatures $LaAlO_3$ has an ideal cubic crystal structure. At about 813 K, LAO undergoes a transition to a rhombohedral (trigonal) perovskite structure (space group is $R\bar{3}c$) [52]. At room temperature, the in-plane lattice constant of LAO is $a = 3.790$ Å [52].

LAO is also a band insulator with a large gap of 5.6 eV [54]. The wide bandgap and the fixed valance of La (unlike Ti in STO) make it almost impossible to induce conductivity in LAO. As can be seen from the theoretical calculation of the Mitra *et al.* [53] for LAO the oxygen vacancy creates a deep state 2.19 eV below the conduction band edge. Whereas, for STO the gap is 0.7 eV. Along the (001) direction LAO is composed of positively charged LaO and negatively charged AlO_2 planes. The small lattice mismatch between LAO and STO (about 3%) and their similar thermal expansion coefficients make it possible to grow LAO epitaxially on STO. Optically, LAO single crystals are transparent with yellowish hue.

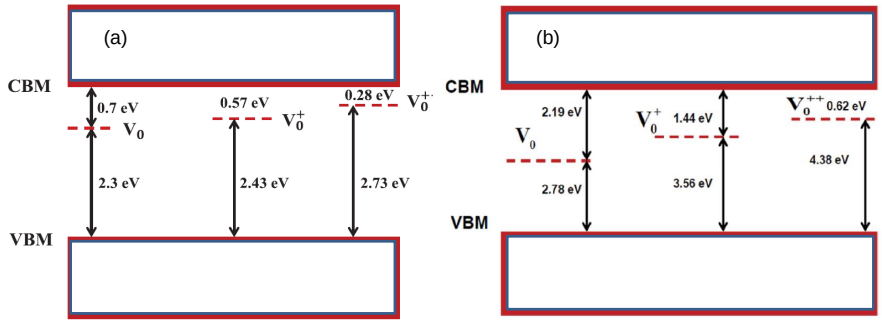

Figure 2.4: Energy levels of V_0 (neutral oxygen vacancy), V^+, and V^{++}, charged oxygen vacancies in (a) STO and (b) LAO with respect to maximum of the valance band (VBM) and minimum of the conduction band (CBM) [53].

2.1.3 $PrAlO_3$ (PAO)

The main goal of this thesis is to study the transport properties of thin films of $PrAlO_3$. $PrAlO_3$ is also a perovskite, and among the aluminate perovskites, $PrAlO_3$ is one of the most studied compounds, mainly because of its structural transitions below room temperature, which are absent in most of the similar compounds. In spite of all the studies, the exact temperature at which the transition happens and the space group of the structure are not completely resolved, yet.

		120 K		150 K		205 K		1320 K	
Phase	**V**	→	**IV**	→	**III**	→	**II**	→	**I**
Symmetry	Tetragonal		Monoclinic		Orthorhombic		Trigonal		Cubic

Figure 2.5: The sequence of structural transitions as a function of temperature for $PrAlO_3$ [52].

At room temperature bulk PAO is rhombohedral with the space group of $R\bar{3}c$, and

with an in-plane lattice parameter of 3.77 Å [52]. It transforms to an orthorhombic structure upon lowering the temperature to about 205–225 K, and to a monoclinic structure at about 151–175 K. Fig. 2.5 shows the structural transitions sequence for PAO. The temperature dependencies of the lattice parameters of PAO are shown in Fig. 2.5.

PAO is known to be paramagnetic in bulk [55, 56]. Pr ions comes into two valences: Pr^{3+} and Pr^{4+}. As-grown crystals of PAO are dark brown due to the presence of Pr^{4+} ions. One of the starting materials in making PAO crystals is Pr_6O_{11}, which is the mixed valence praseodymium oxide and has the same coloration. After annealing in a reducing atmosphere the color change to light green, which is the typical color of Pr^{3+} doped crystals. The field cooled magnetization curves at $T = 5$ K for an annealed and an as-grown samples are shown in Fig. 2.6.

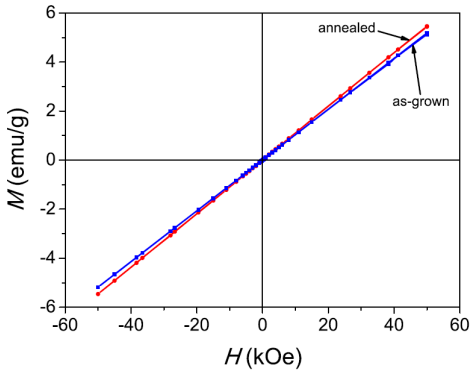

Figure 2.6: Field cooled $M(H)$ curves of as-grown and annealed $PrAlO_3$ samples at $T = 5$ K after cooling the samples in the field of 50 kOe [56].

2.1.4 Terraces and termination control of $SrTiO_3$

The ideal (001) surface is a *perfect* plane (see Fig. 2.7 (a)). In practice, that perfect plane hardly exists; the (001) surface has an inevitable deviation from a perfect cut, a miscut, which results in a step-terrace structure (see Fig. 2.7 (b)). Terraces tend to be unit-cell-sized (3.904 Å). Depending on the miscut angle, the width of terraces varies. Typical miscut angles are between $0.05° - 0.3°$, which lead to terraces widths of about 70–500 nm. The substrate used in this thesis is (001) oriented single-crystalline STO. The substrates were bought from MTI in the USA or CrysTec in Germany. As was mentioned earlier, STO along the (001) direction can be viewed as an alternating stack of SrO and TiO_2. An as-received STO substrate has a mixed termination of AO and BO_2 (not well defined terraces), which often are not possible to see under an Atomic Force Microscope. The specific termination of Sr-site or Ti-site on the substrate surface has a crucial effect on its electronic properties. Usually, a specific termination is achieved by suitable chemical etching and thermal treatments. Details of the treatment methods to achieve a pure TiO_2 termination for STO (which is the desired termination for this thesis) are discussed in the subsequent chapter. To make STO terminated by SrO, one needs to deposit one atomic layer of SrO on a TiO_2 terminated STO. This could be done in the chamber just before growing the desired thin film.

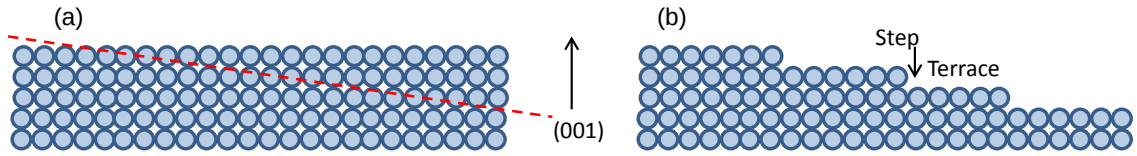

Figure 2.7: Schematic of (a) an ideal (001) surface and (b) a step-terraced surface due to an inevitable miscut angle. The dashed line in (a) shows a typical miscut.

The effects of the miscut angle (and thus the width of terraces) on the electronic properties of the LAO/STO interface is still under study. Fix *et al.* [57] have studied samples grown on substrates with miscut angles ranging from $0.2^\circ - 8^\circ$, and reported an enhancement of the mobility for larger miscut substrates; a higher mobility, but with roughly a third of carrier concentration, was observed for the samples with a miscut angle of 8°, at 10 K. They suggest that the terraces may act as traps for low-mobility carriers. Fix *et al.* have not seen any influence of the current direction in the Van der Pauw measurement for resistivity. On the other hand, Brinks *et al.* [58] have seen anisotropic resistance for different transport directions. They suggested that the observed anisotropy is due to the difference in transport along or perpendicular to the terrace direction.

2.2 The $LaAlO_3/SrTiO_3$ interface: 2D electron gas at the interface

In 2004, Ohtomo and Hwang [21] showed that when thin films of $LaAlO_3$ are deposited onto a TiO_2-terminated $SrTiO_3$ (001) substrate, a high mobility electron gas forms at the interface. Their report of the emergence of conductivity at the interface of two insulators has motivated a tremendous amount research on the oxide interfaces. When depositing LAO on STO, two different interfaces can be prepared based on the termination of STO. If STO is terminated by TiO_2, the stacking at the interface is LaO/TiO_2 and it is called an n-type interface. On the other hand, if STO is terminated by SrO, the stacking at the interface is SrO/AlO_2 and it is called a p-type interface. It turns out that only the n-type interface is conductive. A schematic of these two interfaces is illustrated in Fig. 2.8 (a). The details of the difference between the electronic structures of the two interfaces are described in the subsequent section. Figure 2.8 (b) shows a typical observation of the conductivity at the

interface LaO/TiO_2 and insulating behavior at the AlO_2/SrO interface [59].

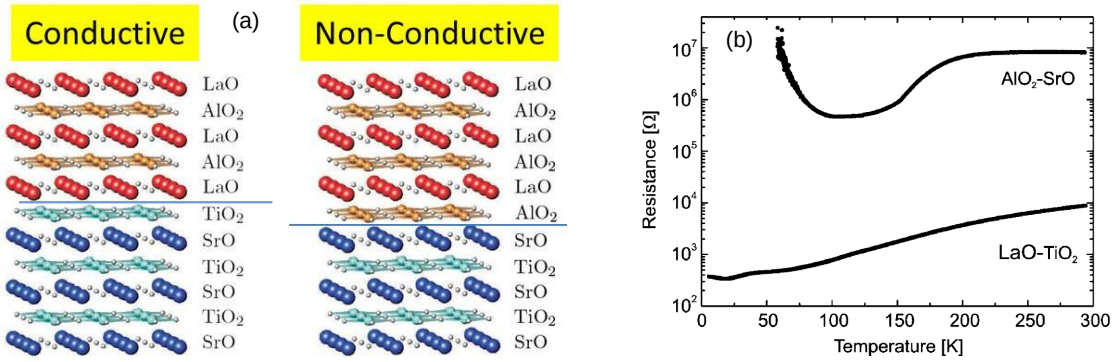

Figure 2.8: (a) Schematic representation of the two types of LAO/STO interfaces, AlO_2-LaO-TiO_2-SrO interface and LaO-AlO_2-SrO-TiO_2 interface respectively. (b) Resistance as a function of temperature for 26 unit cells thick LAO on STO substrates with a TiO_2-terminated surface and a SrO-terminated surface both grown at 850°C and 3×10^{-5} mbar oxygen pressure [59].

It should be noted that a 2DEG can also be formed on the surface of $SrTiO_3$ by cleaving it in vacuum. Interested readers can follow the results from Santander-Syro *et al.* [60].

Conductivity has also been observed at the (110)- and (111)-oriented LAO/STO interfaces [61]. The (001)- and (111)-oriented interfaces have the polar discontinuity, but the (110)-oriented interface does not have any polar discontinuity. So, the observation of conductivity at the LAO/STO interfaces with the (110)-orientation is very interesting. Amorphous LAO/STO interfaces are also found to be conductive [33, 34].

2.3 Mechanism for interfacial conduction

2.3.1 The polarization catastrophe picture

From the beginning of the discovery of conductivity at the LAO/STO interface, the polar catastrophe picture was the primary mechanism for the conductivity. This picture is more understandable if we take into account the layered structure of the film and the substrate. Along the (001) direction, LAO is polar and composed of positively charged layers of $(LaO)^{+1}$ and negatively charged layers of $(AlO_2)^{-1}$. In a simple picture, LAO is like a capacitor made up of $+e$ and $-e$ plates (e is the electric charge). There is an electric field E and thus a potential V across each plate of this capacitor. STO, however, is composed of neutral planes of $(SrO)^0$ and $(TiO_2)^0$. Thus, by deposition of LAO, one joins neutral layers of the substrate to the charged layers of the film at the interface. Such charge discontinuity has consequences which were first discussed for heterojunctions of Ge/GaAs semiconductors by Baraff *et al.* [62] (Ge is a non-polar material, while GaAs is polar). Their idea, which is known as the "*Polar Catastrophe*" picture, was later applied for explanation of the conductivity at the LAO/STO interface by Nakagawa *et al.* [25]. In an n-type interface, the depositions of $LaAlO_3$ layers on $SrTiO_3$ is similar to building up a series of capacitors on top of the substrate; the potential across each capacitor is additive and diverges as the film thickness increases, as schematically is shown in Fig. 2.9.

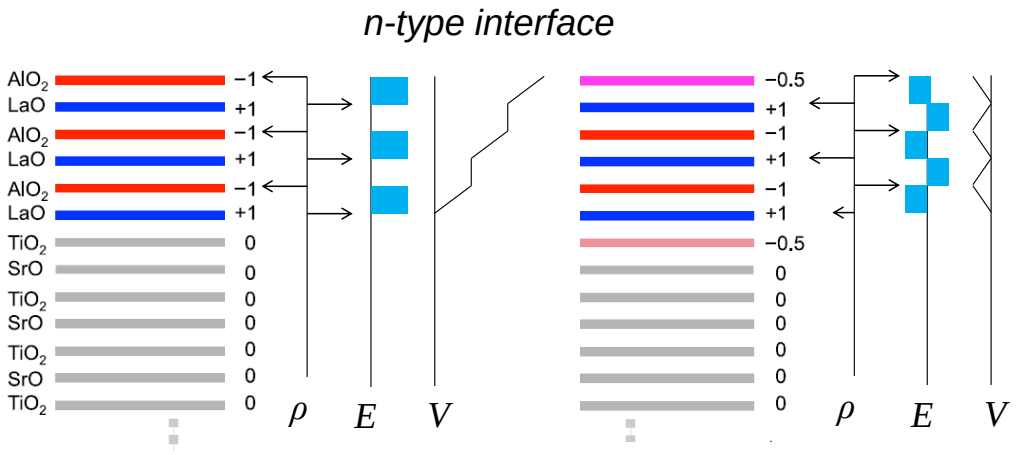

Figure 2.9: Electrostatic model showing the polar catastrophe based on atomic layers taken as charged planes for an n-type interface. The left panel depicts a pristine interface, together with the charge density ρ, electric filed E, and electrostatic potential V, which tends to diverge with increasing LAO film thickness. The right panel shows the stabilized system for which 0.5 e per u.c. has been transferred from the surface layer to the interface.

In a conventional semiconductor, the structure avoids this diverging potential by re-arranging ions across the interface which causes roughening of the interface (the so called atomic reconstruction). But, in an LAO/STO interface, another option is available at the interface, and that is made possible by the mutltivalency of Ti. To balance the charge discontinuity, half of the electron (or, practically, one electron in every other unit cell) from the LAO surface valence bands (oxygen $2p$ bands) is transfered to the STO conduction bands (Ti $3d$ t_{2g} bands). To accommodate that half electron, the average valency of the Ti atom at the interface changes from Ti^{4+} to $Ti^{3.5+}$. It turns out that it is more energetically favorable for the system to rearrange charges rather than ions. By this charge reconstruction the potential no longer diverges. That half electron at the n-type interface is the source of

conductivity and the terminology of n-type is related to that. Experiments also confirm the existence of that extra electron at the interface [25].

Charge discontinuity (with opposite sign) and the resulting diverging potential also happens for the p-type interface. Similarly, the system removes half of an electron from the SrO plane (effectively doping half a hole). However, there are no multivalence transition ion is available. So, to accommodate that extra hole, some of the oxygen ions at the interface are removed. Experiment results have shown that holes at the p-type interface are not mobile and do not result in conductivity [25].

Studies by Thiel *et al.* [63] in a series of samples that are grown at 10^{-4} mbar (7.5×10^{-5} torr) followed by some post annealing, show that the conductivity happens for the interfaces where the LAO thickness is equal to or above 4 unit cells (u.c.), suggesting that the measured conductivity has some intrinsic origin.

The polar discontinuity scenario is successful in explaining some of the observed experimental results. But there are some experimental results that question the full validity or applicability of the polar catastrophe mechanism. For instance, the number of charge carriers predicted by the polar discontinuity model is 3×10^{14} cm^{-2}, while the reported Hall measurement data are generally an order of magnitude lower. It is suggested that there are two types of electrons at the interface; one population is tightly bound to the interface and is strongly localized due to defects, while the other population is mobile [64].

Another example is the discrepancy between the values reported for the critical thickness for the emergence of the conductivity. Originally, it was reported that 4 u.c. of LAO is necessary for the emergence of the conductivity, while other predict 5 u.c. [65]. This

group explains the conductivity as a crossover of the LAO valence band maximum and STO conduction band minimum. At 5 u.c., the valence band at the LAO surface crosses the STO conduction band and the charges are transferred to the interface.

Two other experiments which really debate the validity of the polar catastrophe scenario are the emergence of the conductivity for amorphous LAO [33, 34], and conductivity at the (110)-oriented interface, which is the nonpolar direction [61].

These results can be explained more easily if we accept other contributions to the interface conductivity. The other main contributions to the conductivity are oxygen vacancies and intermixing of the cations.

2.3.2 Oxygen vacancies

Oxygen vacancies V_O could be a source of n-type carriers at the interface. Each oxygen bonds to two electrons; thus V_O could dope electrons into the system. In the case of LAO/STO interface, the concentration of V_O is a function of the oxygen pressure during growth P_{O_2}. In fact, from the early studies on LAO/STO interface [21], it was clear that P_{O_2} has a crucial role on the modulation of the conductivity.

The resistivity behavior and the number of the charge carriers at the interfaces that are grown at different P_{O_2} differ significantly. If the thin films are grown at low P_{O_2} ($P_{O_2} \lesssim 10^{-5}$ torr), the number of sheet carriers n_s can be as high as 10^{17} cm^{-2}, which is much higher than the interfacial amount predicted by polar catastrophe scenario (10^{14} cm^{-2}). The sheet resistance of the interfaces that are prepared at low P_{O_2}, can be as low as $\sim 10\ \Omega/\square$ at room temperature. Whereas, interfaces that are grown at higher P_{O_2} [29, 30] have much higher sheet resistance at room temperature ($\sim 10 - 100$ k$\Omega/\square$). It is also theoretically [31, 32]

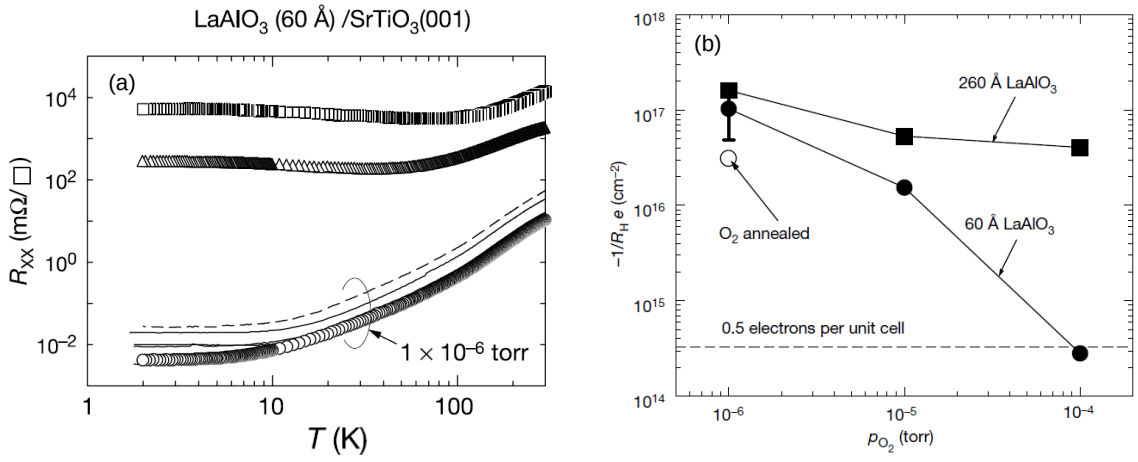

Figure 2.10: (a) Temperature dependence of sheet resistance R_{xx} for interfaces grown at different P_{O_2}. (b) The dependence of carrier density at 2 K on the P_{O_2}. The sheet carrier density corresponding to 0.5 electrons per unit cell is denoted by the dashed line. [21]

demonstrated that varying oxygen pressure during growth results in dramatic changes in interfacial conductivity.

Moreover, conductivity found at the interface of STO and amorphous LAO [33, 34] suggests that oxygen vacancies can be a dominant source of mobile carriers. Oxygen post-annealing of the amorphous samples fills the oxygen vacancies, and the interface becomes insulating.

All of these results can be justified more easily, if we accept that some of the carriers are doped into the interface during the thin film growth. In fact, the main idea of this thesis is to highlight the role of oxygen vacancies in the emergence of conductivity.

Oxygen vacancies should not be considered as the sole mechanism for the conductivity; Electron Energy Loss Spectroscopy (EELS) experimental results [66] suggest that the

observed charge densities are much higher than the amount which could have originated from oxygen vacancies. Another reason that we should not solely consider the conductivity stemming from oxygen vacancies is their inability to explain the critical thickness of 4 u.c.

2.3.3 Cation intermixing

A third possible source of electrons for the 2DEG at the LAO/STO interface is interdiffusion. Some studies, such as Electron Energy Loss Spectroscopy (EELS) [25] and Surface X-ray Diffraction (SXRD) [67], suggest that doping the interface by interdiffusion of La/Sr atoms [26] that are created in the $SrTiO_3$ substrate during $LaAlO_3$ deposition contributes to the conductivity. When the La^{3+} replaces Sr^{2+}, the valence of the titanium has to change to Ti^{3+}, which results in electron doping. The reason for cation mixing is thought to be the reduction in the dipole energy at the interface, and it has been shown that $La_{1-x}Sr_xTiO_3$ ($0.05 < x < 0.95$) is metallic [26, 28]. However, there are some experimental results that do not support this mechanism; such as intentional delta doping with Cd and Mn [68], which does not result in interfacial conductivity.

In the electronic reconstruction model, donors ultimately originate from the surface of LAO. They come from the interface or within STO in the other two mechanisms.

2.4 Coexistence of superconductivity and magnetism

The existence of magnetism at the LAO/STO interface is perhaps one of the most surprising phenomena of this system. $SrTiO_3$ and $LaAlO_3$ are both non-magnetic materials, so the first report of magnetism [69] was quite fascinating. Hints of magnetism at the LAO/STO interface was first discovered in 2007 through observation of hysteresis in the

magnetoresistance and of a characteristic Kondo-like minimum in the resistivity *vs.* temperature curve [69]. Magnetoresistance hysteresis is usually indicative of ferromagnetic domain formation in which domains change polarity above a certain coercive field. Later, torque magnetometry measurement [70] proved that the magnetism ($\sim 0.3\mu_B$ per interfacial unit cell) is present all the way to 200 K. In 2011, scanning SQUID microscopy [71] directly imaged the ferromagnetism, and it was found that magnetism exists in heterogeneous dipole-like ferromagnetic patches. The spatial distribution of the patches are highly non-uniform. The magnitude and the size of the magnetization were found to change from patch to patch. The evidence of magnetism has been seen in X-ray Magnetic Circular Dichroism (XMCD) [23], as well. The reported magnetization is $\sim 0.01\mu_B$ at $T = 3 - 10$ K, and was suggested to be related to oxygen vacancies, because samples with higher concentration of oxygen vacancies showed a stronger XMCD signal. Other references such as Ref. [72] relate the magnetism to the d_{xy} orbital of Ti^{3+}. Similar to the conductivity, the magnetism only occurs when the LAO film is thicker than a few unit cells. In contrast to conductivity, magnetism is seen at SrO-terminated surfaces, too. A summary of the reported magnetic measurements is shown in Fig. 2.11.

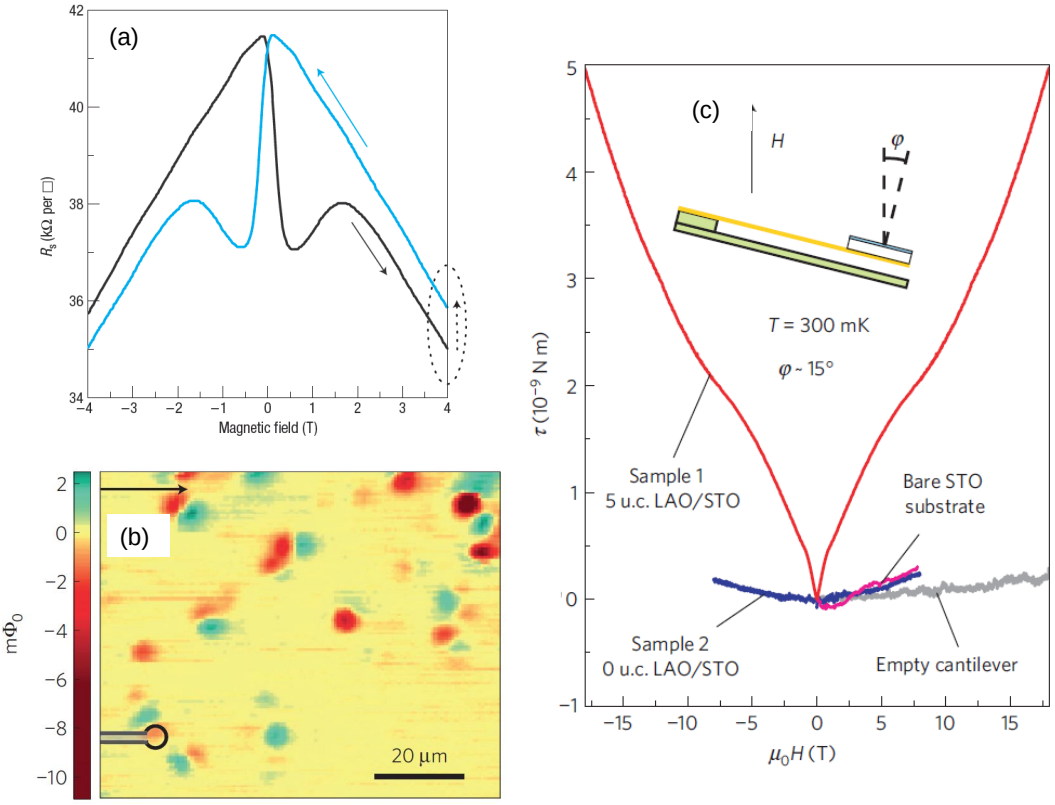

Figure 2.11: (a) Sheet resistance as a function of magnetic field at 0.3 K for an LAO/STO interface grown at 10^{-3} mbar. The arrows indicate the direction of the measurements [69]. Hysteresis appears in the sheet resistance. (b) Direct imaging of magnetic dipoles using scanning SQUID microscope [71]. The ferromagnetic landscape appears as many static spatially separated dipoles. Inset: Scale image of the SQUID pick-up loop used to sense magnetic flux. (c) The magnetic field dependence of the torque curves of various test samples (cantilever only, bare STO substrate and the 0 u.c. sample) and an interface sample, taken at $T = 300$ mK. Inset: A schematic representation of the cantilever set-up [70].

Superconductivity at the LAO/STO interface was first seen by Reyren *et al.* [22] in

2007. Their samples were prepared by depositing of LAO layers with thicknesses of 2, 8, and 15 u.c. on (001) TiO_2 terminated-STO. The films were grown by pulsed laser deposition at 770°C and in P_{O_2} of 6×10^{-5} mbar (4.5×10^{-5} torr), then cooled to room temperature in 400 mbar of O_2, with a 1-hour oxidation step at 600°C. The 2-u.c.-thick sample turned out to be an insulator (resistance ≥ 30 MΩ) at all temperatures T (32 mK $< T <$ 300 K). The 8-u.c. and 15-u.c.-thick samples superconduct at $\cong$ 200 mK and 100 mK, as shown in Fig. 2.12 (a). The width of the transition is higher for the 8-u.c. sample. The 8-u.c. sample did not show neither a minimum in the $R(T)$ characteristics nor a hysteretic magnetoresistance. Whereas, for the 15-u.c. sample, a shallow minimum in the $R(T)$ curve was observed at 4 K.

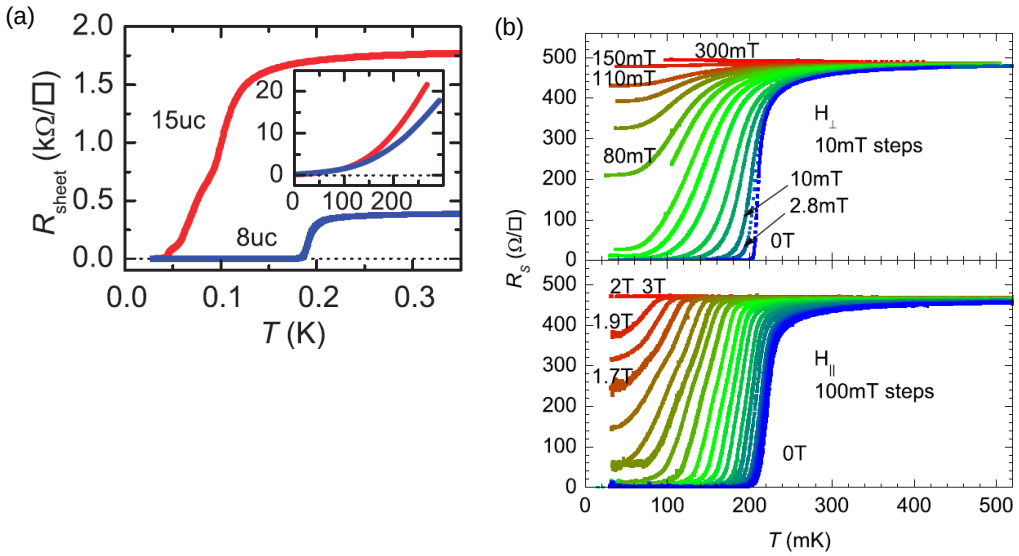

Figure 2.12: (a) Temperature dependence of the sheet resistance for the 8-u.c. and 15-u.c. samples, explained in the text. Inset: Sheet resistance versus temperature measured in 4–300 K. Superconductivity happens at $\cong$ 200 mK for the 8-u.c. sample [22]. (b) Sheet resistance versus temperature curves for magnetic fields applied perpendicular ($H_\perp$) and parallel ($H_{||}$) to the interface plane [73].

The superconducting critical magnetic field H_c, perpendicular and parallel to the interface was measured in Ref. [73]; strong anisotropies for fields applied in- and out-of-plane were measured, as can been seen in Fig. 2.12 (b). In the perpendicular direction, a magnetic field of ∼150 mT suppresses the superconductivity; whereas, for parallel direction, the width of the transition is relatively unaffected by fields up to 1.3 T. Such anisotropy confirms the 2D nature of the superconductivity. The thickness of the superconducting layer was measured to be ∼ 10–50 nm [73]. The coherence length was estimated to be 50–100 nm, through the analysis of the critical perpendicular field within the Ginzburg-Landau theory [73].

The ∼300 mK transition temperature for the 2DEG at the LAO/STO interface falls in the T_c range of oxygen-deficient $SrTiO_{3-x}$. A superconducting dome as a function of carrier density [24] has been observed with a maximum $T_c \sim 300$ mK, which is close in value to that observed in the bulk STO. To add to the complexity of the problem, it also has been reported that the application of the in-plane magnetic field increases the superconducting temperature [74]. The electron pairing may originate from the bulk $SrTiO_3$, such as the proposed BCS-pairing due to the LO (longitudinal optical) phonons of $SrTiO_3$ [75]. Other exotic mechanisms of pairing, such as d-wave pairing in the electron-electron interactions between itinerant and localized electrons across the interface [76], and topological superconductivity in the d_{xy}/d_{yz} band from particle-hole fluctuations, have also been proposed [77].

Coexist of magnetism and superconductivity in nature is rare and very remarkable. Whether the magnetism and superconductivity at the LAO/STO interface occur in separated regions of the sample or within a same region is yet to be understood.

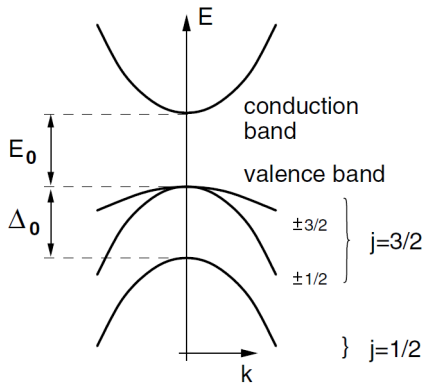

Figure 2.13: Effect of SOC on the *orbital* motion of crystal electrons.

2.5 Spin-Orbit interaction

The Spin-Orbit (SO) interaction is an interaction between the spin of a particle with its motion. This kind of coupling exists naturally in atomic systems, and comes with the Hamiltonian of $H_{SO} \sim \vec{L} \cdot \vec{S}$, where $\vec{L}$ is orbital angular momentum and $\vec{S}$ is the spin angular momentum. SO coupling has a very profound effect on the energy band structure; In semiconductors such as GaAs, SO coupling gives rise to a splitting of the topmost valence band. Fig. 2.13 schematically shows that by taking SOC into account for electron states, we obtain electronic states with angular momentum $j = 3/2$ and $j = 1/2$, that are split in energy by a SO gap Δ_0 [78]. Systems with high $\vec{L}$ and large spin are expected to have strong spin-orbit coupling.

Before focusing on the effects of SO coupling on interfaces, it is important to understand its origin. To begin, consider an electron with mass m, charge e, and momentum $\vec{p}$ that moves in an external magnetic field $\vec{B}$. This electron experiences a Lorentz force perpendicular to its motion $\vec{F} = -\frac{e}{m}\vec{p} \times \vec{B}$ with Zeeman energy $U = -\mu_B \vec{\sigma} \cdot \vec{B}$, where $\vec{\sigma}$ and

μ_B are the Pauli spin matrices and the Bohr magneton, respectively. By analogy, when this electron moves in an electric field $\vec{E}$, it experiences a magnetic field $\vec{B}_{eff} \sim \frac{1}{mc^2}\vec{E} \times \vec{p}$ in its rest-frame, where c is the speed of light. This magnetic field induces a momentum-dependent Zeeman energy, which is the same as atomic SO coupling $H_{SO} = \frac{\mu_B}{mc^2}(\vec{E} \times \vec{p}) \cdot \vec{\sigma}$. As it seems, SO interactions are the relativistic correction to the Schrödinger equation for electrons.

Mainly, there are two types of SO interactions in solids: a symmetry independent type that exists in crystals and stems from SO interaction in atomic orbitals, and a symmetry dependent SO coupling that exists in crystals without inversion symmetry.

In crystals, the electric field is given by the gradient of the crystal potential $\vec{E} = -\vec{\nabla}V$, which produces a SO energy of $\frac{\mu_B}{mc^2}(-\vec{\nabla}V \times \vec{p}) \cdot \vec{\sigma}$, with the SO field of $\vec{w}(\vec{p}) = -\frac{\mu_B}{mc^2}(-\vec{\nabla}V \times \vec{p})$. Because SO coupling preserves time-reversal symmetry $[\vec{w}(\vec{p}) \cdot \vec{\sigma} = -\vec{w}(-\vec{p}) \cdot \vec{\sigma}]$, the SO field must be odd in electron momentum $\vec{p}$; that means, $\vec{w}(-\vec{p}) = -\vec{w}(\vec{p})$. Only structures, such as zinc-blende III-V semiconductors, that lack inversion symmetry can accommodate this odd-in-momentum SO field. The lack of inversion symmetry in the bulk leads to a spin splitting, and it was first noticed by Dresselhaus [79] and thus is called the Dresselhaus SO interaction.

Surfaces and interfaces such as in 2D materials can also induce asymmetry. The SO coupling in these cases is a combined effect of atomic SO coupling and asymmetry of the potential in the direction perpendicular to the 2D plane. This effect is named in honor of Emmanuel Rashba [10] who discovered it. The Rashba effect is a manifestation of SO interaction in solids, where spin degeneracy associated with the spatial inversion symmetry is lifted due to a symmetry-breaking electric field normal to the heterointerface. In general, the Hamiltonian of the spin-orbit interaction is given by $(\vec{\nabla}V \times \vec{p}) \cdot \vec{\sigma}$ and for the perpendicular

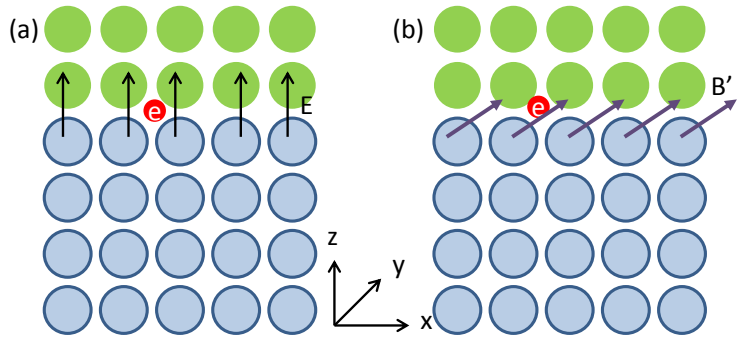

Figure 2.14: (a) Electron confined in x-y plane moving in a static an electric field $\vec{E}$. (b) In electron's frame of reference, Lorentz transformations generate magnetic field $\vec{B}'$ which depends linearly on velocity.

electric field $\vec{\nabla}V = (0, 0, E_z)$ results in a conventional k-linear Rashba effect, where $\vec{p}$ is an electron's momentum, and $\vec{\sigma}$ is the Pauli spin matrices.

To understand this, let us consider an electron constrained in x-y plane, moving in an external electric field $\vec{E} = E\hat{z}$ in the laboratory frame of reference with velocity $\vec{v} = v_x\hat{x} + v_y\hat{y}$, shown in Fig. 2.14 (a). In electron's frame, Fig. 2.14 (b), Lorentz transformations lead to appearance of a magnetic field $\vec{B}$, which is perpendicular to the electron's momentum and the direction of the electric field; and is proportional to electron's velocity: $\vec{B}' \sim p_x\hat{y} + p_y\hat{x}$, where $\hat{x}$ and $\hat{y}$ are unit vectors in x and y direction, respectively. The magnetic field interacts with the electron through the Zeeman term, $\mu_B\vec{\sigma} \cdot \vec{B}' \sim p_x\sigma_y + p_y\sigma_x$, which gives rise to the Rashba SOC. The essential feature of any SO coupling is that, even in the absence of an externally applied magnetic field, electrons moving in an electric field experience a magnetic field in their frame of motion – the SO field – that couples to the electrons magnetic moment.

Bulk $SrTiO_3$ has crystal inversion symmetry and time-reversal symmetry, thus the

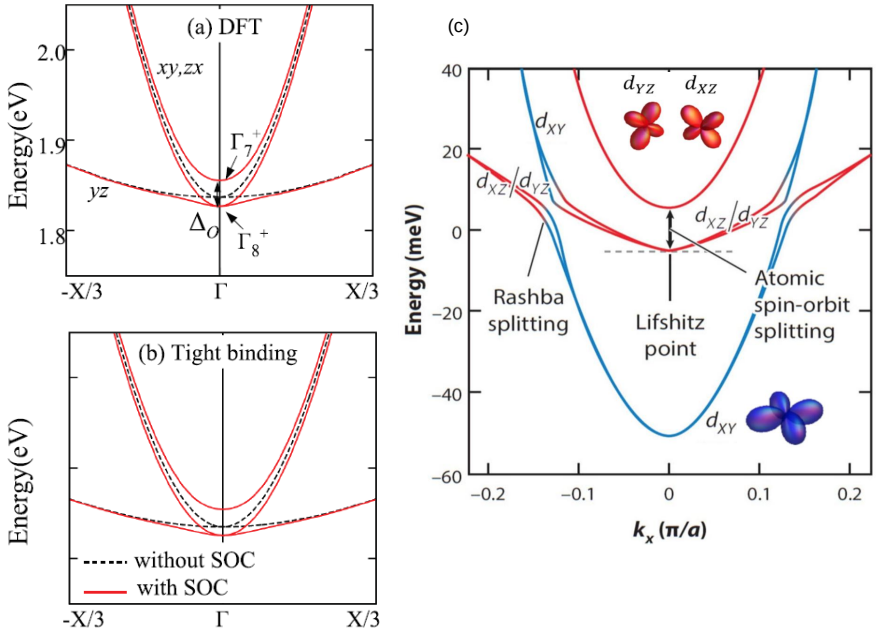

Figure 2.15: Band structure of t_2g orbitals in bulk $SrTiO_3$ calculated by (a) DFT and by (b) a tight binding model. In the absence of spin-orbit coupling, yz, zx, and xy are degenerate at the Γ point. SOC splits the sixfold-degenerate orbitals [80]. (c) Band structure for the 2DEG at the LAO/STO interface. Color-coded subbands are bands that are formed from the corresponding d orbitals [84]. The figure is adapted according to Ref. [85].

energy bands are still spin-degenerate. The conduction band of STO originates from Ti $3d$ orbitals. Because of the crystal field, the five degenerate $3d$ orbitals split into two e_g ($d_{x^2-y^2}, d_{z^2}$) and t_{2g} (d_{xy}, d_{yz}, and d_{zx} states) subbands [48]. An atomic SO coupling [80] causes the further splitting of t_{2g} states by Δ_0, see Fig. 2.15 (a) and (b). The early Raman characterization by Uwe *et al.* [81] measured $\sim$ 17 meV for this gap, while the later ARPES results by Chang *et al.* [82] and calculations of Marques *et al.* [83] provided higher values ($\sim$ 70-100 meV)

At the interface of LAO/STO, the crystal inversion symmetry is broken, so the SO

interaction lifts the spin degeneracy of the confined electrons. The band structure of the electron gas at the interface is shown in Fig. 2.15 (c). Strong SO coupling effects whose magnitude can be modulated by the application of an external electric field have been observed for the LAO/STO interface through magnetotransport studies [86]. Unlike in semiconductor heterostructures, interfacial carriers at the LAO/STO interface reside in the $3d$-t_{2g} conduction band of STO, potentially affecting the strength of the SO coupling [80]. Density-functional-theory calculations [80] show a large SO coupling effect around the Γ point, either with standard k-linear Rashba spin splitting or with a cubic dependence on the wave vector, depending on the sign of the d_{xz}/d_{yz} sub-band splitting. But, for d_{xy} sub-bands the Rashba SO coupling is calculated to be mainly k-cubic, with energy scale of a few meV to $\sim$ 20 meV [80, 87]. The form of k-linear is $H_{R1} = \alpha_{R1} i(k_-\sigma_+ - k_+\sigma_-)$, and the form of the k-cubic is $H_{R3} = \alpha_{R3} i(k_-^3\sigma_+ - k_+^3\sigma_-)$, where, $\sigma_\pm = (\sigma_x \pm i\sigma_y)/2$ and $k_\pm = (k_x \pm ik_y)/2$ with k being the wave vector.

One of the experimental manifestations of spin-orbit interaction are Weak Localization (WL) and/or Weak Anti Localization (WAL) effects through magneto-transport measurement. These effects are discussed in the subsequent section.

2.6 Weak Localization (WL)

The electronic transport in solids can be classified by three main characteristic lengths: (i) The mean free path ℓ, which is the average distance that an electron travels before its momentum changes by scattering from scattering centers. (ii) The phase coherence length ℓ_φ, which is the average distance over which an electron can maintain its phase coherence. ℓ_φ is usually determined by inelastic scattering of electrons by phonons or other electrons.

These characteristic lengths are also associated with their corresponding life times, τ and τ_i, which are the lifetimes of conduction electrons in an eigenstate of momentum and an eigenstate of energy, respectively. (iii) The sample size L.

If $\ell \gg L$, electrons can propagate through the sample without being scattered. This is known as the ballistic transport regime. If $\ell \ll L$, electrons will scatter and diffuse through the sample, and this is known as the diffusive transport regime. In the diffusive regime, if $\ell_\varphi \leq \ell$, it is referred to as semiclassical diffusion, and leads to the Drude conductivity:

$$\sigma = \frac{ne^2\tau}{m} \tag{2.1}$$

In the diffusive regime, if $\ell_\varphi \gg \ell$, a conduction electron in state with momentum k can be scattered by impurities (even many times) without loosing its phase coherence. Due to the statistical distribution of the impurities, the multiple scattered waves form a chaotic pattern. The usual Boltzmann theory (Drude conductivity) neglects interferences between the scattered partial waves and assumes that the momentum of the electron wave disappears exponentially after the time τ. However, neglecting the interference is not quite correct. There can be a coherent superposition of the scattered electron waves, which results in back-scattering of the electron wave and lasts as long as its coherence is not destroyed. In this diffusive regime, the quantum interference between time-reversed scattering loops, in which one or more impurities are present (Fig. 2.16), will result in a correction to the conductivity [88, 89]. The weak localization or weak anti-localization is an effect due to this correction in the conductivity in the quantum diffusive regime. Another useful way to see the quantum correction to the conductance, is the cartoon on the right panel in Fig. 2.16 which shows a

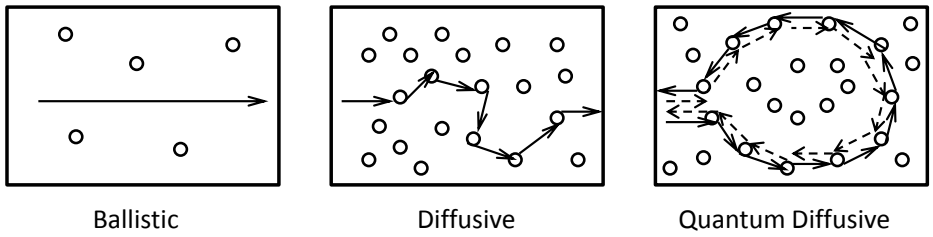

Figure 2.16: Schematic of different electronic transport regimes in solids. The open circles represent impurities and arrows shows the trajectories that electron traveled.

diffusion path of a conduction electron in a disordered system. The electron propagates in both directions: full lines with the wave function of $\psi_1 = |\psi_1|e^{i\theta_1}$, and dashed lines with the wave function of $\psi_2 = |\psi_2|e^{i\theta_2}$. Classical diffusion physics assumes an identical probability for the electron to propagate on the same path in the opposite direction. The two probabilities add up and contribute to the total probability of finding the electron: $|\psi_1|^2 + |\psi_2|^2$. But, electrons have wave-like character, so the the total probability of the electron moving from one point to another point is $|\psi_1|^2 + |\psi_2|^2 + 2|\psi_1||\psi_2|\cos(\theta_1 - \theta_2)$. So, this interference term effectively makes it more likely that a carrier will wander around in a circle, which leads to an increase in the net resistivity.

This weak localization correction originates from quantum interference between self-crossing paths in which an electron can diffuse in the clock-wise and counter-clockwise direction around a loop. The quantum phases cancel each other exactly because the length of the two paths along a loop are the same, and thus this quantum interference term can survive disorder averaging. Weak localization exists in one, two and three dimensions, but it is more probable to find a self-crossing path in lower dimensions. So, weak localization

effect are more appreciable in thin films and wires. In systems with strong SO coupling, the electron spin rotates as it propagate through a self-intersecting trajectory. The spin rotation direction is opposite for the two paths around the loop. As a result, the two paths along the loop interfere destructively which suppresses the net resistivity, as schematically is shown in Fig. 2.17. Thus, this effect is called weak anti-localization.

For two dimensional systems at low but finite temperature, Anderson *et al.* [90] and Gorkov *et al.* [91] showed that the quantum interference correction to conductivity has some sort of logarithmic dependence on ℓ and ℓ_φ:

$$\sigma_{QI} \propto \pm \frac{e^2}{\pi h} \ln(\frac{\ell_\varphi}{\ell}) \tag{2.2}$$

where e^2/h is the conductance quantum, the $-$ and the $+$ signs corresponds to WL and WAL, respectively. Note that this correction is temperature dependent; ℓ is defined by the elastic scattering so it is not a function of temperature, but ℓ_φ is determined by inelastic scatterings so it is usually depends on temperature. At low temperatures, ℓ_φ becomes longer and so the quantum correction to conductivity becomes important. A schematic temperature dependence of the conductivity is shown in Fig. 2.17.

Weak anti-localization enhances the conductivity and weak localization suppresses the conductivity with decreasing temperature at very low temperatures. These effects provide valuable information about the system, such as symmetries of the system, the phase coherence length [93], and the quasiparticle mass [94]. Magnetoresistance experiments can often help sort out the various contributions to the transport.

Major contributions to the magneto-conductance of a disordered electronic system

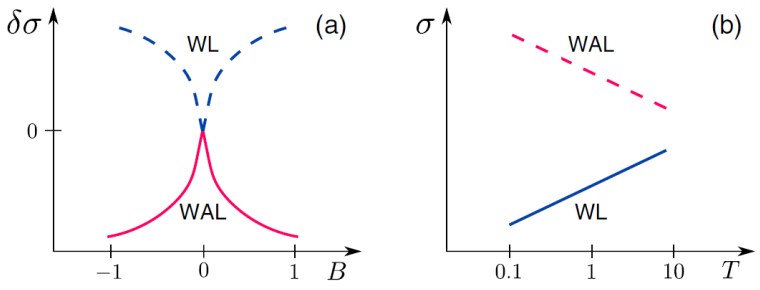

Figure 2.17: Schematic of WL and WAL in two dimensions in (a) magnetoconductivity, defined as $\delta\sigma \equiv \sigma(B) - \sigma(0)$, and (b) temperature dependence of the conductivity σ. B is the magnetic field and T is temperature. Adapted from Ref. [92].

are interactions (mainly Coulomb), which contain exchange and Hartree terms, and weak localization, which involves the SO interaction term. In a diffusive regime for a confined 2DEG, where the inversion symmetry is broken, the SO interaction mechanisms fall into two main competing categories: Elliot-Yafet (EY) and D'yakonov-Perel (DP) mechanisms. These two electron spin relaxation processes have received much attention in connection with various spintronics applications.

The Elliot-Yafet mechanism [95, 96] is related to electron spinflip scattering owing to a wave vector dependent admixture of valence-band states to the conduction-band wave function. In this case, the electron spins relax as the spin-orbit interaction causes them to not be in a pure spin state and thus the spin coherency is lost with each act of scattering. The EY mechanism takes into account the change in the spin polarization of a Bloch state due to scattering by impurities, lattice defects, or phonons This mechanism establishes a linear relation between the spin-orbit relaxation time and the elastic scattering time, $\tau_{SO} \propto \tau_{el}$.

In the D'yakonov-Perel mechanism [97], the coherency between spins is destroyed not due to the scattering as in EY case, but as a result of spin precession in an inhomogeneous magnetic field between successive scattering events. The spin-orbit relaxation time is inversely proportional to the elastic scattering lifetime in DP spin relaxation mechanism, $\tau_{SO} \propto \tau_{el}^{-1}$.

Two main groups of theorists applied these relaxation mechanisms to understand magneto-conductance in 2D materials due to WL/WAL: the Hikami-Larkin-Nagaoka groups and the Maekawa-Fukuyama (MF) that use EY mechanism, and the Iordanskii, Lyanda-Geller, and Pikus (ILP) group that use the DP relaxation mechanism. The MF equation [98] uses k-independent and the HNL theory [99] uses k-cubic corrections, to the magneto-conductance. The ILP equation [100] considers spin-orbit interaction effect on the weak localization as an effect of a spin-dependent vector potential (has both k-linear and k-cubic corrections). The prediction by of Hikami *et al.* (logarithmic increase of the conductance with decreasing temperature in the presence of strong SO coupling) was experimentally confirmed by Bergman. He prepared bilayers of Au/Mg, with different thickness of Au. Mg is a metal with the smallest possible spin-orbit coupling. On the other hand, Au has a strong spin-orbit coupling. As can be seen in Fig. 2.18 the spin-orbit coupling modifies the weak localization of the conduction electrons in thin films and reverses the magnetoconductance.

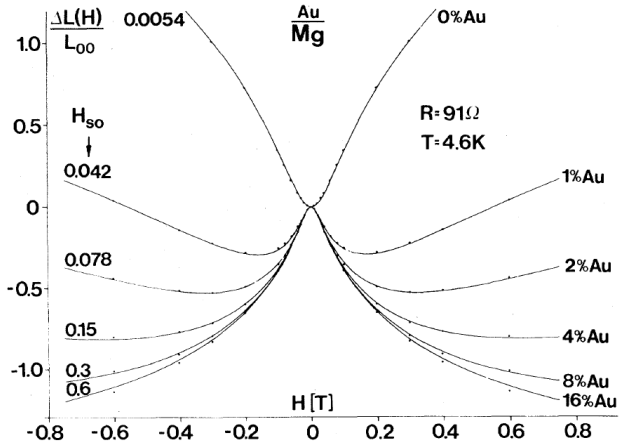

Figure 2.18: The magnetoresistance of a thin Mg- film at 4.5 K for different coverages with Au. The Au thickness is given in % of an atomic layer on the right side of the curves. The coating with Au increases the spin-orbit scattering. The points are experimental data and the full curves are obtained with the HLN theory. The ratio on the left side gives the strength of the adjusted spin-orbit scattering. It is essentially proportional to the Au-thickness. L_{00} is the universal conductance.

Caviglia *et al.* [86] first observed Rashba SO coupling in LAO/STO by modulation of the SO interaction through an application of an external electric field. He used MF equations and deduced that the spin relaxation time is proportional to the inverse of the elastic scattering time over a wide voltage range ($\tau_{SO} \propto \tau_{el}^{-1}$) and thus suggested the DP mechanism characteristic for the Rashba SO interaction of the 2DEG. Later, Nakamura *et al.* [101] investigated a spin-orbit coupling in gated $SrTiO_3$, in which inversion symmetry is preserved in its bulk form. By analyzing an antilocalization effect on magnetoresistance, they observed the distinct configuration of a spin-precession vector in a k plane based on the k-cubic-Rashba effect compared to the linear Rashba effect.

2.7 Kondo mechanism

The Kondo effect is a consequence of scattering of the electrons in a non-magnetic metal from dilute magnetic impurities at low temperature, and it manifests as an increase in the resistivity at low temperature. The conduction electron magnetizes in the vicinity of the magnetic ion. This magnetization causes an indirect exchange interaction between two magnetic ions, because a second ion becomes aware of the magnetization induced by the first ion. An indication of this interaction is the occurrence of a minimum and an upturn at low T in the resistivity curve. Often, when a resistance minimum is found, a local magnetic moment is linked to that. The question started in 1933; Dutch physicist Wander Johannes de Haas and co-authors reported an unexpected rise in the resistivity of some gold samples at low temperatures (metals typically show a resistivity which continuously decreases by lowering the temperature and eventually saturates at a value which depends on the impurity concentration). In 1961, Phil Anderson introduced a microscopic model that explained how local moments form in metals, with magnetic impurities, without getting screened by electrons (magnetic impurities can be screened by itinerant electrons such that they don't act like a local moment). The theory explained that the impurity moments couple antiferromagnetically to the spins of the conduction electrons. In 1964, Japanese physicist Jun Kondo showed that the anomalous high resistance at low temperature is the consequence of the dynamic nature of the scattering by the exchange coupling and of the sharpness of the Fermi surface at low temperatures. Kondo added a logarithmic term of $\ln(\frac{kT}{W})$, where W is the width of the electron band, to the temperature dependence of the resistivity to explain the upturn. Kondo's calculations could reproduce the resistivity upturn, but the zero-temperature limit remained unsolved–the logarithmic divergence cannot physically persist

to zero temperature. In 1974, Nobel Prize winner Kenneth Wilson was able to first solve the Kondo model by the numerical renormalization group.

The Kondo effect was one of the main signatures of magnetism in LAO/STO first reported by Brinkman *et al.* [69]. Subsequently, the Kondo effect was reported for electrolytically-gated $SrTiO_3$ [102], $LaAlO_3/EuTiO_3/SrTiO_3$ trilayer structures [103], and for δ-doped/$LaTiO_3/SrTiO_3$ [104]. The observed negative magnetoresistance, for both the in-plane and out-of-plane magnetic field directions, has been explained within the context of Kondo interaction [102]. However, Diez *et al.* [105] proposed an alternative explanation, based on the very large (70%) negative in-plane magnetoresistance, gate voltage data, temperature profiles for the resistance, and theoretical calculations. Diez *et al.* proposed an explanation fully within the single-particle context of Boltzmann transport to explain the negative in-plane giant magnetoresistance. The Boltzmann transport equation with spin-orbit coupling, in combination with anisotropy of the Fermi surface and scattering rates, suffices to produce a large resistance drop upon application of a magnetic field. He proposed that the combination of spin-orbit coupling and scattering from finite-range impurities can explain the observed magnitude of the negative magnetoresistance.

Ultraviolet light illumination (365 nm) is reported to suppress the Kondo upturn [106]. The suppression has been related to the destruction of the Kondo coherence of magnetic ions.

Chapter 3

Equipment and Characterization Techniques

3.1 Pulsed Laser Deposition (PLD)

Thin film samples for this study were synthesized using the Pulsed Laser Deposition (PLD) method. The basic idea of the technique is to use the pulses of a high-power laser to evaporate a small amount of a solid target. The target is the material from which we want to make thin films. The principle of PLD relies on photons interacting with the target. The focused laser pulses are absorbed at the target surface in a small volume. The absorbed energy density of the laser is sufficient enough to break the chemical bonds of the molecules within that volume; there occurs conversion of the energy to electronic excitation. Further energy conversions to thermal, chemical, and mechanical result in evaporation and ablation from the surface of the target. Most of the ablated target material is in the ionized form and thus it is called *plasma plume*. The plasma plume then solidifies on a substrate, and the thin films are formed. The conventional theory of film growth during the deposition also applies here: depending on energies, possibilities include three-dimensional island growth, two-dimensional monolayer formation, and the growth of separate islands on top of a full monolayer. The total free energy of the system governs the balance between growth and dissociation of a cluster. Practically and often, the free energy can be tuned by lowering the temperature (or increasing the deposition rate). For instance, deposition at low temperatures can promote amorphous phase instead of crystalline. If the surface energy of a nucleated

cluster is low and that of the substrate is high, it is energetically more favorable for the film to form as full monolayers. The deposition can occur either in vacuum or in the presence of some dilute background gas, which influences the composition of the film. If the conditions such as laser parameters, substrate temperature, and background gas pressure are right, the film will have the same stoichiometry as the target. Ref. [107] is a nice book on principles of PLD.

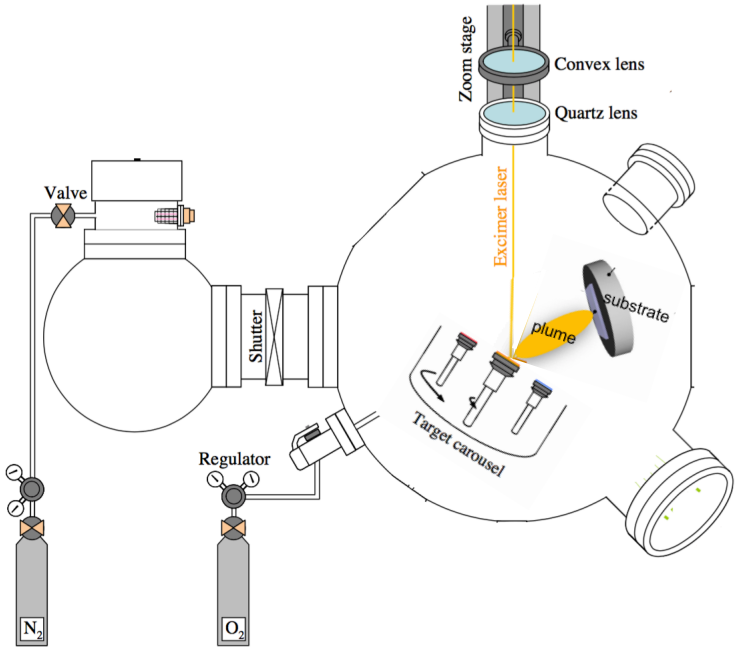

Figure 3.1: Schematic of pulsed laser deposition; Ota master thesis [108], modified. The image is not drawn to scale.

A wide variety of materials can be made into thin films using PLD. In particular, PLD works for insulators, such as oxides. Metals that have very high conductivity do not ablate well by laser, as the electromagnetic waves do not penetrate well into metals. The

main components of a PLD system are the KrF excimer laser, vacuum chamber and pumps, and substrate and target holders. A schematic illustration of a PLD system is shown in Fig. 3.1.

In our PLD set-up, a Lambda Physik COMPex 201 KrF laser ($\lambda = 248$ nm) is used for ablation of the target material. The laser has a maximum energy output of 200 mJ, pulse duration of 25 ns, and repetition rates up to 10 Hz. The laser beam is focused onto the target using a high energy excimer mirror at 50°, and a 50 cm focal length lens placed 5.5 inches from the chamber window. The ablated area on the target has a rectangular shape, 2 by 3 mm^2, the size of which can be modified by changing the position of the lens. Our set-up accommodates multiple targets that can rotate. Dr. Mark Monti installed the system and designed the substrate and target holders; a detailed explanation of our PLD is in his Ph.D. dissertation.

3.1.1 Growth parameters

There are many growth parameters that highly affect sample properties. Laser fluence and repetition rate, oxygen pressure during growth, substrate temperature, and target morphology are some of the main parameters.

–Laser Fluence and Repetition

The fluence (energy per unit area, typically reported as $J.cm^{-2}$) of a laser pulse has to be larger than a certain threshold value so that abalation would be possible, and also so that all the species in the target could be removed stoichiometrically. Too high of a fluency might lead to the removal of large target fragments, which increases the number of particulates on the film. For aluminates deposition, we typically use about 50-100 mJ, which gives

1.7-3.3 J.cm^{-2} fluency. For Ni deposition, higher energy is required; I used 150 mJ. I did not notice any change in the quality of the films by varying the repetition rate in the range of 1–8 Hz.

– Oxygen Pressure During Growth (P_{O_2})

As was mentioned in the previous chapter, oxygen vacancies are one of the mechanisms of conductivity at the $LaAlO_3/SrTiO_3$ interface, and thus the oxygen partial pressure during growth is highly influential on the thin films electrical properties. In this study, high purity oxygen gas (research grade, 99.9995% purity) was introduced into the chamber through a series of valves and can be fine tuned using a flow meter. P_{O_2} was varied over the range of $6 \times 10^{-6} - 10^{-3}$ torr for synthesizing $RAlO_3$ (R = La and Pr) thin films. The background pressure in the chamber was kept as low as $\sim 7 \times 10^{-7}$ torr, which was achieved by the combination of a rotary and a turbo pump. After the deposition, the $RAlO_3$ samples were post-annealed in situ in the same P_{O_2}.

– Substrate Temperature

Substrate temperature can affect the thermodynamics and the kinetic processes of growth, as well as provide lattice matching for materials of differing thermal expansion coefficients. The substrate temperature is increased by a custom designed heater (Kanthal A1 with 0.018" diameter). The highest temperature available in our system is $\sim 750°C$.

– Target Morphology

Targets for PLD can be either single crystal or polycrystalline (which can be made using solid state reactions technique). The surface of the target affects the quality of the film. Dense and smooth-surface targets are desired. It is often suggested to polish the surface of the target after each couple of runs to have a smooth surface. Particulates may come off

from a cracked or textured target and get deposited on the substrate.

3.2 Target preparation

Targets should be in the form of a large flat disk with a diameter of 1.5 cm, at least. For $LaAlO_3$ thin film deposition both the single and polycrystalline targets were used.

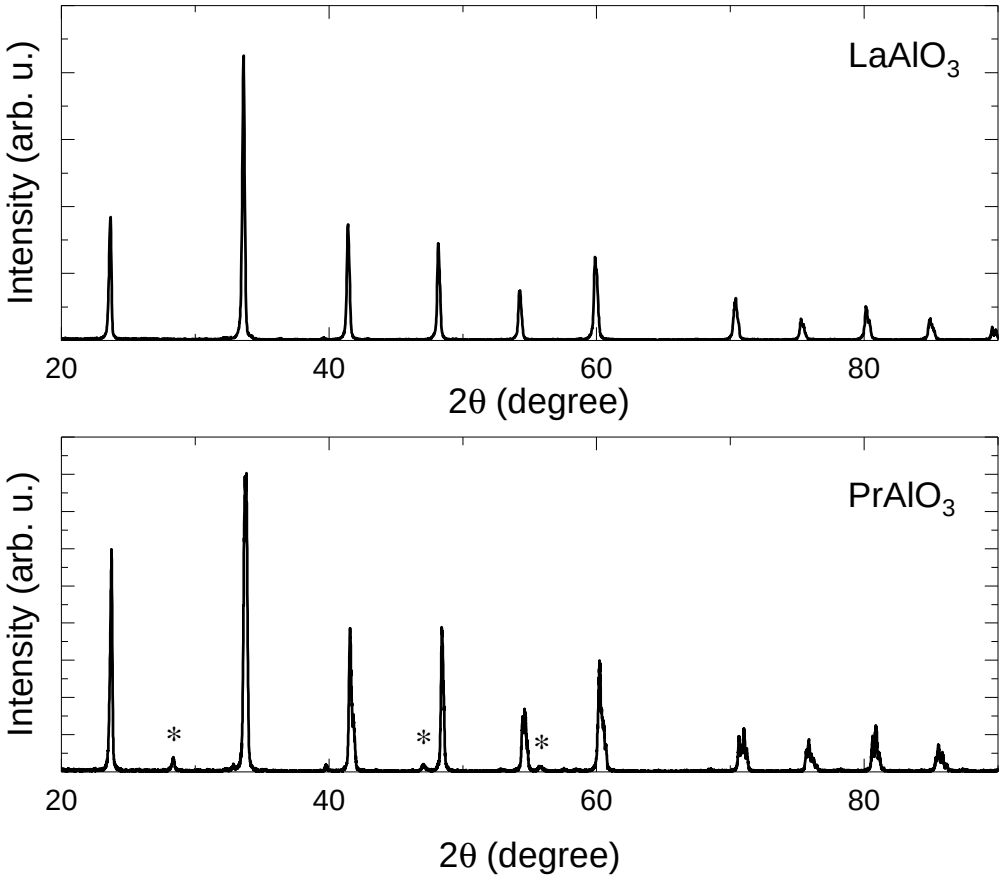

Figure 3.2: X-ray diffraction pattern of the polycrystalline $LaAlO_3$ (top panel) and $PrAlO_3$ (bottom panel) targets. $*$ shows the peak positions for the impurity phase of Pr_6O_{11}, which can be removed by grinding for longer times and annealing at higher temperatures.

The single crystal target, which is a disk with 2.54 cm diameter and 0.5 mm thickness, was purchased from the MTI company. The polycrystalline target was made by the solid state reaction technique. I did not notice any difference in the quality of the films that were made with the single crystal or polycrystalline targets. For the $PrAlO_3$ thin film deposition, the target was made by the solid state reaction method. To make a target suitable for PLD, 8–10 grams of the final compound is needed to make a large disk (1.25" diameter) target. To create a stoichiometric ratio for the final compound, $RAlO_3$ (R=La and Pr), the exact weight of each oxide (for instance, Al_2O_3, La_2O_3, and/or Pr_6O_{11}) was calculated precisely, using the atomic weight of each element. High purity oxide powders were weighed and then individually dried in alumina crucibles in a 900°C furnace overnight to burn off any carbonates. After this initial drying step, the exact ratio of oxides was precisely weighed and ground for a long time to get a fine and homogeneous powder, using a mortar and pestle. The grinding was repeated at least three times. The compound was kept at 1200°C between each grinding over night. Then, the powder was pressed into a pellet using a hydraulic press to create a dense disc. For our 1.25" diameter pellet, a pressing of 12000 lbs, corresponding to a pressure of 66 MPa was used. The pellet is extremely fragile and was removed from the press with care and placed onto a clean flat tray alumina crucible. The $RAlO_3$ pellet was sintered at 1500°C for 12 hours, and cooled down slowly to achieve a polycrystalline dense disk that was suitable for ablating stoichiometric thin crystalline films. Fig. 3.2 shows the XRD pattern of the LAO and PAO targets used in this study.

3.3 Surface analysis: Atomic Force Microscopy (AFM)

Atomic force microscopy is a powerful technique to study the surfaces of materials. The probe of the AFM is a cantilever. The tip resonances and scans over the surface of the sample. The surface structure is mapped by the change in the force (and thus the change in the frequency of the tip) experienced by the tip of the cantilever. The oscillation of the tip is detected by a laser reflected from the top side of the cantilever. The change in the oscillation of the tip is translated into the change in the topography of the surface that is to mapped. A schematic of an AFM is shown in Fig. 3.3.

For this thesis, I took the topographical images of the substrate and the film surfaces with a Veeco Atomic Force Microscope (AFM), ex situ at room temperature using the tapping mode. Silicon cantilevers (Bruker) with resonance frequencies of 300-350 kHz and force constants of 20-80 N/m were used. Cantilevers that are coated with Al (RTESPA) for high reflectivity, often provide a sharper image. Sometimes, Gwyddion software was used to process the raw AFM images.

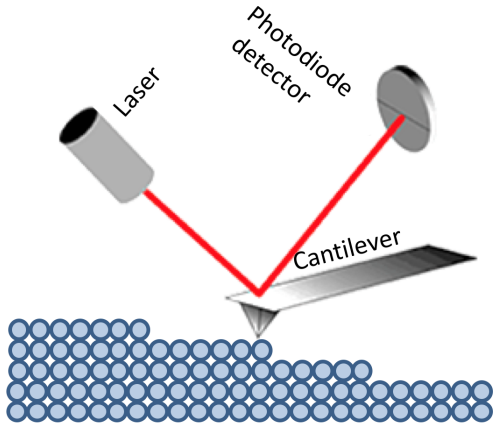

Figure 3.3: Schematic of Atomic Force Microscopy.

3.4 Substrate preparation

As was mentioned in the previous chapter, the specific termination of the substrate has a great impact on the electronic properties of the heterostructure. The TiO_2 termination is the desired termination for the $SrTiO_3$ substrate in this study. An as-received STO substrate has a mixed termination of SrO and TiO_2, shown in Fig 3.4(a), which often is not possible to see using an AFM. To achieve a TiO_2 termination, Fig 3.4(b), a series of suitable chemical etching and thermal treatments should be followed. References [109, 110, 111] have a nice review of different titration methods to achieve single termination for STO.

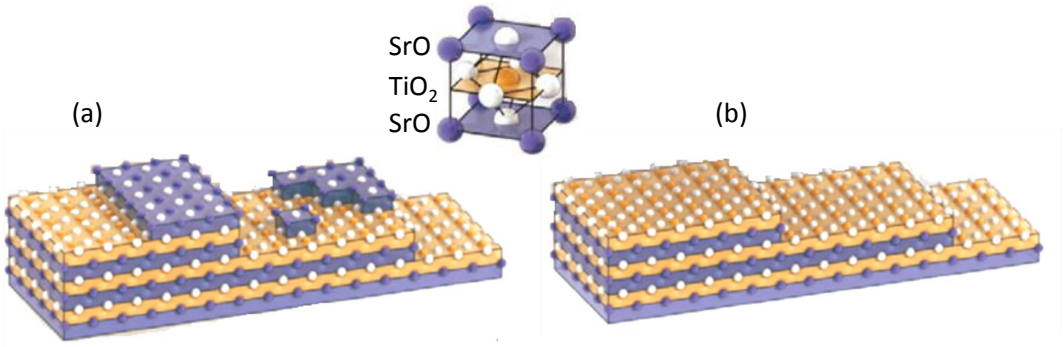

Figure 3.4: (a) Schematic illustration of as as-received $SrTiO_3$ substrate; the termination is a mixture of SrO and TiO_2. (b) Schematic illustration of the desired TiO_2 termination which could be achieved by suitable chemical etching and thermal treatments.

In our lab, a systematic study of etch processes to optimize the quality of the TiO_2 termination and the reproducibility of the etch procedure was performed by Dr. Mark Monti. He studied the effects of three different etchants: two different buffered oxide etchants of HF:NH4F (BOE 6:1 from J.T. Baker and BOE 10:1 from KMG chemicals) and aqua regia, a 3:1 mixture of $HCl:HNO_3$, as a function of etch time. His results indicates that BOE

10:1 provides a better result. I prepared the substrate based on the procedure explained in his thesis. The procedure is as follows: Substrates should be first cleaned in an ultrasonic agitator first using isopropanol, then acetone, and then isopropanol for 15 minutes each. Then the substrates should be agitated in 60°C deionized (DI) water for 20 min. This step promotes the formation of strontium hydroxide. The temperature should be carefully measured. Temperatures higher than 60°C resulted in a jagged shaped terraces. Hold the substrate by a plastic tweezer so that you can immediately transfer it to the next step. The next step is to dip the substrate in BOE 10:1 for 1 minute.

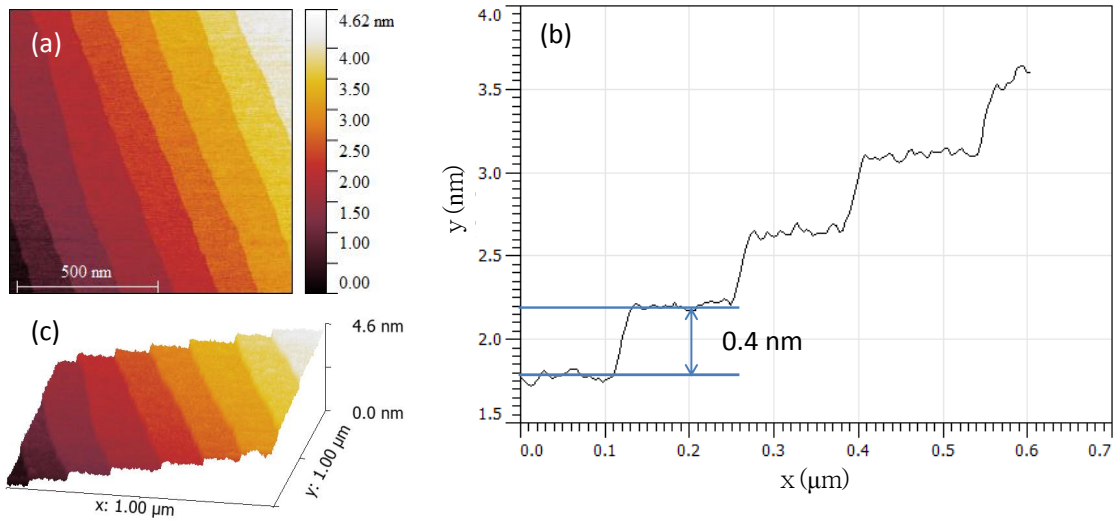

Figure 3.5: (a) An AFM image of a terminated STO substrate (b) A line scan taken perpendicular to the terraces that verifies the unit cell step size between terraces, indicating single termination. (c) 3D AFM image of the substrate.

Better results were achieved when the HF container was placed inside the ultrasonic agitator.

By etching, strontium hydroxide is dissolved in HF, leaving a TiO_2 layer on the surface. I then annealed the etched substrates in oxygen at 950°C for 1 hour to get smoother step edges.

Longer annealing time causes the migration of the Sr atoms to the surface. The annealing time depends on the miscut angle of the substructure. The time required for thermal treatment increases with terrace length. The dependence of the annealing time on the miscut angle and the number of dislocations in the crystal make this termination procedure difficult to be reproducible each time. The etched substrates were characterized by AFM to determine the quality of the substrate prior to thin film deposition. Fig. 3.5 shows AFM images of an STO substrate that was TiO_2-terminated in the lab, along with a line scan normal to the terrace edges. The unit cell step size between terraces indicates single termination. The images also reveals flat terraces, ~ 140 nm or ~ 350 unit cells wide, corresponding to a typical miscut angle ($\sim 0.2^\circ$) for this substrate.

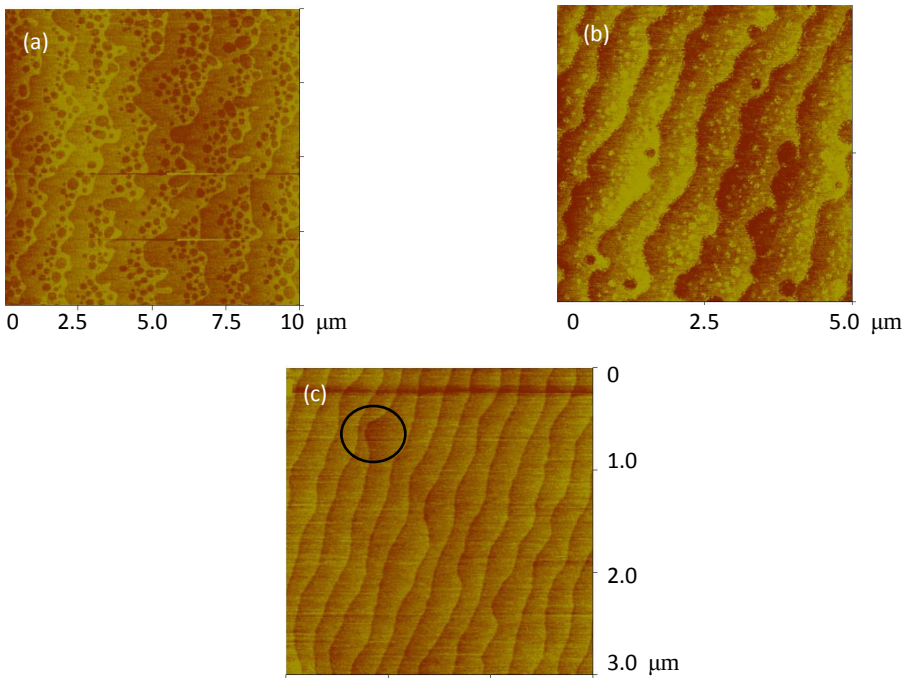

Figure 3.6: (a) and (b) Round deep features that sometimes appear at the edge of the terraces with large width. (c) Step bunching that is shown by a circle in the AFM image.

The substrates were bought from MTI in the USA or CrysTec in Germany. I found that the procedure works well for the substructures that are from the CrysTec company. However, on some of the substrate purchased from CrysTec that have low miscut angle, some round deep features appear at the edges of the terraces; see Fig. 3.6 (a) and (b). I did not find any influence from these features on electrical properties. Step bunching can also happen, as can be seen in Fig. 3.6 (c). If the density of the step bunching is low, they do not seem to have any affect on the crystallinity and the transport properties of the films.

3.5 Structural characterization: X-Ray Diffraction (XRD)

X-Ray Diffraction (XRD) is a major characterization technique for thin films. High-quality diffraction data can provide information such as the crystal structure and quality, atomic arrangement, stress/strain, film thickness and defects in a crystal. In the XRD process, the atoms of a crystal cause a beam of x-rays to diffract into many directions. The diffracted rays form a constructive and destructive interference pattern. If a fixed value of the wavelength is used for the incident x-rays, each diffracted angle is associated with interference from a specific set of atomic planes of the crystal. To have constructive interference between the diffracted beams, Bragg's law

$$2d_{hkl}\sin\theta = n\lambda \tag{3.1}$$

should be satisfied. In Eq. 3.2, d is the spacing between the crystal planes, hk and l are integers known as Miller indices, θ is the x-ray diffraction angle, λ is the wavelength of the x-rays, and n is the order of diffraction. For an orthorhombic structure, d can be found by

$$d^2 = \frac{1}{\frac{h^2}{a^2} + \frac{k^2}{b^2} + \frac{l^2}{c^2}} \tag{3.2}$$

where, a, b, and c are orthorhombic lattice parameters.

For this study, a Philips X'PERT diffractometer using CuK_α x-rays with $\lambda = 1.5406$ Å, was operated at 40 kV and 30 mA. For this machine, the sample substrate was mounted on putty in a stainless steel holder and pressed flat using a glass slide. Alignment was achieved using the (002) reflection of STO. Later, UT purchased another x-ray machine, in which the alignment is easier; the Rigaku Ultima IV. Rigaku uses CuK_α x-rays radiation and operates at 40 kV at 44 mA, providing more source power. It can work both in Bragg Brentano (BB for powder diffraction) and Parallel Beam (PB for thin film diffraction) modes. Some of the

XRD data are taken using the Rigaku machine. Fig. 3.7 (a) shows a schematic illustration of the Rigaku Ultima IV diffractometer. The main parts are the x-ray source, a monochromator which selects CuK_α radiation, different sets of slits that align the beam, the sample stage, attenuator, and detector. The detector records the x-ray photon count scattered from the sample. The source, sample stage, and detector can rotate.

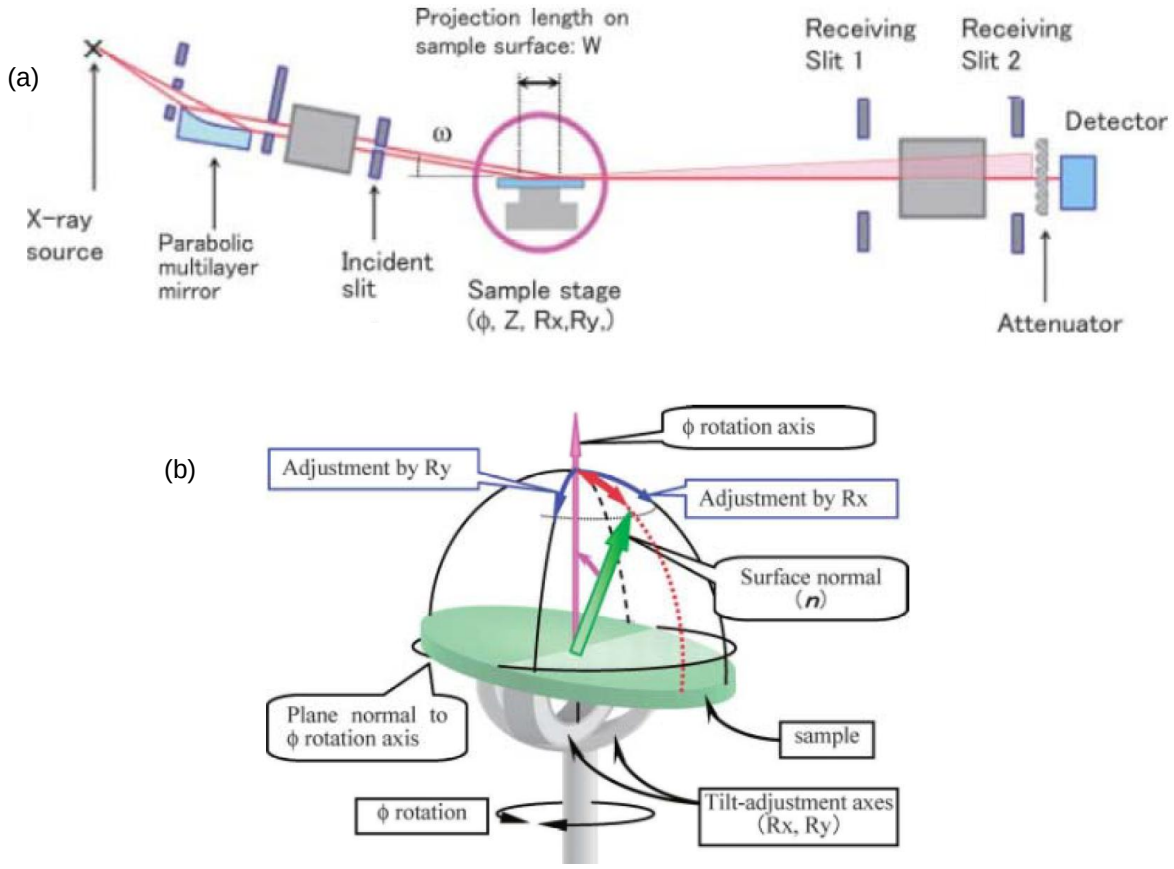

Figure 3.7: Schematic illustration of (a) the Rigaku Ultima IV, and (b) sample alignment, showing various angles and axis. The figures are taken from Rigaku website.

The incident beam angle is characterized by angle θ (also called ω). At $\theta = 0$, along the direct beam axis, the source and detector directly face each other. The detector can rotate with respect to the incident beam direction by angle 2θ. The angle between incident beam and the diffracted beam is 2θ. For alignment, the sample stage can rotate in three different directions: local x and y coordinate frame (Rx and Ry rotation), and around the direct incident beam axis (ϕ rotation, where ϕ is the angle measured in perpendicular direction to θ), see Fig. 3.7 (b).

3.5.1 Profile measurement: Out-of-plane diffraction measurements

This is a routine XRD scan to get information about the crystal structure including lattice constants, lattice distortion, crystal orientation, crystallite size, etc. This scanning mode is also often called $\theta - 2\theta$ or $\omega - 2\omega$ scan, where the x-ray source rotates by angle θ and the detector rotates by angle 2θ, simultaneously. The XRD spectrum consists of peaks in the intensity recorded by the detector at certain 2θ angles, such as the spectrum in Fig. 3.8. Epitaxial thin films that have a high degree of crystalline perfection can be probed by XRD. The film peaks are often very weak relative to the substrate peaks, due to the small number of planes involved in the diffraction. The spectrum is often plotted on a square-root or on o logarithmic scale to make the film peaks visible. Fig. 3.8 shows a typical $\theta - 2\theta$ XRD spectrum of PAO/STO. The peak at about 42° is due to copper K_β radiation. And, the peak at about 44° is due to tungsten radiation, W-L_α. The XRD machine uses a fixed copper (Cu) anode target to produce x-rays. If a monochromator is not installed the Cu-K_β ($\lambda = 1.3926$ Å) radiation is not filtered out, and appears in the XRD spectrum. The tungsten radiation contamination is due to the fact that most of the x-ray cathodes are

made with a tungsten filament. Over time, small amounts of tungsten evaporate from the cathode and get deposited on the anode. The characteristic of this contamination is that it will increase with the age of the anode as more and more tungsten gets deposited on the copper anode. The characteristic contamination occurs at $\lambda = 1.4764$ Å. To get rid of these two peaks, Cu-K_β and W-L_α, a monochromator should be installed, or an attenuator should be set around those peaks.

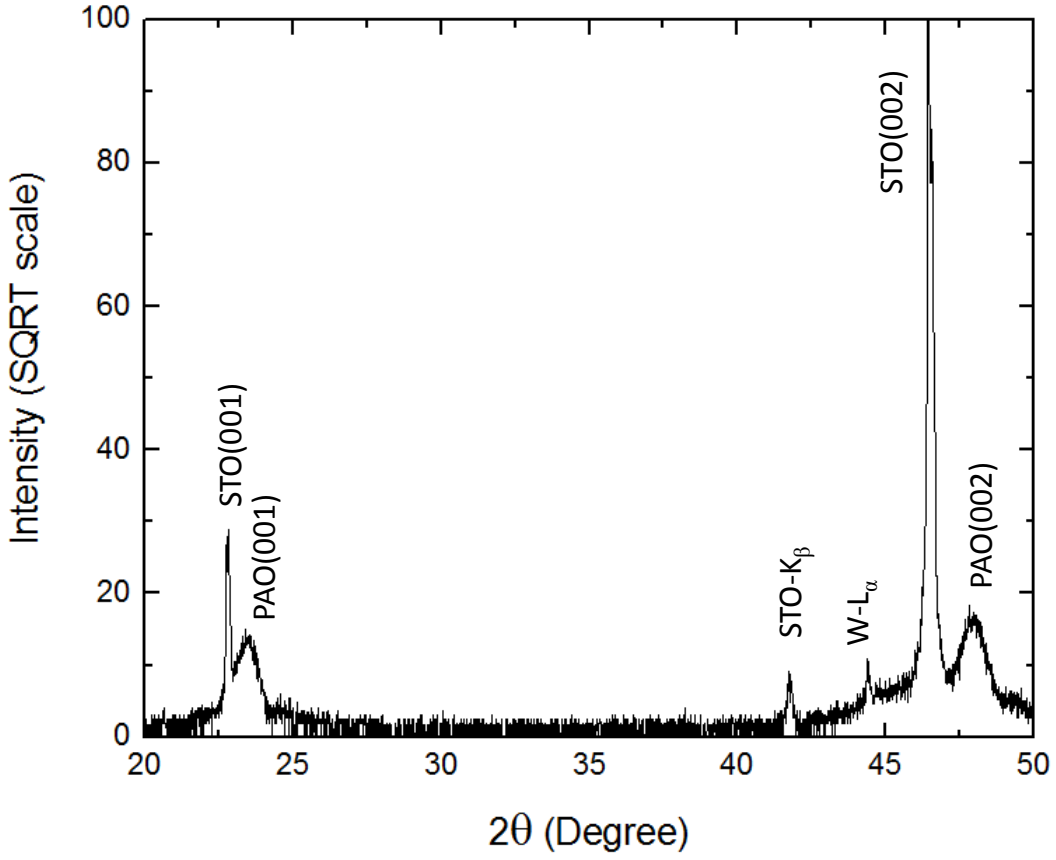

Figure 3.8: XRD data for thin films of PAO grown on STO.

3.5.2 X-Ray Reflectivity (XRR) measurement

X-ray reflectivity is a technique that can determine surface and interface roughness, film thickness, and the density of the thin film samples. In this study, I used XRR to measure the thickness of the thin films. The range of thickness that can be determined by XRR is about 2-200 nm. The scan is very similar to $\theta - 2\theta$ scan except that that the incident angles are very small, $0^\circ - 5^\circ$ (grazing angles). The x-ray beam irradiates the sample at a grazing angle θ and the reflected intensity at an angle 2θ is recorded. At each surface or interface, part of the beam is reflected due to the different electron densities in the different layers. At very small angles $\theta < \theta_c$, the x-ray source and detector are facing each other, and almost all of the incident beam is reflected from the film surface. When the incident angle θ is equal to the total reflection critical angle $\theta = \theta_c$, x-rays propagate along the sample surface. At $\theta > \theta_c$ the incident beam penetrates into the film by refraction. At every interface, a portion of x-rays is reflected. Interference of these partially reflected x-ray beams creates a reflectometry pattern. The reflection from the different interfaces interfere and give rise to interference fringes. The period of the interference fringes is related to the thickness of the film, and the fall in the intensity is related to the roughness of the layer, see Fig. 3.9. The critical angle which is often less than 0.3° provides information about the density of the film. The formula to calculate thickness d is,

$$d = \frac{\lambda}{2} \frac{(m-n)}{(\sin\theta_m - \sin\theta_n)} \tag{3.3}$$

where λ is the wavelength, and θ_m and θ_n are m^{th} and n^{th} fringe positions in the XRD spectra. Fig. 3.10 shows some XRR scan for the typical thickness of thin films used in this study.

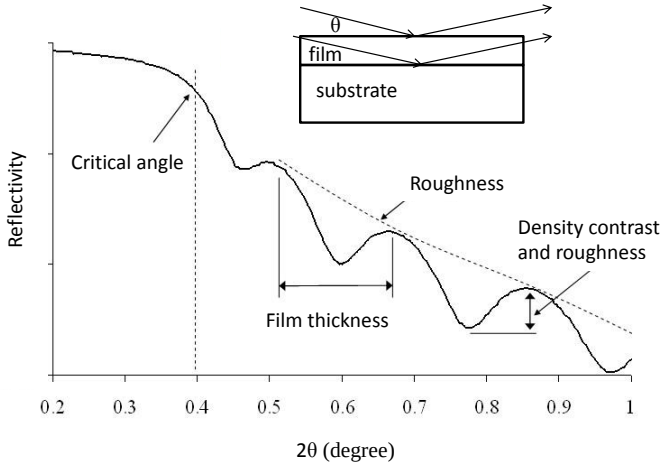

Figure 3.9: A typical XRR spectrum.

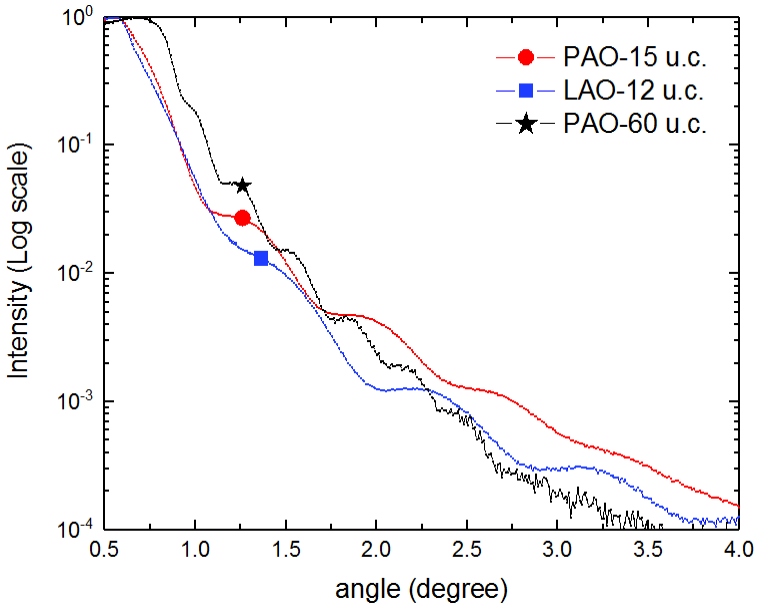

Figure 3.10: XRR scans for PAO and LAO thin films with different thickness on STO.

3.5.3 Rocking curve measurement

The preferred orientation direction and the degree of the orientation are two separate important factors in thin film crystallography. The orientation direction can be determined by a $\theta - 2\theta$ scan. The degree (or distribution) of the orientation can be obtained by a rocking curve measurement as shown in Fig. 3.11. This method of measurement is performed by rocking the thin films sample around a small angle θ (or ω) while the detector is kept at a fixed 2θ angle. The detector measures the diffraction intensities from the preferentially-oriented lattice planes. In the Rigaku machine this measurement is called an ω scan. The degree (distribution) of preferred orientation is measured from the Full Width at Half Maximum (FWHM) of the rocking curve plot. This scan is often performed on thin films so the angles values are for the thin film peaks.

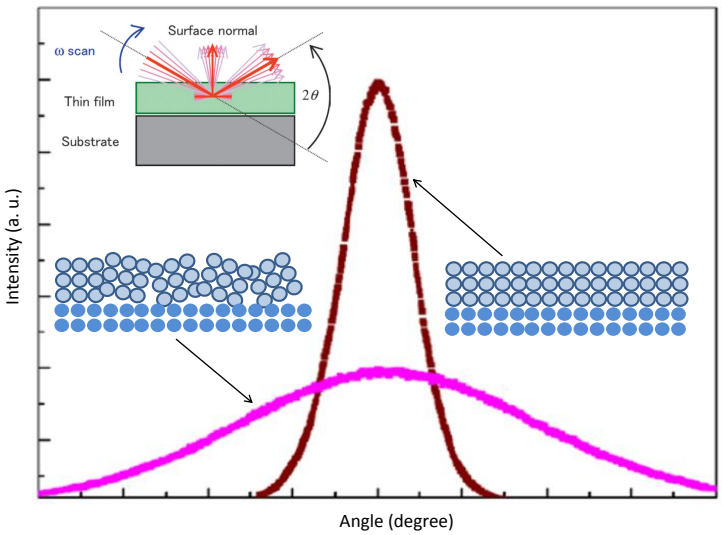

Figure 3.11: A schematic illustration of rocking curve measurement. An epitaxial thin film produces sharp peak, whereas a non-epitaxial film produces wide peak.

A perfect crystal (or a perfect epitaxial thin film) will produce a very sharp peak. Defects like mosaicity, dislocations and curvature create disruptions in the perfect parallelism of the atomic planes. The rocking profile from a perfect crystal will have some width due to instrument broadening and the intrinsic width of the crystal material.

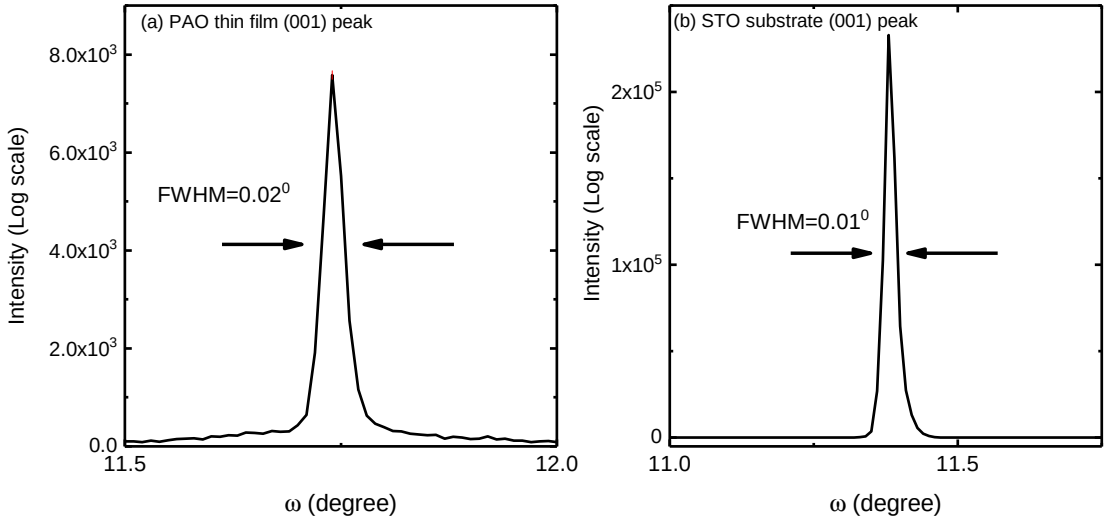

Figure 3.12: Rocking curve profile around the (001) peak for (a) PAO thin film and (b) STO substrate. The FWHM for the film and the substrate are 0.02° and 0.01°, respectively.

Fig. 3.12 shows the rocking curve profile for the PAO thin film and the STO substrate peak. The FWHM for the film is 0.02^0, which indicates that the film is quite epitaxial.

3.6 Electrical transport measurements

To electronically access the $LaAlO_3/SrTiO_3$ interface, which is buried underneath the insulating $LaAlO_3$, I used a wire-bonder. Contacts were made in a Van der Pauw geometry

by ultrasonic welding using a West Bond Inc. model 7476D manual aluminum wedge-wedge wire-bonder.

Transport properties were measured using a 9 T Quantum Design physical property measurement system (PPMS) using standard Van der Pauw (VDP) geometry in a DC set up down to 2 K. For measurement below 2 K, the helium-3 probe in our lab was used. For measuring sheet resistance R_s by PPMS, the machine provides two measured characteristic resistance R_A and R_B; Fig 3.13 shows the geometry for determining these two resistances.

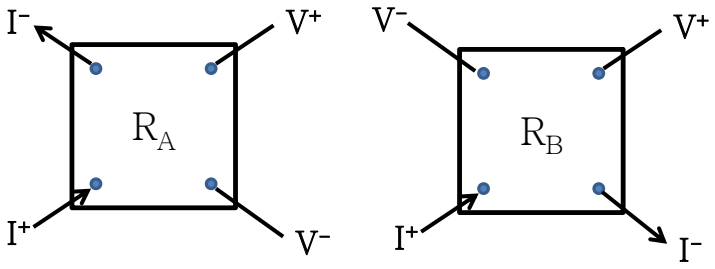

Figure 3.13: The two permutations that are used in the PPMS for determining the sheet resistance in the VDP configuration.

After obtaining these two resistances, R_s can be obtained numerically by solving the VDP equation [112]

$$e^{-\pi R_A/R_s} + e^{-\pi R_B/R_s} = 1 \tag{3.4}$$

One way to solve Eq. 3.4 is as follows:

– Calculate the initial value of the Z_i or Z_0

$$Z_0 = 2\ln(2)/[\pi(R_A + R_B)] \tag{3.5}$$

– Calculate the i^{th} iteration of

$$y_i = e^{-\pi R_A Z_i} + e^{-\pi R_B Z_{i-1}} \tag{3.6}$$

– Calculate the i^{th} iteration of Z_i, where

$$Z_i = Z_{i-1} - \frac{\pi(1 - y_i)}{R_A e^{-\pi R_A Z_i} + R_B e^{-\pi R_B Z_{i-1}}} \tag{3.7}$$

– You can stop the iteration, when the error in $(Z_i - Z_{i-1})/Z_i$ is small enough, *e.g.* within or better than 10^{-6}. Then, R_s is

$$R_s = 1/Z_i \tag{3.8}$$

If the thickness d of the electron gas is known, resistivity is $\rho = R_s d$. Often, R_{xx} is also used as a symbol for the longitudinal sheet resistance. Similarly, R_{xy} is used to indicate the Hall resistance.

Magnetoresistance (MR) and the Hall effect data were obtained in a magnetic field H up to 9 T. Hall resistance R_{xy} data provide the sheet carrier density n_s and the Hall mobility μ. For measuring the Hall resistance in the VDP geometry, current passes diagonally in the sample, as shown in Fig 3.14.

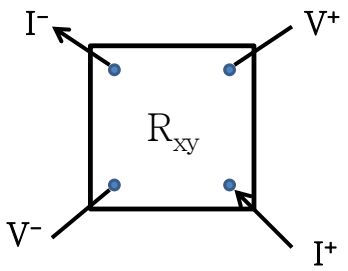

Figure 3.14: The configuration used to measure the Hall effect. To eliminated the effect of misalignments of contacts, the magnetic field was swiped from positive values to negative values.

There is always a misalignment of the electrode contacts, and that causes the R_{xx} or R_{xy} to have some portion of the other. We got rid off the Hall voltage contribution in magnetoresistance data by doing resistivity measurements at +/- H fields and then took the average of those two measurements. That removes the contribution from the Hall voltage, as the Hall voltage changes sign when the field changes direction (R_{xx} is an even function of magnetic filed, whereas R_{xy} is an odd function). Thus,

$$R_{xx}(H) = \frac{R_{xx}^{raw}(H) + R_{xx}^{raw}(-H)}{2} \tag{3.9}$$

Similarly, one can remove that magnetoresistance portion in the Hall data by

$$R_{xy}(H) = \frac{R_{xy}^{raw}(H) - R_{xy}^{raw}(-H)}{2} \tag{3.10}$$

Chapter 4

Effects of Oxygen Content on the $PrAlO_3/SrTiO_3$ Interface

4.1 Introduction

As was mentioned in Chapter 2, the growth parameters significantly affect the electrical and magnetic properties of $RAlO_3/SrTiO_3$ (R = rare earth) interfaces. In this chapter, I examine, in detail, the effects of oxygen content on the electrical and magnetic properties of $PrAlO_3$ (PAO) and STO for two main reasons. First, among the aluminates, PAO has the closest lattice constant to LAO (due to the multivalency of Ce, it is hard to make stable thin films of $CeAlO_3$), and thus this helps to lessen the effect of strain as much as possible. Second, the effective magnetic moment of the Pr^{3+} f electron states is 3.6 Bohr magnetons, while closed shell La^{3+} is diamagnetic [35], thus this rare-earth substitution can lead to magnetic properties in an aluminate structure. So, I prepared several PAO/STO interfaces under different oxygen pressures during growth and then analyzed the crystal structure and the surface morphology of the thin films. Finally, I examine the effects of oxygen pressure during growth on the Kondo effect and on the spin-orbit (SO) interaction, by measuring electric and magnetic properties.

4.2 $PrAlO_3$ thin films growth parameters

To study the effects of P_{O_2} on the electric and magnetic properties of the electron gas at the $PrAlO_3/SrTiO_3$ (PAO/STO) interface, several epitaxial films were made using PLD under various P_{O_2}. In this survey study, to keep the effect of the substrate defect constant, a single terminated substrate was cut into equal pieces to be used for depositing the different samples. Substrates from different companies might have different numbers of impurities and different miscut angles, so the effect of variations in those parameters are eliminated as much as possible.

PAO epitaxial thin films were prepared in the P_{O_2} range of $6 \times 10^{-6} - 1 \times 10^{-3}$ torr at 750°C. The laser pulse energy was 100 mJ, the fluence of the laser was ~ 3 J·cm^{-2} and the repetition rate was 1 Hz. After deposition, the samples were post annealed for 20 minutes and then cooled down to room temperature, both in the same oxygen pressure as during deposition. The growth oxygen pressures reported were from an ion gauge in close proximity to the substrate, but should be considered approximate, since pressure gradients are inherent between oxygen source and vacuum pump. The growth parameters are summarized in Table 4.1.

Table 4.1: PLD parameters used in thin film growth of $PrAlO_3$

P_{O_2} range	$6 \times 10^{-6} - 1 \times 10^{-3}$ torr
Laser fluence	~ 3 J·cm^{-2}
Repetition rate	1 Hz
Substrate temperature	750°C
Post annealing condition	20 min in the same P_{O_2} as during deposition

4.3 Surface analysis of the $PrAlO_3$ thin films

Figure 4.3 depicts the AFM topography of the PAO/STO sample grown at 1×10^{-4} torr. The thin film deposition has maintained the step terrace structure of the substrate, and thus this verifies that the growth is layer-by-layer growth. Similar step-flow growth were obtained for the other samples. Oxygen pressure during growth did not affect the topography of the samples.

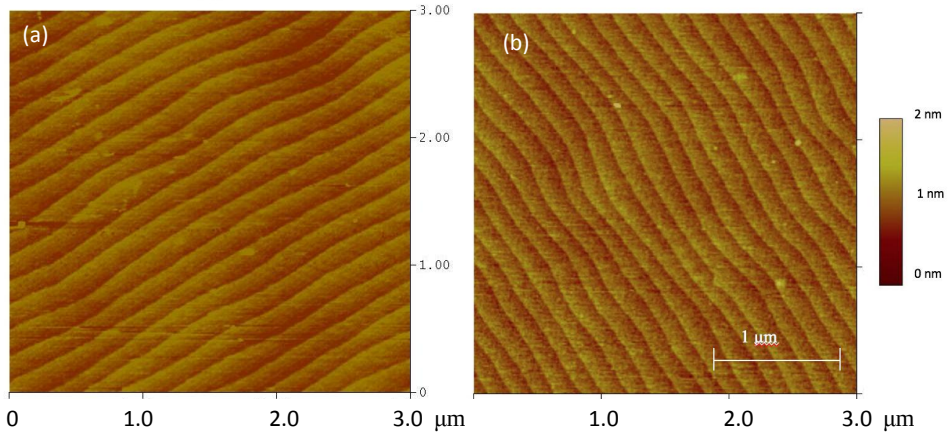

Figure 4.1: AFM topography of the TiO_2-terminated STO substrate (a) before the film deposition and (b) after the PAO film deposition (PAO/STO). The film was grown at 1×10^{-4} torr.

4.4 Crystal structure of the $PrAlO_3$ thin films

Figure 4.2 shows the XRD scan of the epitaxial PAO films on STO (001) that were grown at different P_{O_2}. The thin films were grown along the c-axis since only the (00ℓ) reflections of the PAO are present.

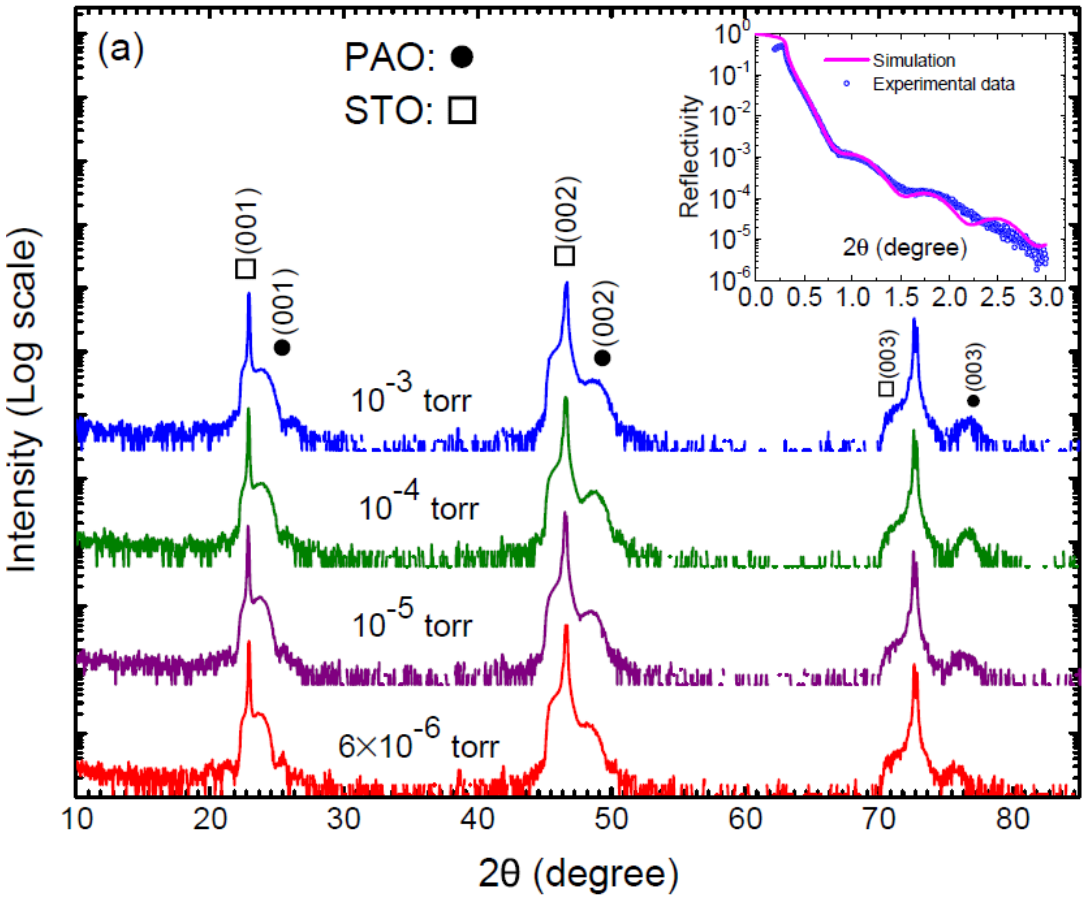

Figure 4.2: (Color online) XRD data for PAO/STO samples grown at different oxygen pressures. The XRR pattern of the 10^{-3} torr sample is shown in the inset (blue symbols). The pink line is a simulation.

The peaks for the substrate and the film are marked by rectangles and circles, respectively. To make the film peaks visible, the y-axis is plotted on a logarithmic scale. The interference fringes at the right side of the PAO (001) peaks are an indication of a very flat film of uniform thickness. In fact, fringes are present on the both sides of such peaks, but they are somewhat screened on the left side by the intense peak of the substrate. Using

Bragg formula, the c-axis lattice parameter can be calculated: $1/d^2 = l^2/c^2$. Where, l is the Miller index along the c-axis, and d is the spacing between the planes, which can be found from Eq. 3.2. The parameters are listed in Table 4.2.

Table 4.2: Out-of-plane lattice constants for thin films of $PrAlO_3$ grown at different P_{O_2}.

P_{O_2} (torr)	out-of-plane lattice constant
10^{-3}	3.738 ± 0.005 Å
10^{-4}	3.745 ± 0.005 Å
10^{-5}	3.751 ± 0.005 Å
6×10^{-6}	3.763 ± 0.005 Å

The out-of-plane constants are smaller than the bulk value (3.77 Å). This is expected, since the PAO films are subject to tensile strain in the in-plane directions from the STO substrate (the cubic lattice parameter of STO is 3.90 Å). Apparently, there is a trend toward relieving this strain for low oxygen films.

The inset in Fig. 4.2 shows an X-Ray Reflectivity (XRR) scan of the 1×10^{-3} torr sample. From a simulation fit, the thickness of this film is estimated to be 6.8 nm, or 18 unit cells (u.c.). Similar results were obtained for the other samples. There was no significant change in the structure, crystallinity, and quality of these samples as a function of oxygen pressure during growth.

4.5 Sheet resistance and Kondo effect

Transport properties were measured using a 9 T Quantum Design Physical Property Measurement System (PPMS) down to 2 K in a DC mode for resistive samples and an AC mode for the low resistance sample. The measurement was done in a Van der Pauw geometry,

and the Van der Pauw algorithm was used to find R_s. For temperature measurement below 2 K ($T \geq 0.3$ K), the helium-3 probe in our lab was used. In Fig. 4.3, the dependence on P_{O_2} of the sheet resistance R_s of the interfaces of PAO and STO is presented. We observe that the samples become less conductive for higher P_{O_2}. The room temperature resistivity increases as the samples are prepared at higher oxygen pressure. While there is only less than a factor of 2 in growth pressure difference between the 6×10^{-6} torr and 1×10^{-5} torr samples, their room temperature resistivities differ by three orders of magnitudes. In the case of the LAO/STO interface, it is known that oxygen vacancies can provide intragap donor levels close to the conduction band of STO [59]. Higher oxygen pressure during growth tends to fill the oxygen vacancies, thus causing the room temperature R_s to increase. The lowest oxygen-pressure-grown sample shows a metallic behavior from room temperature down to 2 K. The resistivity for this sample levels off below 10 K. We also treated an STO substrate under the deposition conditions, without an actual film on it, but it turned out to be very resistive and we were not able to measure any measurable conductance for it. This could be inherent to the PLD process; the energy of impinging ablated species favors oxygen loss at high temperatures and reducing atmosphere. The very low sheet resistance indicates that the conduction layer is much thicker for the 6×10^{-6} torr sample and the transport must occur in a region many layers thick.

For 10^{-5} and 10^{-4} torr O_2 growth pressure, the resistivity of the PAO/STO interface has a metallic trend from room temperature down to 50 K and 75 K, respectively, and a nonmetallic trend below those temperatures. For the 10^{-3} torr sample, a minimum of R_s occurs at a higher temperature of 150 K, and it is accompanied by an unusual maximum at around 57 K, and a second minimum at 32 K. Currently, we do not have a clear explanation

for the unusual maximum a around 57 K. We note that the temperature of the maximum coincides with the melting point of oxygen and may be related to variation in interstitial or interface-trapped oxygen mobility, as might be expected for this most over-oxygenated 10^{-3} torr sample.

Reference [113] has examined interfaces of $PrAlO_3$ and $NdAlO_3$ (NAO) with $SrTiO_3$ at $P_{O_2} = 10^{-3}$ torr. Our observed maximum at 57 K in R_s is absent in their data. This may be due in part to different absolute growth pressures.

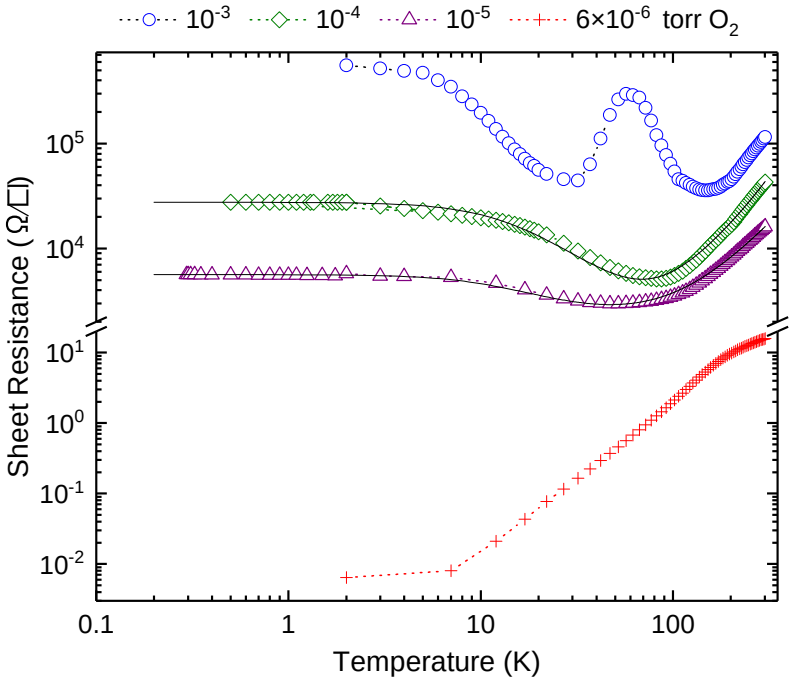

Figure 4.3: (Color online) Sheet resistance of PAO/STO interface synthesized at different oxygen pressure as a function of temperature. Solid curves are a fit using Eqs. 4.1 and 4.2.

At very low temperatures, all the samples, except the lowest P_{O_2} one, exhibit insu-

lating behavior by an upturn in R_s. The upturn is substantially stronger for the high P_{O_2} sample. The upturn in R_s at low temperatures has been seen in some of the reported results for the interface of $LaAlO_3/SrTiO_3$ that were grown at pressures higher than 1×10^{-4} torr, or in samples thicker than 15 u.c. [114]. These variations in R_s suggest that different types of transport mechanisms are operating at the interface. Some of the scattering processes that result in an upturn in resistivity are: scattering from localized magnetic moments (Kondo effect), weak localization (WL), and variable range hopping due to strong localization.

To see the behavior of sheet resistance at temperatures below 2 K, the helium-3 probe in our lab was used. We were able to take data down to 0.3 K for the 10^{-5} and 10^{-4} torr O_2 growth pressure interfaces.

The presence of a saturating resistance below T_m is the signature feature of the Kondo effect and our data are best fit to a Kondo model. In the Kondo model an impurity in a metal couples to reservoir of itinerant electrons by an antiferomagnetic exchange coupling forming a virtual bound state. This coupling can result in a contribution to the resistivity through a universal function of $R_K(T/T_K)$, in units of Kondo temperature (T_K).

Metallic resistance including a Kondo effect term is given by:

$$R^{fit}(T) = R_0 + \alpha T^2 + \beta T^5 + R_K(T/T_K) \tag{4.1}$$

Here, R_0 is the residual resistance due to disorder and impurities, αT^2 is the e-e interaction term and βT^5 is the contribution from the electron-phonon interaction, at temperatures well below the Debye temperature. $R_K(T/T_K)$ represents the contribution of magnetic Kondo scattering to electrical resistivity. $R_K(T/T_K)$ has a logarithmic trend at $T \gg T_K$ and a saturating behavior at $T \ll T_K$.

To fit our experimental data we used the empirical form of $R_K(T/T_K)$ presented by Costi [115] and Goldhaber [116], and later used by Lee *et al.* in Ref. [102] for undoped STO gated by an ionic gel electrolyte. They have demonstrated a Kondo effect, as a function of an applied electric field, which is the result of interaction between magnetic Ti^{3+} ions, unpaired and localized, with delocalized electrons that partially fill the Ti $3d$ band. The form is

$$R_K\left(\frac{T}{T_K}\right) = R_K(T=0)\left(\frac{T_K'^2}{T^2+T_K'^2}\right)^s \tag{4.2}$$

Here, T_K is defined as the temperature at which the Kondo resistivity is half of the value of the resistivity at zero temperature, $R_K(T_K) = R_K(T=0)/2$ so that:

$$T_K' = T_K/\sqrt{2^{1/s}-1} \tag{4.3}$$

Where, s is the effective spin of the magnetic scattering centers. We chose $s = 0.75$ for both the 10^{-5} and 10^{-4} torr samples. We first fit the model to the higher temperature part of the curve and extracted α, β and R_0, and then used these values for fitting at low temperatures (below 10 K) and found T_K. Table 4.3 summarizes the obtained values extracted from the fitting to Eqs. 4.1 and 4.2 across the whole measured temperature range.

Table 4.3: Parameters obtained from fitting sheet resistance data of Fig. 4.3 to Eq. 4.1 and 4.2.

P_{O_2} (torr)	10^{-5}	10^{-4}
s	0.75	0.75
R_0 (Ω)	2090	635
α (Ω/K^2)	0.153	0.39
β (Ω/K^5)	4.5×10^{-11}	3.6×10^{-9}
R_K(T=0) (Ω)	3500	27000
T_K (K)	16.1	18.3

From Table 4.3, we see a slight increase in the T_K values as the P_{O_2} is increased from 10^{-5} torr to 10^{-4} torr. Because the unusual mid-temperature peak in Fig. 4.3 for the 10^{-3} torr sample might affect the fitting results at the extreme temperatures on either end, we have not fit to the model for this sample.

4.6 Sheet carrier density and mobility

Fig. 4.4 shows the Hall resistance R_{xy} at 2 K as a function of magnetic field for the different interfaces. Hall resistance data was calculated by the method explained in Section 3.6.

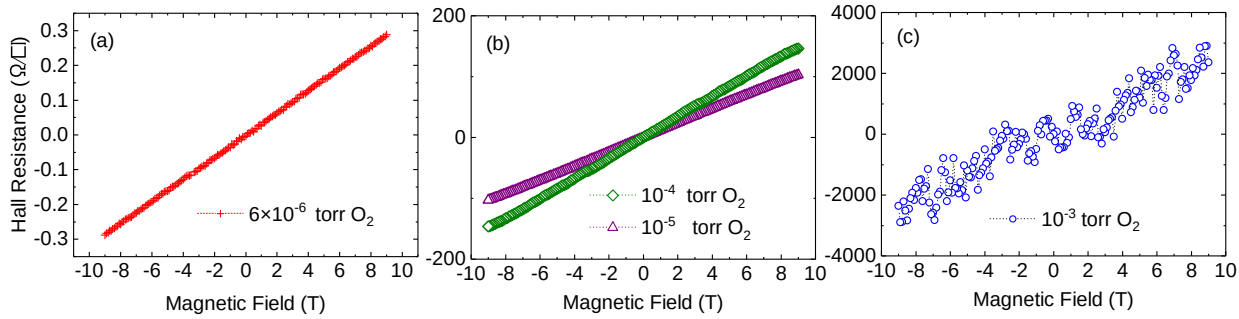

Figure 4.4: Hall resistance as a function of magnetic field at 2 K for the interfaces prepared at (a) $P_{O_2} = 6 \times 10^{-6}$, (b) $P_{O_2} = 10^{-5}$ and $P_{O_2} = 10^{-4}$, and (c) $P_{O_2} = 10^{-3}$ torr.

If we define the Hall coefficient R_H as

$$R_H \equiv \frac{dR_{xy}(H)}{dH} \tag{4.4}$$

The sheet carrier density (n_s) and the Hall mobility (μ) will be derived using the sheet

resistance R_s,

$$n_s = -\frac{1}{eR_H} \tag{4.5}$$

$$\mu = \frac{1}{en_sR_s} = \frac{R_H}{R_s} \tag{4.6}$$

R_{xy} is not necessarily always linear with the magnetic field. If there are two types of carriers such as electrons and holes, or two types of electrons (electrons in different energy bands), Hall data can be non-linear with the magnetic field. Throughout this part of the study, the Hall coefficient R_H was derived using a linear fitting to the Hall resistance.

The temperature dependences of the sheet carrier density (n_s) and mobility (μ) are displayed in Figs. 4.5 (a) and (b), respectively. The positive values for n_s indicate an electron-doped interface, and negative values indicate a hole-doped interface. For the $P_{O_2} = 10^{-6}$ torr sample, the carrier concentration is two orders of magnitude larger than the amount predicted by the polar catastrophe (3.2×10^{14} cm^{-2}, when half an electron per unit cell is transfered to the STO interface from LAO). The n_s values for the lowest P_{O_2} sample are so high that it resembles a bulk metallic sample. This implies that the oxygen vacancies or interdiffusion are contributing to the numbers of donors and creating a thick conducting region for the $P_{O_2} = 10^{-6}$ torr sample.

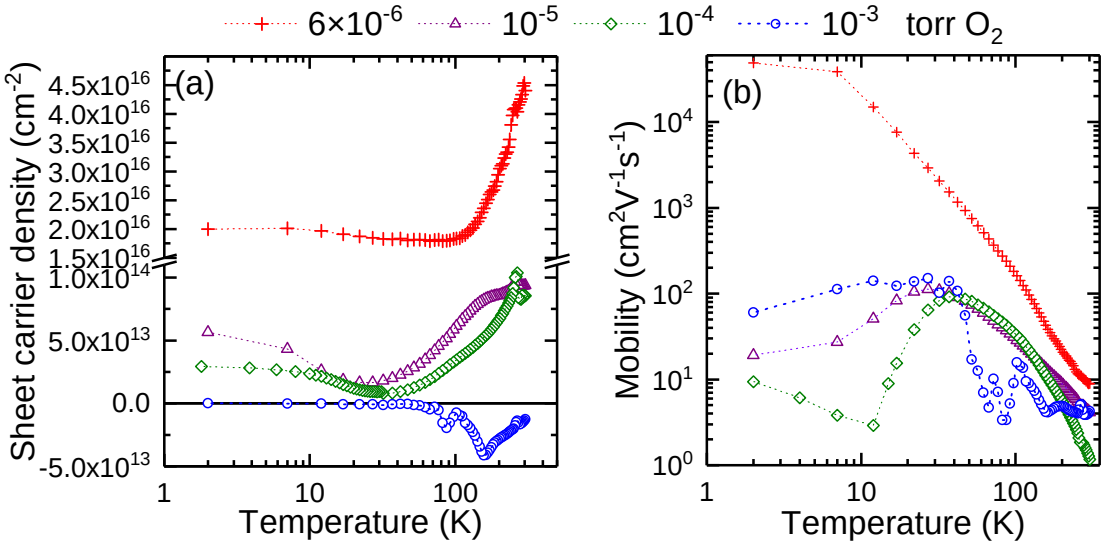

Figure 4.5: (Color online) Sheet carrier density, n_s (a) and Hall mobility, μ (b) as a function of temperature.

The behavior of n_s is rather complex and may involve two types of carriers freezing out at low temperatures for the $P_{O_2} = 10^{-3}$ torr interface. At higher temperatures, the 10^{-3} torr sample is predominantly doped with holes (possibly due to the interstitial or interface oxygen ions mentioned in the discussion of R_s), which eventually freeze out at low temperatures. At 2 K, the carriers are electrons with a concentration of 1.9×10^{11} cm^{-2}. For the 6×10^{-6} torr sample, the mobility monotonically increases by three orders of magnitude as the sample is cooled down from room temperature, Fig. 4.5 (b). For other samples μ drops by further cooling below 40 K, perhaps due to localization. There are some variations in n_s and μ at certain temperatures; those that happen at 150 K and 220 K are around the structural transitions of PAO in bulk. At room temperature, $PrAlO_3$ has a rhombohedral structure which transforms to an orthorhombic structure upon lowering the temperature to about 205–225 K, and to a monoclinic structure at about 151–175 K [55, 56]. The distinct

drop of n_s at 32 K has been previously seen for the NAO/STO interface [117] and for the LAO/STO [114] interface at around 20 K.

Surprisingly, the mobility values at low temperature are higher for the 10^{-3} torr sample than for the 10^{-4} torr sample, despite the latter having a higher resistance and lower n_s at low temperatures. This could be in part due the difference in the number of defects or impurities in the two samples, for example, minimal oxygen vacancy defects in the 10^{-3} torr sample.

4.7 Magnetoresistance and spin orbit interaction

Figure 4.6(a) shows the magnetic field dependence of the magnetoresistance (MR) at 2 K. MR data are calculated as $\mathrm{MR} = [R(H) - R(0)]/R(0) \times 100\%$. The measurement was done both with the magnetic field H perpendicular to the interface plane (out-of-plane MR), Fig. 4.6 (a), and with the magnetic field H parallel to the interface plane (in-plane MR), Fig. 4.6 (b).

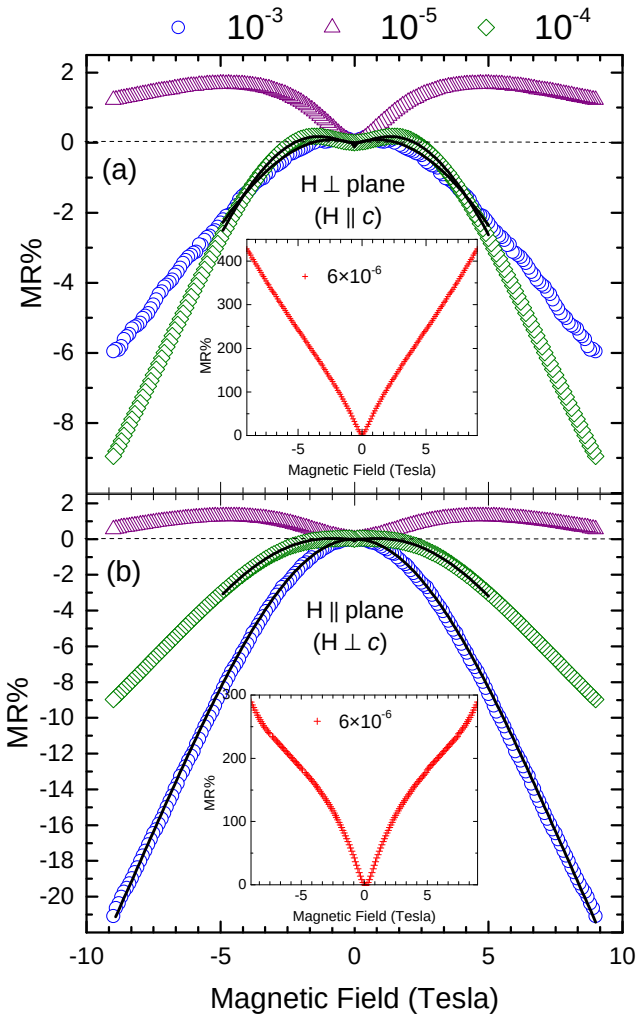

Figure 4.6: (Color online) MR of PAO/STO interfaces at 2 K. The magnetic field is applied (a) out of the plane and (b) in the plane of the substrate. Insets show MR data for 6×10^{-6} torr sample. Solid curves are fits according to Eq. 4.8.

For the 6×10^{-6} torr sample, MR values are positive for all measured fields and are immensely large [insets of Figs. 4.6 (a) and (b)]; the field dependence resembles some bulk metals. Very high positive MR has also recently been reported in degenerate semiconductive

STO single crystals capped with ultra thin STO/LAO bilayers [118].

For higher P_{O_2} samples, the MR data has a positive slope at low fields and a negative slope at high fields, resulting in a local maximum in the MR. These variations indicate that at least two different field-dependent scattering processes operate at the interface. The maximum of the MR shifts to a lower field as the oxygen pressure during growth increases. For the 10^{-3} torr sample the positive part of the MR is small.

A MR anisotropy investigation [119] for 26 u.c. $LaAlO_3$ on $SrTiO_3$ showed that the sign of the MR does not depend on the field direction for low P_{O_2} samples, considered to be 3D samples (both the out of plane and in-plane MRs are positive for fields up to 9 T). However, for high P_{O_2} LAO/STO the 2D samples, the sign of the MR changed from positive values in the out-of-plane geometry to negative values in the in-plane field orientation. For both 2D and 3D LAO/STO interfaces, the magnitude of the MR values are smaller when the field is in the plane of the interface. MR was observed to be negative for 12 u.c. of NAO/STO grown at 7.5×10^{-3} torr [117].

We attribute the positive part of the MR to strong spin-orbit (SO) scattering and the negative part to the Kondo mechanism. The SO interaction has been shown to be very strong in some of the semiconductor heterostructures such as p-type GaAs/$Al_xGa_{1-x}As$ [120], and in topological insulators [121, 122]. The constructive interference between time-reversed waves of carriers in a disordered material leads to the weak localization (WL) effect [123]. Applying a magnetic field perpendicular to the plane of motion of carriers inhibits the WL and causes a negative MR at small magnetic fields. A strong SO interaction decreases the probability of carriers backscattering and counteracts weak localization. This effect is called weak anti-localization (WAL) and leads to a positive MR at small fields.

The conduction electrons confined in the vicinity of the polar RAO/STO interface experience a strong electric field perpendicular to the interface as the result of broken inversion symmetry. In the carriers' rest frame, this electric field appears as an internal magnetic field at the interface plane, perpendicular to their wave vector. As a result, the spins of electrons couple to the internal magnetic field which leads to a large Rashba SO interaction whose magnitude is tunable by the application of an external electric field [86]. We use the same analogy to fit the MR data for our samples. We fit the positive MR data for the 10^{-5} torr sample with the Hikami-Larkin-Nagaoka (HLN) theory [99]. HLN theory considers the effect of SO scattering, random magnetic impurity scattering, magnetic field, and inelastic collisions on the quantum backscattering interference, and is expressed as a change in conductivity:

$$\begin{aligned}\Delta\sigma(H) = -\frac{e^2}{\pi h}\Bigg[&\frac{1}{2}\Psi\left(\frac{1}{2}+\frac{H_\varphi}{H}\right) - \ln\left(\frac{H_\varphi}{H}\right) \\ &- \Psi\left(\frac{1}{2}+\frac{H_\varphi+H_{SO}}{H}\right) + \ln\left(\frac{H_\varphi+H_{SO}}{H}\right) \\ &- \frac{1}{2}\Psi\left(\frac{1}{2}+\frac{H_\varphi+2H_{SO}}{H}\right) + \frac{1}{2}\ln\left(\frac{H_\varphi+2H_{SO}}{H}\right)\Bigg]\end{aligned} \tag{4.7}$$

where σ is the longitudinal conductivity and is calculated from the inversion of the measured resistivity matrix. $\Delta\sigma(H) = \sigma(H) - \sigma(0)$, $\Psi(x)$ is the digamma function, $e^2/\pi h$ is the universal value of conductance, and $H_\varphi = \hbar/4eD\tau_\varphi$. D and τ_φ are the diffusion constant and phase coherence time (inelastic scattering time), respectively. $H_{SO} = \hbar/4eD\tau_{SO}$ is the field at which the SO interaction is no longer effective and the positive WAL magnetoresistance becomes the negative WL magnetoresistance. τ_{SO} is the SO scattering time. HLN theory was derived for materials in which the spin-splitting energy is proportional to k^3, which is

the case in $SrTiO_3$[101]. We treated both H_{SO} and H_φ as fitting parameters and the good quality of the fit in a wide magnetic field range is shown for the 10^{-5} torr sample in Fig. 4.7. While HLN theory is significant only in the diffusive regime, the fit, however, is shown for a wide magnetic field range. We obtained $H_\varphi = 0.33$ T and $H_{SO} = 1.25$ T for perpendicular, and $H_\varphi = 0.50$ T and $H_{SO} = 1.25$ T for parallel magnetic field orientations, respectively, for the 10^{-5} torr sample.

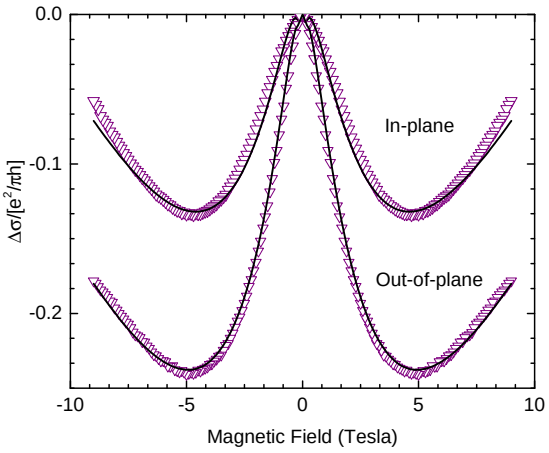

Figure 4.7: Dependence of magneto-conductance, expressed in units of $e^2/\pi h$, on magnetic field at 2 K for the 10^{-5} torr oxygen growth pressure sample for both field orientations. Black lines are fit to Eq. 4.7.

As the P_{O_2} is increased the positive part of the MR becomes smaller. The 10^{-4} torr sample has positive MR at magnetic fields near $H = 0$. The maximum of its MR happens at 1.5 T; for the 10^{-3} torr sample, at 0.5 T. To fit the experimental data for samples grown at $P_{O_2} = 10^{-4}$ and 10^{-3} torr to theory, we add the WAL positive MR, due to strong SO interaction, to the negative Kondo MR:

$$R\left(H\right) = R_0 + R_K\left(\frac{H}{H_1}\right) + c\left[\Psi\left(\frac{1}{2}+\frac{H_\varphi}{H}\right) - \ln\left(\frac{H_\varphi}{H}\right)\right] \tag{4.8}$$

where c is a constant and H_1 is a magnetic field scale which is related to both T_K and the g-factor of the impurity spin. $R_K(H/H_1)$ is the zero temperature Kondo-magnetoresistance (taken at 2 K for our data), which is expressed in Ref. [124] as:

$$R_K\left(\frac{H}{H_1}\right) = R_K(H=0)\cos^2\left(\frac{\pi}{2}M\left(\frac{H}{H_1}\right)\right) \tag{4.9}$$

$M(\frac{H}{H_1})$ is the magnetization of a Kondo impurity at zero temperature and is given by:

$$M(\frac{H}{H_1}) = \begin{cases} \frac{1}{\sqrt{2\pi}}\sum_{i=0}^{\infty}(-\frac{1}{2})^i(i!)^{-1}(i+\frac{1}{2})^{(i-\frac{1}{2})}\mathrm{e}^{-(i+\frac{1}{2})}\left(\frac{H}{H_1}\right)^{2i+1} & H \le \sqrt{2}H_1 \\ 1-(\pi)^{-3/2}\int\frac{dt}{t}\sin(\pi t)\mathrm{e}^{-t\ln(t/2e)}\left(\frac{H}{H_1}\right)\Gamma(t+1/2) & H \ge \sqrt{2}H_1 \end{cases} \tag{4.10}$$

This interpretation was previously used by Lee *et al.* [102] in electrolyte-gated STO to explain the negative MR regime, and by Das *et al.* [104] in $LaTiO_3/SrTiO_3$ δ-doped with $LaCrO_3$ to explain the small positive MR which is followed by a transition to a negative MR regime. The result of fitting to Eq. 4.8 is shown with black solid lines in Fig. 4.6. The WAL effect is meaningful for small fields, $H < H_{SO}$, thus we only fit the data for small field range. The fitting parameters are listed in table 4.4.

Table 4.4: Parameters extracted from fitting the MR data in Fig. 4.6 to Eq. 4.8.

P_{O_2} (torr)	Out-of-plane			In-plane		
	H_1(T)	H_φ(T)	c	H_1(T)	H_φ(T)	c
10^{-4}	11.4	0.46	800	11.6	0.52	800
10^{-3}	15	0.15	30000	8.72	–	0

The difference between weak anti-localization in normal and in-plane magnetic fields for thin films contains information about the effective dimensionality of the carrier system. For in-plane fields, if the effective thickness of the carrier system is smaller than the magnetic length (at low fields), then the weak anti-localization magnetoresistance is affected [125, 126]. When the field is brought from being perpendicular [Fig. 4.6 (a)] to being parallel to the interface [Fig. 4.6 (b)], there is no sign change in the MR values. For the in-plane geometry, for the 6×10^{-6} torr sample, a change in curvature appears for $H > 5$ T, which implies the presence of an additional scattering mechanism that becomes active at higher fields. There is not much change for the 10^{-5} torr sample; the MR values and the overall shape of the MR curves in both directions for this sample are very similar. Thus, for this sample, the 2DEG is thicker than the magnetic length. However, the 10^{-4} torr and 10^{-3} torr samples are affected by the change in the orientation of the magnetic field: as shown in Fig. 4.6 (b), the positive part of the MR at low fields becomes smaller for the 10^{-4} torr sample and it is negligible for the 10^{-3} torr sample. For the 10^{-3} torr sample, in which there are very few oxygen vacancies present, the MR values for the in-plane field orientation are larger than the corresponding out-of-plane MR data. We expect that the thickness of the 2DEG is smaller than the magnetic length for these two interfaces. Thus, the MR of the 10^{-4} and 10^{-3} torr samples are in accord with the 2D nature of the interface for these materials.

4.8 Summary

In summary, we examined the behavior of the conductivity at the interface between $PrAlO_3$ and $SrTiO_3$; we studied the electric and magnetic transport properties of interfaces of PAO/STO grown at oxygen pressures in the P_{O_2} range of $6 \times 10^{-6} - 1 \times 10^{-3}$ torr. Overall,

differences between $PrAlO_3$ and $LaAlO_3$ were subtle, much smaller than the effects of oxygen content changes. These indicate that Pr ions near the interface are predominantly trivalent, with relatively localized magnetism. The most-conducting 2-D-like Pr samples were not as conducting as comparable La samples, indicting either that a steric effect, or a slightly mixed-valent nature of Pr, may be detrimental to conductivity at the interface. The least-conducting, most oxygenated Pr interface exhibits hole conductivity at low temperatures, a departure from the usual electron-doped behavior of the better-conducting interfaces; the smaller and more electropositive Pr ions may permit more interstitials or interfacial oxygen, providing residual hole doping after n-type carriers are compensated or freeze out.

For the 6×10^{-6} torr sample, the very small value of R_s at low temperature, large carrier concentration, high mobilities, and very high positive MR values indicate it is like a bulk metal, likely due to extensive oxygen defects and/or interdiffusion. As the interfaces are grown at higher oxygen pressures, resistivity behavior characteristic of nearly two-dimensional transport occurs; for 10^{-5} and 10^{-4} torr, high-temperature metallic behavior with increasing R_s is accompanied by an upturn at low temperature, consistent with Kondo scattering theory. Analysis of the R_s data gives Kondo temperature $\sim$ 16 K and $\sim$ 18 K for the 10^{-5} and 10^{-4} torr samples, respectively. The MR values for the $P_{O_2} \geq 10^{-5}$ torr samples were modeled with their positive part due to WAL because of a strong SO interaction and their negative part due to the Kondo effect. The variation of MR values suggests a strong SO interaction for the 10^{-5} torr sample with $H_{SO} = 1.25$ T in both field orientations. The positive part of the MR shrinks for the 10^{-4} torr sample. For this interface the MR is dominated by negative Kondo MR at high fields.

The data presented in this chapter are published in Ref.[127]. The interesting Hall and

magnetoresistance data encouraged us to do a more detailed study of these measurements at different temperatures. The results are presented in the subsequent chapter.

Chapter 5

Multiband Conduction at the $PrAlO_3/SrTiO_3$ Interface

5.1 Introduction

As was mentioned in Chapter 2, in order to avoid the diverging potential that takes form when LAO is depositing on STO, a half electron per unit cell should transfer to the interface. This electronic reconstruction should lead to an electron carrier density of 3×10^{14} cm^{-2}, as predicted by theory. However, the number of carriers measured by experiments such as the Hall effect data [128] are roughly one order of magnitude smaller. So, the question arises about the "missing" electrons. An answer to this question is given based on the assumption that there are two types of carriers at the interface: one population that is strongly localized by impurities and defects and has a high carrier density, while the other population has a high mobility and a low carrier density. Such multiband conduction, which manifest itself in nonlinear Hall data has been reported for the 2DEG at the LAO/STO interface [129, 130]. In this chapter, I show that multiband conduction also likely happens for the PAO/STO interface. If the interfaces are grown at low P_{O_2}, Hall effect data suggest that the transport is dominated by one type of carrier. For the interfaces that are grown at high P_{O_2}, at low and high temperatures, $T < 5$ K and $T > 50$ K, the Hall data could be described by a single channel of electron carriers with a low mobility. However, at intermediate temperatures, 10 K $< T <$ 40 K, the Hall data becomes noticeably nonlinear, with positive out-of-plane and in-plane magnetoresistance. The nonlinear Hall resistance

can be described by a two-band model with different electron charge carrier types.

5.2 Thin film fabrication and characterization

To better understand the anisotropy in the magnetoresistance data and nonlinearity in the Hall that was observed in Chapter 4, we prepared two different interfaces of PAO/STO: one was synthesized at the $P_{O_2} = 10^{-5}$ torr and the other at 10^{-4} torr. These two samples are 15 u.c., which are thinner than the thin films presented in Chapter 4. Fig. 5.1 shows AFM images of these two samples.

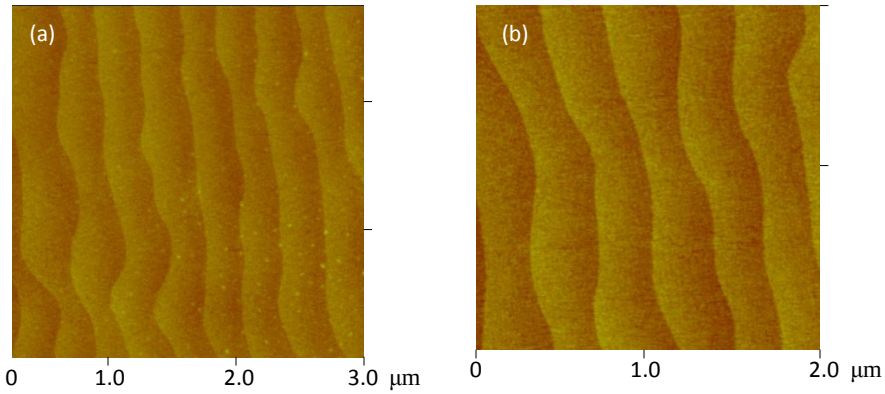

Figure 5.1: AFM images of PAO/STO thin films that were fabricated at (a) $P_{O_2} = 10^{-5}$ torr and (b) $P_{O_2} = 10^{-4}$ torr. This range of oxygen pressure during growth appears to have no effect on the topography of the samples.

5.3 Dependence of the sheet resistance on the magnetic field orientation

The sheet resistance was measured for different magnetic field orientations: at zero field, 9 T field applied perpendicular and parallel to the interface, and -9 T field applied

perpendicular and parallel to the interface. The results for the $P_{O_2} = 10^{-5}$ and 10^{-4} torr interfaces are presented in Figs. 5.2 (a) and (b), respectively.

I should note that the exact values of resistance for this set of samples should not be compared to the set of thin films presented in Chapter 4; the resistivity trend should rather be compared. This is because that these samples were synthesized on substrates that were from a different company, and also the beam splitter of the laser of the PLD was changed. These interfaces are very sensitive to the growth conditions, and small changes may result in different values of resistance.

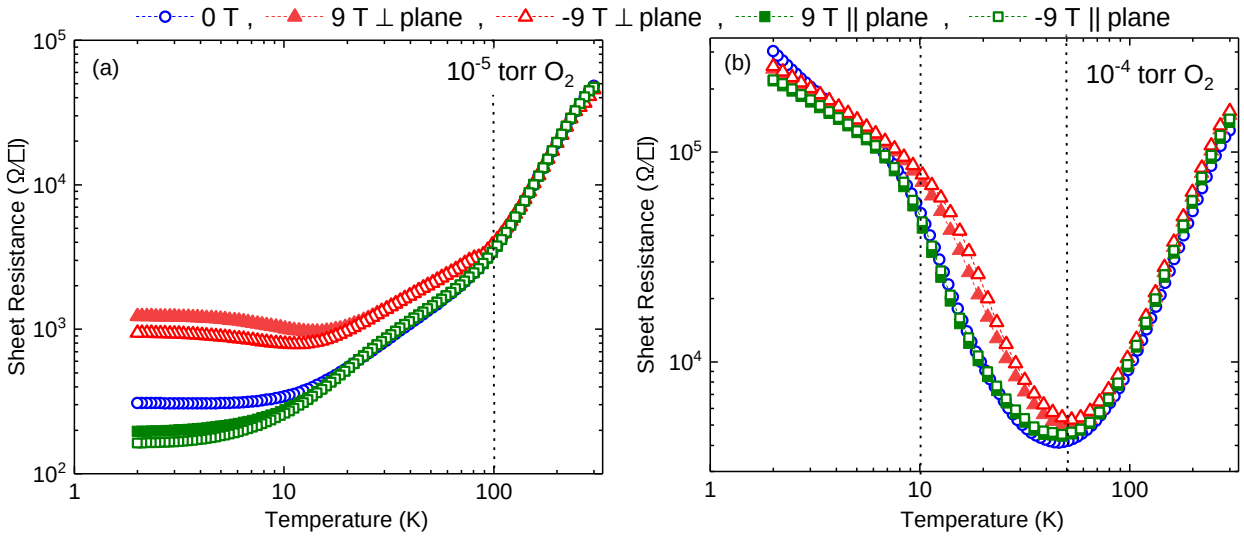

Figure 5.2: Dependence of the sheet resistance on temperature, at different magnetic field directions for 15 monolayers of PAO on STO that were fabricated at (a) $P_{O_2} = 10^{-5}$ torr and (b) $P_{O_2} = 10^{-4}$ torr. The dotted lines distinguish the temperature regions where the magnetic field has a pronounce effect.

At zero field, from Fig. 5.2 (a) we see a normal metallic behavior for the 10^{-5} torr

sample. For the 10^{-4} torr sample, Fig. 5.2 (b), we see a metallic behavior down to 50 K, below which the resistivity shows an upturn that becomes less steep below 10 K. The behavior is similar to what was observed in the previous chapter. For the 10^{-5} torr sample, at high temperatures, $T > 100$ K, the magnetic field does not have a profound effect on the resistivity. However, a 9 T magnetic field applied perpendicular to the interface results in an immense increase of about one order of magnitude in the resistance at low temperatures. Interestingly, applying a magnetic field in the plane of the interface reduces the resistance. We can deduce that there magnetic moments present in the sample and the electrons scatter from them much more when those moments are aligned perpendicular to the interface.

Preparing the interface at a higher P_{O_2}, which effectively results in less oxygen vacancies, suppresses these effects at low temperatures. As can be seen in Fig. 5.2 (b), the magnetic field has the most effect at intermediate temperatures, 10 K $< T <$ 50 K, as shown by the dotted lines in the figure. Results from the Hall data shed more light on the electronic properties of the interface in this intermediate temperature range.

5.4 Nonlinear Hall resistance

Fig. 5.3 shows Hall resistance over the temperature range of 2–100 K for the two samples. To get the data, the magnetic field was swiped from +9 T to −9 T at each temperature and the magnetoresistance portion is also been removed to symmetrize the data (see Section 3.6). For the 10^{-5} torr sample at high temperatures, Fig. 5.3 (a), $T \geq 50$ K, the Hall resistance is perfectly linear and it changes by about a few 100 Ω over a field of 9 T. By lowering the temperature, the slope of the Hall resistance as a function of magnetic field monotonically increases (indicating a decrease in the number of carriers). A very small

deviation from a linear relation can be observed at 5 K. For this sample, the number of the carriers and mobility, which are shown in Fig. 5.3, are calculated based on a linear fit to the Hall resistance data.

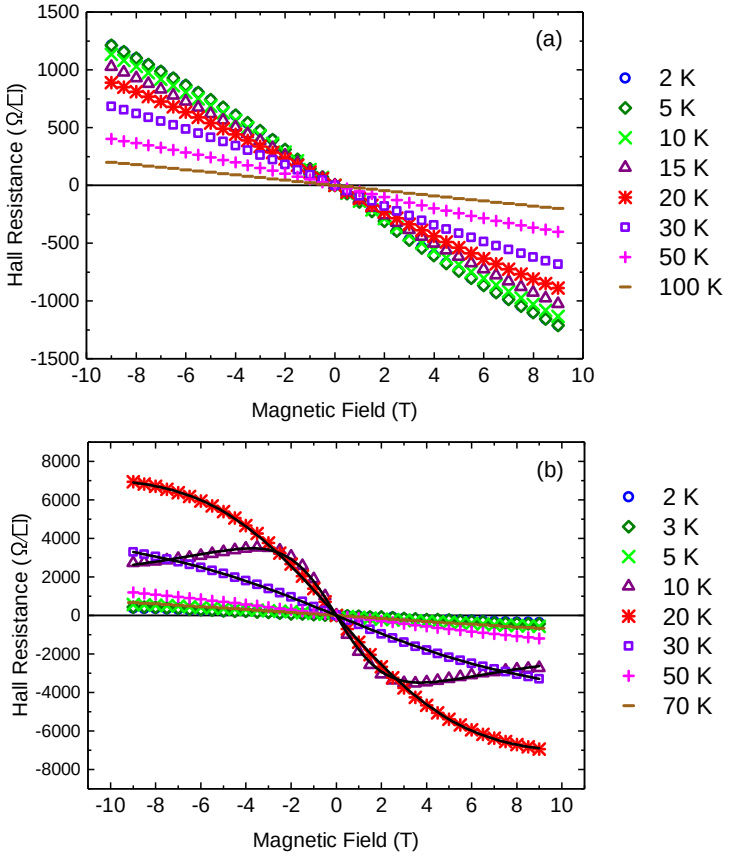

Figure 5.3: Hall resistance as a function of magnetic field for the $PrAlO_3/SrTiO_3$ interface: (a) $P_{O_2} = 10^{-5}$ torr sample and (b) $P_{O_2} = 10^{-4}$ torr sample, at different temperatures. The Hall data becomes distinctly nonlinear at $T = 20$ K and $T = 10$ K for the 10^{-4} torr sample. Black lines are fits to Eq. 5.2.

Interesting Hall data was observed for the high P_{O_2} sample. For the 10^{-4} torr sample, Fig. 5.3 (b), at low and high temperatures, $T < 5$ K and $T > 50$ K, the Hall resistance is

linear and does not depend significantly on the temperature. However, over on intermediate temperature range 5 K $\leq T \leq$ 50 K, which is shown between the dash lines in Fig. 5.2 (b), the Hall resistance is distinctly nonlinear; this is the region where the magnetic field has a strong effect on the resistivity (large positive magnetoresistance). The observation of an S-shape Hall trend along with a large magnetoresistance suggest multiband conduction. Perhaps, two separate bands of charge carriers contribute to the transport. Thus, we assume that two types of electron carriers with number densities of n_1 and n_2 and mobilities of μ_1 and μ_2, participate in the interfacial conduction. The longitudinal R_{xx} and transverse R_{xy} resistances for a sample with two types of carriers are [14]

$$R_{xx}(B=0) = \frac{1}{e(n_1\mu_1 + n_2\mu_2)} \tag{5.1}$$

$$R_{xy}(B) = \frac{B}{e}\frac{n_1\mu_1^2 + n_2\mu_2^2 + (\mu_1\mu_2 B)^2(n_1+n_2)}{(n_1\mu_1 + n_2\mu_2)^2 + (\mu_1\mu_2 B)^2(n_1+n_2)^2} \tag{5.2}$$

One way to solve for the four unknowns of n_1, n_2, μ_1, and μ_2 from the two above equations is to define some variables, as follows

$$\rho = \frac{1}{e(n_1\mu_1 + n_2\mu_2)} \tag{5.3}$$

$$R_0(B \longrightarrow 0) = \frac{n_1\mu_1^2 + n_2\mu_2^2}{e(n_1\mu_1 + n_2\mu_2)^2} \tag{5.4}$$

$$R_\infty(B \longrightarrow \infty) = \frac{1}{e(n_1+n_2)} \tag{5.5}$$

Also, define μ as

$$\mu^2 \equiv \frac{(n_1+n_2)^2\mu_1^2\mu_2^2}{(n_1\mu_1 + n_2\mu_2)^2} = \rho^2 R_\infty^{-2}\mu_1^2\mu_2^2 \tag{5.6}$$

These conversions help to find a more compact form for the Hall resistance

$$R_{xy}(B) = \frac{R_0 B + R_\infty \mu^2 B^3}{1 + \mu^2 B^2} \tag{5.7}$$

Equation 5.7 is now easier to work with. R_0 can be read from the data, and μ and R_∞ could be set as the fitting parameters. Our original four unknowns are

$$\mu_1 = \frac{R_0\rho^{-1} + \mu + \sqrt{(R_0\rho^{-1} + \mu)^2 - 4\rho^{-1}\mu R_\infty}}{2} \tag{5.8}$$

$$\mu_2 = \frac{R_0\rho^{-1} + \mu - \sqrt{(R_0\rho^{-1} + \mu)^2 - 4\rho^{-1}\mu R_\infty}}{2} \tag{5.9}$$

$$n_1 = \frac{e^{-1}\rho^{-1} - R_\infty^{-1}e^{-1}\mu_2}{\mu_1 - \mu_2} \tag{5.10}$$

$$n_2 = \frac{-e^{-1}\rho^{-1} + R_\infty^{-1}e^{-1}\mu_1}{\mu_1 - \mu_2} \tag{5.11}$$

The black lines in Fig. 5.3 (b) are the results of fitting the Hall data to the above equations. The fits are in good agreement with the experimental data.

5.4.1 Sheet carrier density and mobility using two-band model

The temperature dependence of the carrier densities n_1 and n_2, and mobilities μ_1 and μ_2 for the 10^{-4} torr sample are shown in Fig. 5.4 (a) and (b), respectively. For the temperature range of $T < 5$ K and $T > 50$ K, where the Hall data is linear, the carrier density for one-type carrier is obtained from a linear fit to $R_{xy} = B/en$, and the mobility is obtained from $R_{xx} = 1/en\mu$. The carrier concentration for the first type of carrier is around

$n_1 = 10^{13}$ cm^{-2}, and is higher than the concentration for the second type of carrier n_2. As can be seen, n_2 is much more temperature-dependent than n_1; its values change by about five orders of magnitude as the temperature is lowered from 100 K to 5 K.

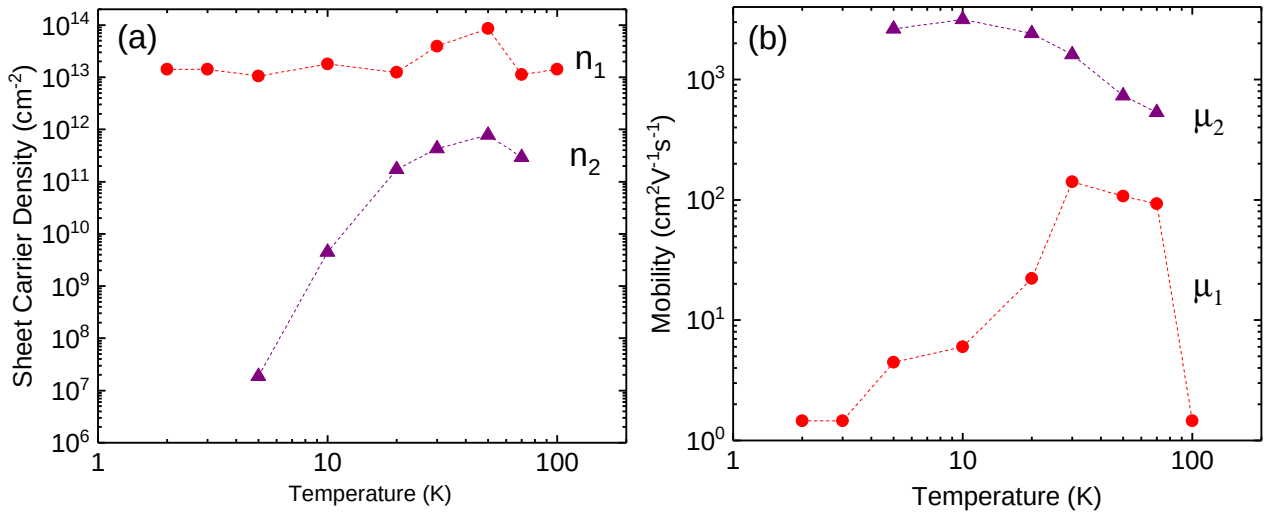

Figure 5.4: (a) Charge carrier densities n_1 and n_2, and (b) mobilities μ_1 and μ_2 for the 10^{-4} torr sample of $PrAlO_3/SrTiO_3$ (001). The values are obtained using a two-band model. The dotted lines are guides to the eye.

Mobilities for the second type of carriers μ_2, are higher than the mobility values for the first type of carriers μ_1. At 5 K, $\mu_2 \sim 3000$ cm^{-2}V^{-1}s^{-1}; whereas, $\mu_1 \sim 5$ cm^{-2}V^{-1}s^{-1}. The two types of carriers have very different mobility behavior as a function of temperature. μ_1 decreases and μ_2 increases as the temperature is lowered. We assume that n_2 is a thermally activated electron band, which has a thermally activated behavior of $n_2 \propto \exp(-\Delta/k_B T)$. Where, k_B is the Boltzmann constant and Δ is the gap for thermally activating the electrons. This activation energy can be found by a linear fit to the plot of $\ln(n_2)$ versus the inverse of temperature. The result of the fitting is shown in Fig. 5.5 and the gap is found to be

$\Delta = 4.9$ meV.

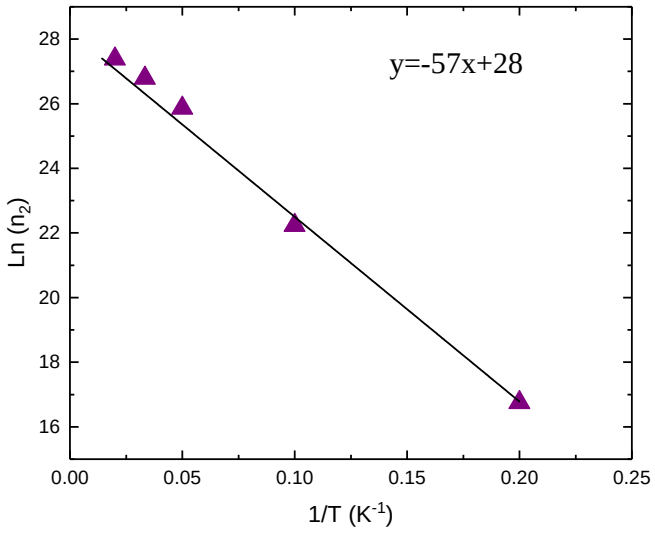

Figure 5.5: Arrhenius plot for the low population type of carriers. The line is an exponential fit to extract the band gap.

5.5 Anisotropy in magnetoresistance

Magnetoresistance (MR) for the two interfaces was measured in three different magnetic field orientations: the magnetic field was applied perpendicular to the plane of the interface (the normal out-of-plane MR, $MR_{\perp}$), the magnetic field was applied in the plane of the interface and parallel to the current, and the magnetic field was applied in the plane of the interface and perpendicular to the current. The diagrams next to the plots in Fig. 5.6 shows the geometry of the magnetic field with respect to the current.

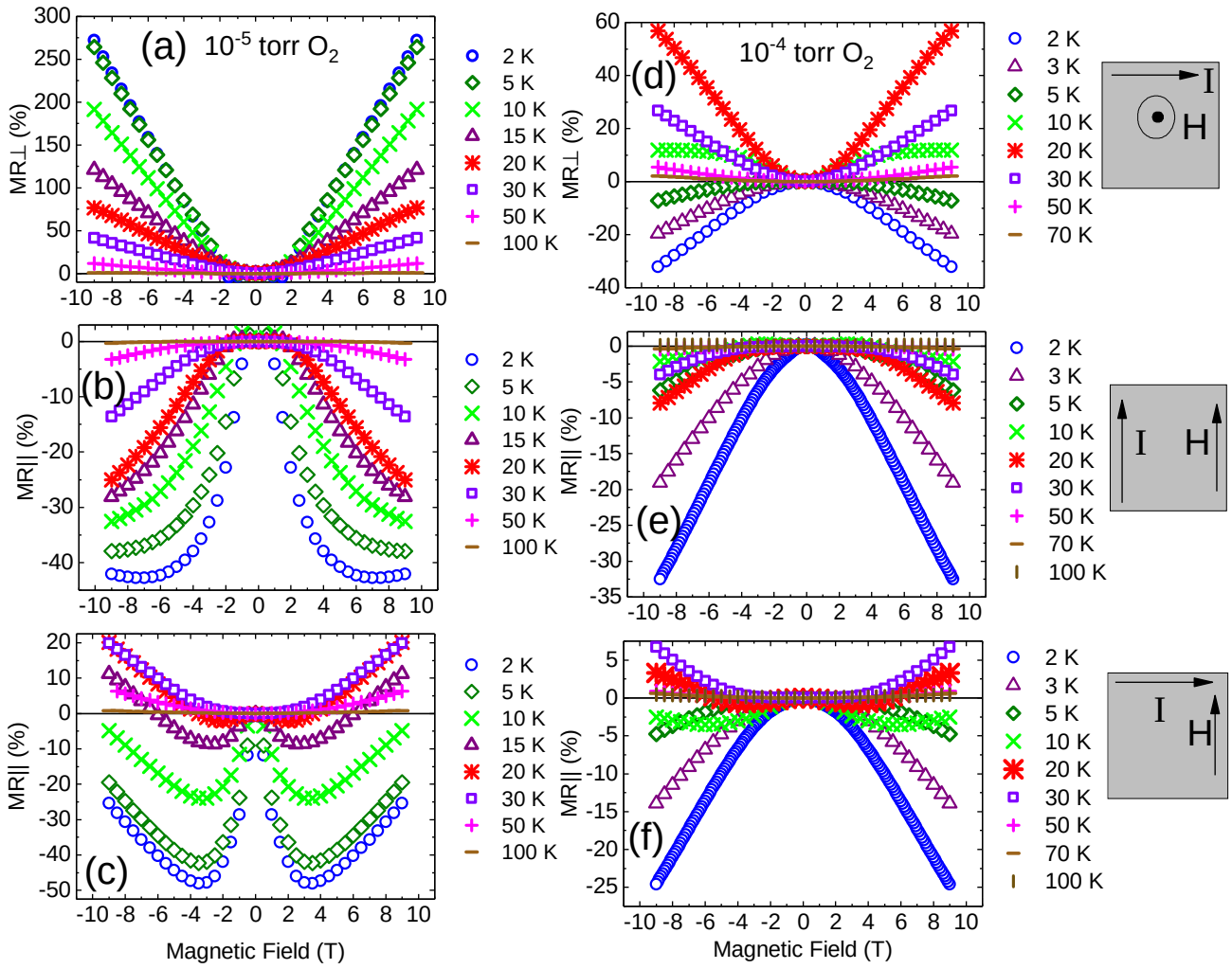

Figure 5.6: (a) Out-of-plane magnetoresistance for the 10^{-5} torr sample. (b) In-plane magnetoresistance for the 10^{-5} torr sample. Magnetic field and current are parallel. (c) In-plane magnetoresistance for the 10^{-5} torr sample. Magnetic field and current are perpendicular. (d) Out-of-plane magnetoresistance for the 10^{-4} torr sample. (e) In-plane magnetoresistance for the 10^{-4} torr sample. Magnetic field and current are parallel. (f) In-plane magnetoresistance for the 10^{-4} torr sample. Magnetic field and current are perpendicular.

In the out-of-plane geometry, where the magnetic field is always perpendicular to the

current, scattering arises predominately during cyclotron motion due to the Lorentz force. In the parallel geometry of Figs. 5.6 (b) and (e), the Lorentz force is zero. But there could be MR if spin-dependent scattering events are present in the system. At low temperatures, the magnetic field can align the spins in the plane of the interface in a magnetic system, and this could result in different scattering processes. This MR geometry is useful to separate orbital scattering and spin-dependent scattering. In the MR mode of Figs. 5.6 (c) and (f), with the magnetic field in-plane but perpendicular to the current carriers can undergo cyclotron motion across the interface, but the orbit is limited by the conducting interface region thickness. So, this mode can provide information about the dimensionality of the interface.

The first finding from Fig. 5.6 is that the magneto-transport is temperature-dependent, anisotropic, and depends strongly on the P_{O_2}. The $P_{O_2} = 10^{-5}$ torr sample has always a positive out-of-plane MR, which becomes immensely large at low temperature; at 2 K, MR = 275%. By bringing the field into the plane of the interface, Figs. 5.6 (b) and (c), that positive MR changes to negative values at low temperature. From Fig. 5.6 (c), it appears that at least two competing mechanisms operate for the in-plane geometry. One, that tries to induce a positive MR, dominates the competition at intermediate temperatures and high fields. From Figs. 5.6 (d), (e) and (f), it can be seen that if the interface is prepared at a higher P_{O_2}, at low temperatures, the MR is negative, regardless of the orientation of the magnetic field with respect to the current. Changes in the sign of the MR strongly appear at intermediate temperatures. Starting at $T = 10$ K, the $MR_{\perp}$ starts to curve upward, and reaches MR = 60% at 20 K. Further increasing the temperature to 30, 50, 70 and 100 K decreases the $MR_{\perp}$ to smaller positive numbers. The temperature region of 10 K $\leq T \leq$ 30

K, where the $MR_{\perp}$ becomes positive, is the temperature range where Hall data become distinctly nonlinear, see Fig. 5.3 (b). One can view the changes in the MR as results of competing mechanisms and/or also of participation of different electron bands. We speculate that the two electron bands, that are discussed in Section 5.4, split strongly over this temperature range and that the electron population in each band scatter differently in the magnetic field. And thus there is variation in the overall behavior of the MR depending on which band dominates.

5.6 PAO/LAO/STO bilayers

One of the hallmarks of the LAO/STO interface is the extreme sensitivity of its transport to electrostatic boundary conditions. This prompted us to study the surface-interface coupling at this amazing interface. To study the effects of the magnetic moment of Pr, and to study the effect of stress in the top layers on the 2DEG at the interface, we prepared a bilayer of PAO and LAO. The bilayer has 9 u.c. of PAO on top of 6 u.c. of LAO: $PAO^{(9)}/LAO^{(6)}/STO$. We compare the magneto-transport results of this sample with a 15-u.c. LAO ($LAO^{(15)}/STO$) and a 15-u.c. PAO ($PAO^{(15)}/STO$) thin film. Figure 5.7 shows the magneto-transport data for the 15 u.c. of LAO on STO that was prepared at $P_{O_2} = 10^{-4}$ torr. The thickness of the film was estimated through an XRR measurement. At this P_{O_2}, PAO thin films tend to show an upturn in resistance at low temperatures, Fig. 5.2 (b); that upturn is absent for the LAO sample. The nonlinearity in Hall data is also obvious for the LAO/STO thin film, see Fig. 5.7 (b). At 2 K, the out-of-plane MR is positive and relatively large, $\sim 70\%$. The presence of negative in-plane MR in Fig. 5.7 (d) for $B \parallel I$, is a signature of spin-dependent magnetic scattering. It tunes out that there is a

critical magnetic field above which the change in MR is more significant. This field occurs at 1 T for the out-of-plane geometry and 2 T for the in-plane geometry. The change in the sign of the MR from positive values for out-of-plane MR, Fig. 5.7 (c), to negative values for in-plane MR, Fig. 5.7 (d), reveals the 2D nature of the interface.

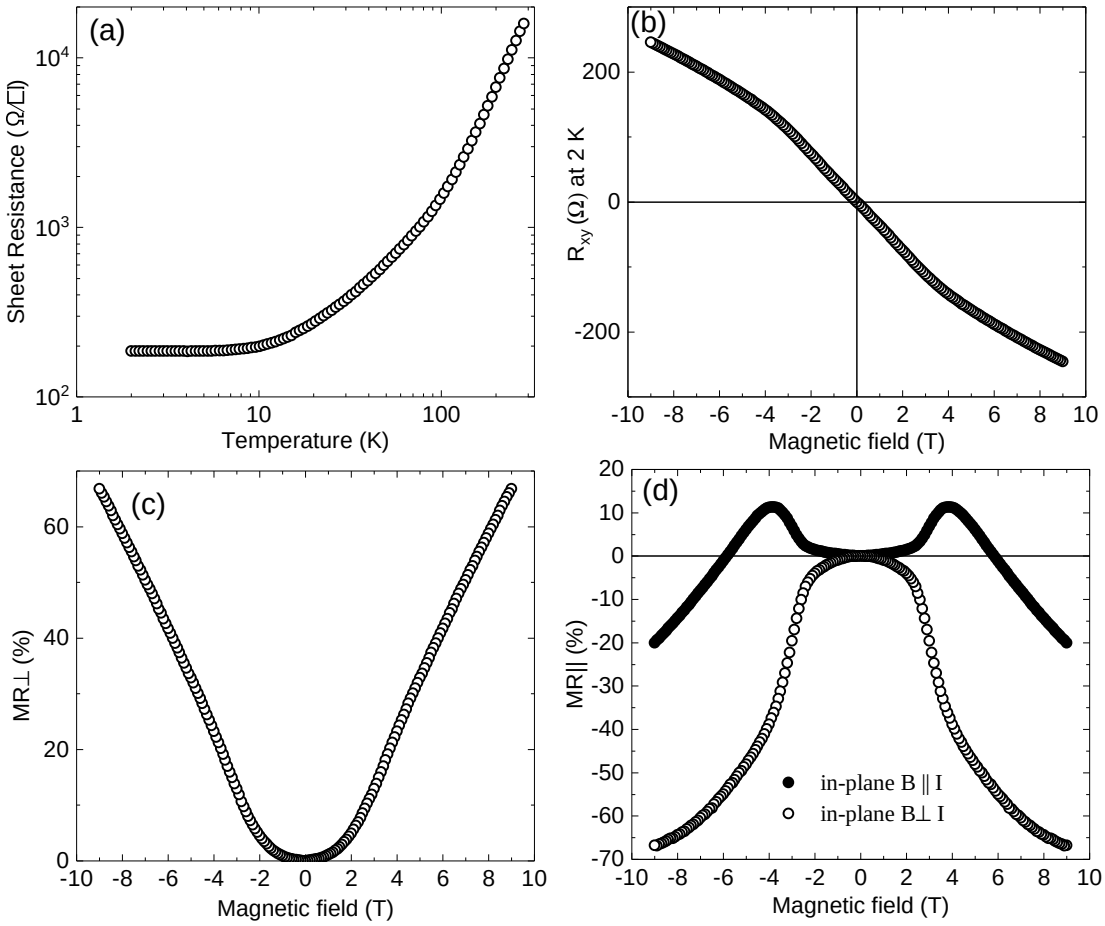

Figure 5.7: Magneto-transport measurements for 15 unit celss of LAO on STO. The thin film was prepared at $P_{O_2} = 10^{-4}$ torr. (a) Sheet resistance as a function of temperature. (b) Hall resistance at 2 K. (c) Out-of-plane magnetoresistance ($MR_{\perp}$) at 2 K. (d) In-plane magnetoresistance ($MR_{\parallel}$) at 2 K, with magnetic field parallel (solid symbols) and perpendicular (open symbols) to the current.

Figure 5.8 shows the magneto-transport data for 9 u.c. of PAO on top of 6 u.c. of LAO on a STO substrate, $PAO^{(9)}/LAO^{(6)}/STO$. The thin films were prepared at $P_{O_2} = 10^{-4}$ torr. The common upturn in resistivity of PAO, Fig. 5.2 (b), is also absent for this sample. It is as if the PAO top layer has no effect on the low temperature behavior of the underlying interface. The slope of the Hall resistance data has become larger than the slope of the Hall resistance for the ($LAO^{(15)}/STO$) interface; this indicates a decrease in the net number of electron carriers. The nonlinearity in the Hall data is also obvious for the $PAO^{(9)}/LAO^{(6)}/STO$ bilayer, see Fig. 5.8 (b). The out-of-plane MR, $\sim 70\%$ at 9 T, is notably larger compared to $LAO^{(15)}/STO$. The signature negative out-of-plane MR at 2 K for PAO thin films, as in Fig. 5.6 (d), does not appear in this bilayer.

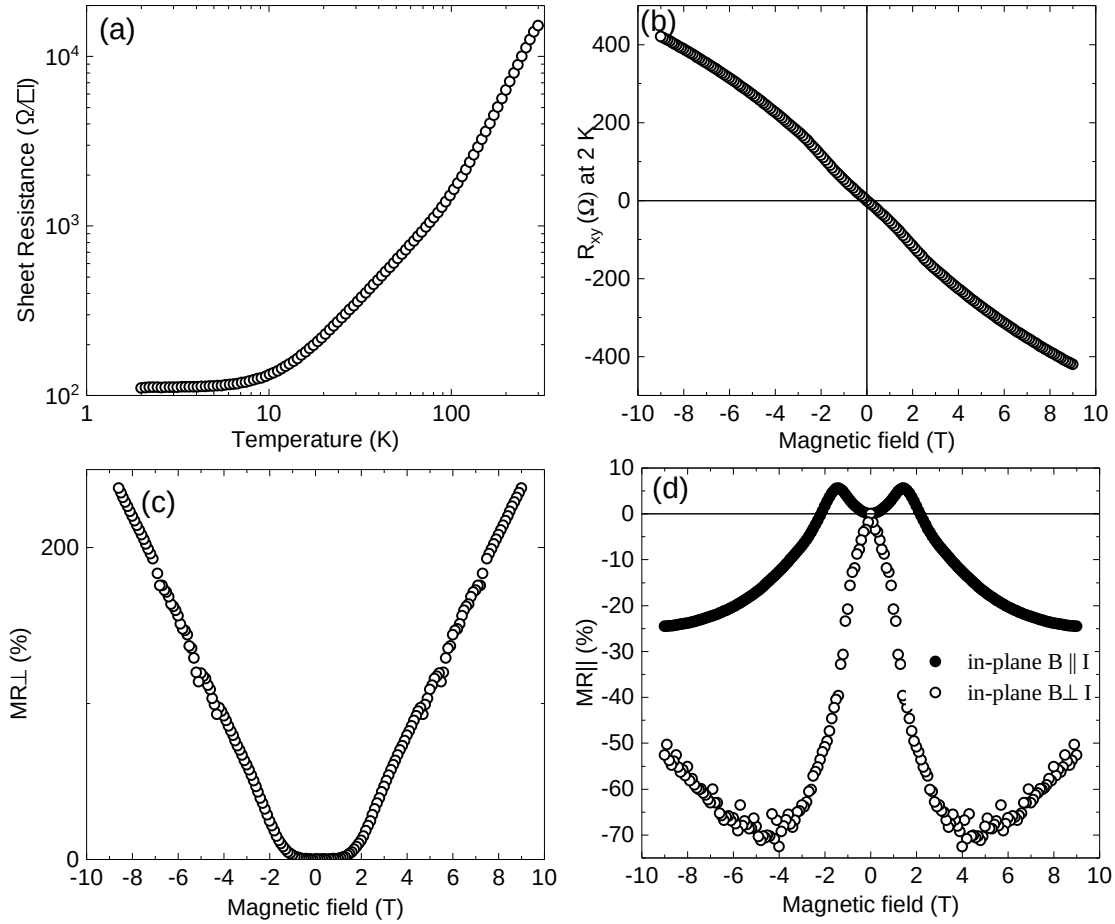

Figure 5.8: magneto-transport measurements for 9 u.c. of PAO on top of 6 u.c. of LAO on STO, PAO$^{(9)}$/LAO$^{(6)}$/STO. The thin films were prepared at $P_{O_2} = 10^{-4}$ torr. (a) Sheet resistance as a function of temperature. (b) Hall resistance at 2 K. (c) Out-of-plane magnetoresistance ($MR_{\perp}$) at 2 K. (d) In-plane magnetoresistance ($MR_{\parallel}$) at 2 K, with magnetic field parallel (solid symbols) and perpendicular (open symbols) to the current.

The magneto-transport results presented here could be compared with the results for the PAO$^{(15)}$/STO interface that was grown at $P_{O_2} = 10^{-4}$ torr previously discussed in Section 5.3. A summary of the comparison data is presented in Fig. 5.9.

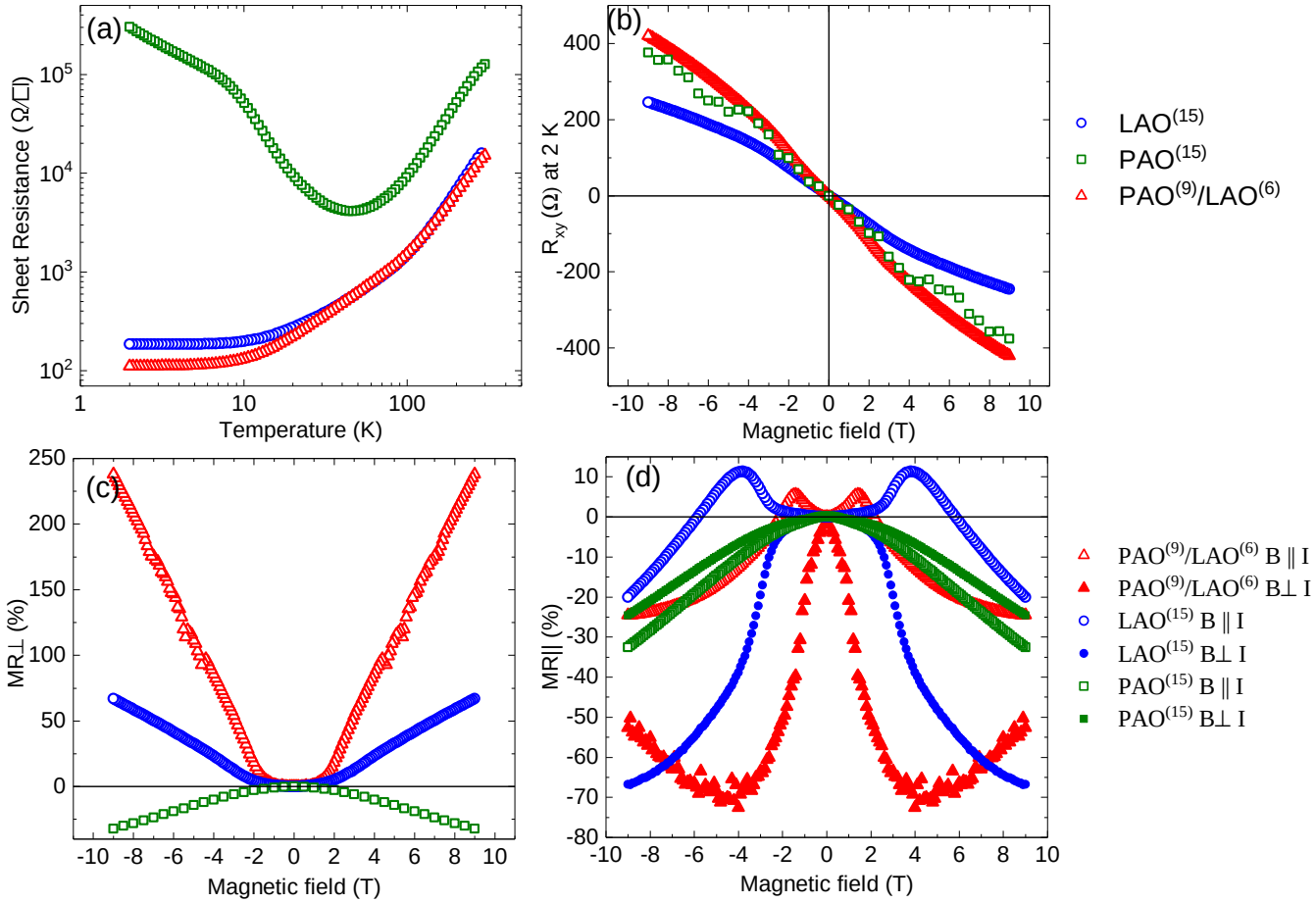

Figure 5.9: (a) Sheet resistance as a function of temperature, (b) Hall resistance at 2 K, (c) out-of-plane magnetoresistance ($MR_{\perp}$) at 2 K, and (d) in-plane magnetoresistance ($MR_{\parallel}$) at 2 K, with magnetic field parallel and perpendicular (empty symbols) to the current for $LAO^{(15)}$/STO, $PAO^{(15)}$/STO, and $PAO^{(9)}/LAO^{(6)}$/STO samples.

Chapter 6

Conclusions and Future Work

6.1 Conclusions

In this thesis, the importance of the Pr substitution for La on the transport properties of the 2DEG at the $LaAlO_3/SrTiO_3$ interface and, also, the effects of oxygen pressure during growth on the $PrAlO_3/SrTiO_3$ interface were studied. Several interfaces of $PrAlO_3/SrTiO_3$ in the P_{O_2} range of 6×10^{-6} – 1×10^{-3} torr were grown, and the transport behaviors were examined. Overall, differences between $PrAlO_3$ and $LaAlO_3$ were subtle, much smaller than the effects of oxygen content changes. These indicate that Pr ions near the interface are predominantly trivalent, with relatively localized magnetism. The most-conducting 2-D-like Pr samples were not as conducting as comparable La samples, indicating either that a steric effect, or a slightly mixed-valent nature of Pr, may be detrimental to conductivity at the interface.

For the 6×10^{-6} torr sample, the very small value of sheet resistance R_s at low temperature, large carrier concentration, high mobilities, and very high positive magnetoresistance values indicate it is like a bulk metal, likely due to extensive oxygen defects and/or interdiffusion. As the interfaces are grown at higher oxygen pressures, resistivity behavior characteristic of nearly two-dimensional transport occurs; for 10^{-5} and 10^{-4} torr, high-temperature metallic behavior with increasing R_s is accompanied by an upturn at low

temperature, consistent with Kondo scattering theory. Analysis of the R_s data gives Kondo temperature $\sim$ 16 K and $\sim$ 18 K for the 10^{-5} and 10^{-4} torr samples, respectively. Positive high MR values are associated with samples where a fraction of carriers are derived from oxygen vacancies. The MR values for the $P_{O_2} \geq 10^{-5}$ torr samples were modeled with their positive part due to WAL because of a strong SO interaction and their negative part due to the Kondo effect. The variation of MR values suggests a strong SO interaction for the 10^{-5} torr sample with $H_{SO} = 1.25$ T in both field orientations. The positive part of the MR shrinks for the 10^{-4} torr sample. For this interface the MR is dominated by negative Kondo MR at high fields.

Nonlinear Hall data at some temperatures were also observed for the interfaces. For the interfaces that are grown at low P_{O_2}, Hall effect data suggest that the transport is dominated by one type of carrier. For the interfaces that are grown at high P_{O_2}, at low and high temperatures, $T < 5$ K and $T > 50$ K, Hall data could be described by a single channel of electron carriers with a low mobility. At intermediate temperatures 10 K $< T <$ 40 K, the Hall data become noticeably nonlinear, with positive out-of-plane and in-plane magnetoresistance. The nonlinear Hall resistances were described in terms of a two-band model, both with electron-charge carriers type, but different densities and mobilities. The multi-band conduction could be the result of the splitting of Ti $3d$ sub-bands, due to the large spin-orbit interaction at the interface.

6.2 Future work

Transition metal oxide interfaces such as $LaAlO_3/SrTiO_3$ interface definitely qualify as one the hot topics of interest, as these materials are gifted with a broad range of significant

electronic properties. These materials often have structural instabilities and complex phase diagrams, which are advantageous for fundamental physics study. The $LaAlO_3/SrTiO_3$ interface has been investigated widely but other related interfaces such as the $PrAlO_3/SrTiO_3$ interface has not been studied as much. A couple of possible studies for this interface are listed below.

6.2.1 Studying the role of magnetic moment of Pr

The Kondo effect originates from the coupling of conduction electrons to virtual bound states of magnetic ions. This coupling manifest itself as an upturn on the resistivity measurements at low temperatures. From the resistivity plot in Fig. 5.9 (a), it can be seen that by substituting Pr for La, below a specific P_{O_2}, the 2DEG experiences a Kondo interaction. One can make a series of thin films of $La_{1-x}Pr_xAlO_3$ with different x values, at $P_{O_2} = 10^{-4}$ torr and study the upturn in resistance as the x value is increased. The origin of the Kondo effect at this interface could be from Ti and/or Pr ions. This study would help to define whether the increased upturn effect at the PAO/STO interface compared to the LAO/STO interface is due to more efficient coupling to Ti, or instead to the additional coupling to Pr ions.

6.2.2 Studying the effect of mechanical pressure on the PAO/STO interface

Mechanical pressure has always been an external parameter to tune the electrical properties of materials. The study of the pressure dependence of transport would help to understand the low-dimensional electron systems better. Experimentally, transport measurements on a buried interface are very challenging. Transport measurements on LAO/STO

heterostructures shows that at 10 K $< T <$ 100 K, where scattering is dominated by impurities, even small pressure strongly affects the transport properties [131]. Applying pressure leads to a strong decrease in μ, and appearance of a minimum in $R_s(T)$ followed by non-metallic behavior and localization at low T. These enhancements in impurity scattering are attributed to the strong suppression of the dielectric permittivity of STO under pressure, which decreases the screening of the scattering centers and leads to incipient localization of charge carriers [131]. One can take advantage of this study and use the pressure cell in our lab to study the 2DEG at PAO/STO interface under pressure. The results of this study would help to understand the mechanism of transport and the origin of the upturn in resistivity at low temperatures.

I have done some preliminary work on how to use our pressure cell to take measurement on thin films, which are as follows. The PAO/STO sample was cut into 3×2 mm^2 to be able to fit into a small chip carrier (MLCC00603), which then fits into the pressure cell. Contacts to the interface were prepared by Al wires attached to the corners of the sample surface using a wire-bonder. To reinforce the Al wires and to keep them in place while the pressure is applied, the whole sample was covered with Stycast 2850 epoxy. Our pressure cell is a clamp-type cell made of beryllium-copper, which enables us to reach pressures up to 20 kbar (2 GPa). We used a 1:1 mixture of isoamyl alcohol and n-pentane as a pressure-transmitting medium, which ensures hydrostatic pressure. The liquid filled a Teflon capsule (about 5 mm diameter and 15 mm length) after having mounted the sample with its surface parallel to the capsule. Fig 6.1 shows the picture of the chip carrier that was used for resistivity measurement under pressure for a PAO/STO interface. The sheet resistance plot as a function of temperature when 0.5 kbar pressure was applied on the sample is shown in

Fig. 6.2.

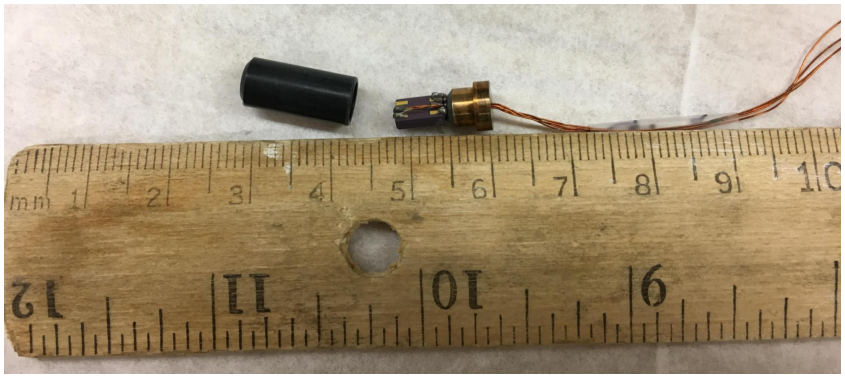

Figure 6.1: Picture of the chip carrier used for resistivity measurement under mechanical pressure for thin films.

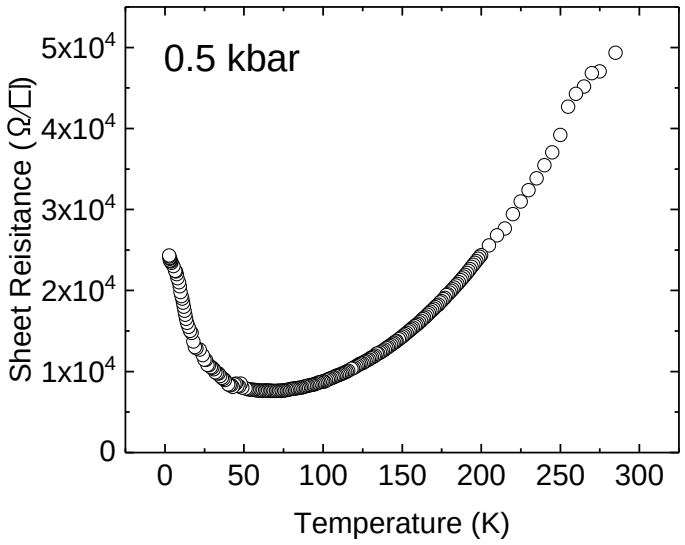

Figure 6.2: Sheet resistance *vs.* temperature for PAO/STO interface for 0.5 kbar applied pressure.

6.2.3 Investigation of the superconductivity at the PAO/STO interface

Despite that superconductivity was discovered for $SrTiO_3$ years ago, the mechanism for electron pairing is still under investigation. What is even more perplexing is the discovery of superconductivity at the LAO/STO interface. The LAO/STO interface is one the rare systems where magnetism and superconductivity coexist. For bulk $PrAlO_3$, superconductivity has not been reported. One can investigate the proper growth conditions for superconductivity in thin films of PAO on STO. Superconductivity probably happens at low P_{O_2} for PAO/STO, where the resistance does not show the upturn at low temperatures.

Recent studies [16, 19] show that the dynamical fluctuations of ferromagnetic layers, such as Ni, deposited on the surface of a topological insulator, Bi, couple to the electrons as a gauge field. The transverse components of that magnetic gauge field can mediate an effective interaction between electrons [132]. The result is a great enhancement in T_c of Bi from 0.5 mK to 4 K. Some of the electronic features of Bi are similar to the 2DEG at the LAO/STO interface, such as low carrier density ($\sim 10^{17}$ cm^{-3}, at 4 K) and large mobility ($\sim 10^7$ cm^{2}V^{-1}s^{-1}, at 4 K). One can explore capping the LAO/STO interface with different thicknesses of ferromagnets such as Ni, Co, Mn, etc., and study the changes in T_c. I have done some preliminary work in our lab for deposition of Ni/LAO/STO. The deposition was done with PLD. The laser energy must be set to some high number ($E > 120$ mJ) in order to ablate the (metallic) Ni target. Figure 6.3 shows the XRD pattern for 6000 pulses of Ni on STO. The substrate temperature was 400°C. The Ni (001) peak at 52° shows success in the deposition of Ni. The XRD pattern for 1200 pulses of Ni on STO and on LAO/STO are also shown in the figure. Fig. 6.5 shows an AFM image for the bilayers of Ni/LAO/STO.

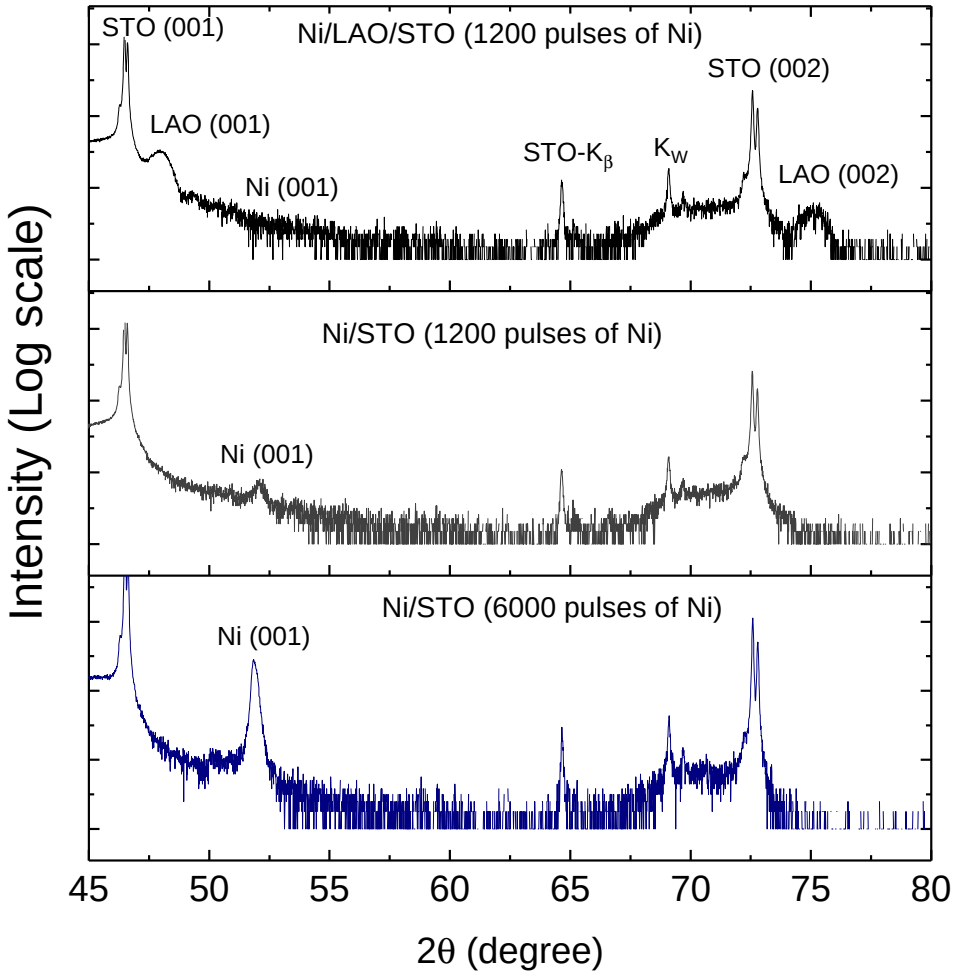

Figure 6.3: XRD spectrum for different numbers of pulses of Ni on STO and on LAO/STO.

The XRR pattern of the Ni/LAO/STO bilayer is shown in Fig. 6.4. For comparison an XRR pattern of a LAO/STO with the same LAO thickness is also shown in the plot. The density of Ni and LAO is 8.9 g/cm^3 and 6.5 g/cm^3, respectively. The oscillations indicate an LAO thickness of 6.5 nm and a combined Ni/LAO thickness of 7.8 nm.

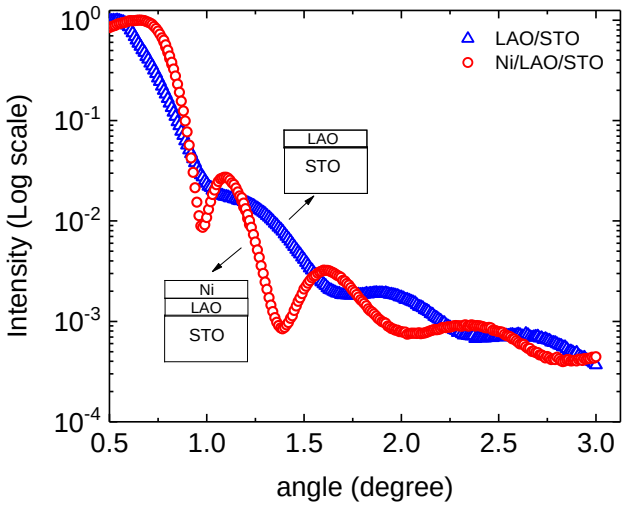

Figure 6.4: XRR patterns for 180 pulses of LAO on STO and 1200 pulses of Ni on the same thickness of LAO on STO.

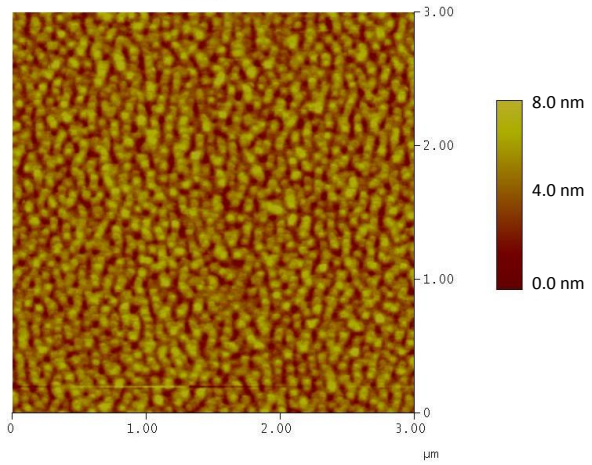

Figure 6.5: AFM image of Ni/LAO/STO

Bibliography

[1] T. IE. *Phys. Z. Sowjetunion*, vol. 1, p. 733, 1932.

[2] W. Shockley, "On the surface states associated with a periodic potential," *Phys. Rev.*, vol. 56, pp. 317–323, Aug 1939.

[3] H. Kroemer, "Nobel lecture: Quasielectric fields and band offsets: teaching electrons new tricks," *Rev. Mod. Phys.*, vol. 73, pp. 783–793, Oct 2001.

[4] A. Gozar, G. Logvenov, L. F. Kourkoutis, A. T. Bollinger, L. A. Giannuzzi, D. A. Muller, and I. Bozovic, "High-temperature interface superconductivity between metallic and insulating copper oxides," *Nature*, vol. 455, pp. 782–785, Oct. 2008.

[5] A. Bhattacharya, S. J. May, S. G. E. te Velthuis, M. Warusawithana, X. Zhai, B. Jiang, J.-M. Zuo, M. R. Fitzsimmons, S. D. Bader, and J. N. Eckstein, "Metal-insulator transition and its relation to magnetic structure in $(\mathrm{lamno_3})_{2n}/(\mathrm{srmno_3})_n$ superlattices," *Phys. Rev. Lett.*, vol. 100, p. 257203, Jun 2008.

[6] J. Liu, M. Kargarian, M. Kareev, B. Gray, P. J. Ryan, A. Cruz, N. Tahir, Y.-D. Chuang, J. Guo, J. M. Rondinelli, J. W. Freeland, G. A. Fiete, and J. Chakhalian, "Heterointerface engineered electronic and magnetic phases of ndnio3 thin films," *Nat. Commun.*, vol. 4, p. 2714, Nov. 2013.

[7] M. N. Baibich, J. M. Broto, A. Fert, F. N. Van Dau, F. Petroff, P. Etienne, G. Creuzet, A. Friederich, and J. Chazelas, "Giant magnetoresistance of (001)fe/(001)cr magnetic superlattices," *Phys. Rev. Lett.*, vol. 61, pp. 2472–2475, Nov 1988.

[8] H. Y. Hwang, Y. Iwasa, M. Kawasaki, B. Keimer, N. Nagaosa, and Y. Tokura, "Emergent phenomena at oxide interfaces," *Nat. Mater.*, vol. 11, pp. 103–113, Feb. 2012.

[9] P. Zubko, S. Gariglio, M. Gabay, P. Ghosez, and J.-M. Triscone, "Interface physics in complex oxide heterostructures," *Annual Review of Condensed Matter Physics*, vol. 2, no. 1, pp. 141–165, 2011.

[10] E. I. Rashba *Sov. Phys. Solid State*, vol. 2, p. 1109, 1960.

[11] Y. A. Bychkov and E. I. Rashba, "Properties of a 2d electron gas with lifted spectral degeneracy," *JETP Lett.*, vol. 39, no. 2, p. 66, 1984.

[12] C. Chappert, A. Fert, and F. N. Van Dau, "The emergence of spin electronics in data storage," *Nat Mater*, vol. 6, pp. 813–823, Nov. 2007.

[13] P. Hofmann, "The surfaces of bismuth: Structural and electronic properties," *Progress in Surface Science*, vol. 81, no. 5, pp. 191 – 245, 2006.

[14] N. Ashcroft and N. Mermin, *Solid State Physics*. Cengage Learning, 2011.

[15] O. Prakash, A. Kumar, A. Thamizhavel, and S. Ramakrishnan, "Evidence for bulk superconductivity in pure bismuth single crystals at ambient pressure," *Science*, 2016.

[16] J. S. Moodera and R. Meservey, "Superconducting phases of bi and ga induced by deposition on a ni sublayer," *Phys. Rev. B*, vol. 42, pp. 179–183, Jul 1990.

[17] Y. M. Koroteev, G. Bihlmayer, E. V. Chulkov, and S. Blügel, "First-principles investigation of structural and electronic properties of ultrathin bi films," *Phys. Rev. B*, vol. 77, p. 045428, Jan 2008.

[18] S. Xiao, D. Wei, and X. Jin, "Bi(111) thin film with insulating interior but metallic surfaces," *Phys. Rev. Lett.*, vol. 109, p. 166805, Oct 2012.

[19] X. Gong, M. Kargarian, A. Stern, D. Yue, H. Zhou, X. Jin, V. M. Galitski, V. M. Yakovenko, and J. Xia, "Time-reversal symmetry-breaking superconductivity in epitaxial bismuth/nickel bilayers," *Science Advances*, vol. 3, no. 3, 2017.

[20] D. P. Norton, B. C. Chakoumakos, J. D. Budai, D. H. Lowndes, B. C. Sales, J. R. Thompson, and D. K. Christen, "Superconductivity in srcuo2-bacuo2 superlattices: Formation of artificially layered superconducting materials," *Science*, vol. 265, no. 5181, pp. 2074–2077, 1994.

[21] A. Ohtomo and H. Y. Hwang, "A high-mobility electron gas at the laalo3/srtio3 heterointerface," *Nature*, vol. 427, pp. 423–426, 1 2004.

[22] N. Reyren, S. Thiel, A. D. Caviglia, L. F. Kourkoutis, G. Hammerl, C. Richter, C. W. Schneider, T. Kopp, A.-S. Rüetschi, D. Jaccard, M. Gabay, D. A. Muller, J.-M. Triscone, and J. Mannhart, "Superconducting interfaces between insulating oxides," *Science*, vol. 317, no. 5842, pp. 1196–1199, 2007.

[23] M. Salluzzo, S. Gariglio, D. Stornaiuolo, V. Sessi, S. Rusponi, C. Piamonteze, G. M. De Luca, M. Minola, D. Marré, A. Gadaleta, H. Brune, F. Nolting, N. B. Brookes,

and G. Ghiringhelli, "Origin of interface magnetism in $bimno_3/srtio_3$ and $laalo_3/srtio_3$ heterostructures," *Phys. Rev. Lett.*, vol. 111, p. 087204, Aug 2013.

[24] A. D. Caviglia, S. Gariglio, N. Reyren, D. Jaccard, T. Schneider, M. Gabay, S. Thiel, G. Hammerl, J. Mannhart, and J.-M. Triscone, "Electric field control of the laalo3/srtio3 interface ground state," *Nature*, vol. 456, pp. 624–627, Dec. 2008.

[25] N. Nakagawa, H. Y. Hwang, and D. A. Muller, "Why some interfaces cannot be sharp," *Nat. Mater.*, vol. 5, pp. 204–209, Mar. 2006.

[26] P. R. Willmott, S. A. Pauli, R. Herger, C. M. Schlepütz, D. Martoccia, B. D. Patterson, B. Delley, R. Clarke, D. Kumah, C. Cionca, and Y. Yacoby, "Structural basis for the conducting interface between $laalo_3$ and $srtio_3$," *Phys. Rev. Lett.*, vol. 99, p. 155502, Oct 2007.

[27] G. Herranz, M. Basletić, M. Bibes, C. Carrétéro, E. Tafra, E. Jacquet, K. Bouzehouane, C. Deranlot, A. Hamzić, J.-M. Broto, A. Barthélémy, and A. Fert, "High mobility in $laalo_3/srtio_3$ heterostructures: Origin, dimensionality, and perspectives," *Phys. Rev. Lett.*, vol. 98, p. 216803, May 2007.

[28] Y. Fujishima, Y. Tokura, T. Arima, and S. Uchida, "Optical-conductivity spectra of $sr_{1-x}la_xtio_3$: Filling-dependent effect of the electron correlation," *Phys. Rev. B*, vol. 46, pp. 11167–11170, Nov 1992.

[29] A. Kalabukhov, R. Gunnarsson, J. Börjesson, E. Olsson, T. Claeson, and D. Winkler, "Effect of oxygen vacancies in the $srtio_3$ substrate on the electrical properties of the $laalo_3/srtio_3$ interface," *Phys. Rev. B*, vol. 75, p. 121404, Mar 2007.

[30] W. Siemons, G. Koster, H. Yamamoto, W. A. Harrison, G. Lucovsky, T. H. Geballe, D. H. A. Blank, and M. R. Beasley, "Origin of charge density at laalo$_3$ on srtio$_3$ heterointerfaces: Possibility of intrinsic doping," *Phys. Rev. Lett.*, vol. 98, p. 196802, May 2007.

[31] H. O. Jeschke, J. Shen, and R. Valenti, "Localized versus itinerant states created by multiple oxygen vacancies in srtio 3," *New Journal of Physics*, vol. 17, no. 2, p. 023034, 2015.

[32] M. Behrmann and F. Lechermann, "Interface exchange processes in laalo$_3$/Srtio$_3$ induced by oxygen vacancies," *Phys. Rev. B*, vol. 92, p. 125148, Sep 2015.

[33] Z. Q. Liu, C. J. Li, W. M. Lü, X. H. Huang, Z. Huang, S. W. Zeng, X. P. Qiu, L. S. Huang, A. Annadi, J. S. Chen, J. M. D. Coey, T. Venkatesan, and Ariando, "Origin of the two-dimensional electron gas at laalo$_3$/srtio$_3$ interfaces: The role of oxygen vacancies and electronic reconstruction," *Phys. Rev. X*, vol. 3, p. 021010, May 2013.

[34] Y. Chen, N. Pryds, J. E. Kleibeuker, G. Koster, J. Sun, E. Stamate, B. Shen, G. Rijnders, and S. Linderoth, "Metallic and insulating interfaces of amorphous srtio3-based oxide heterostructures," *Nano Letters*, vol. 11, no. 9, pp. 3774–3778, 2011.

[35] G. Grosso and G. P. Parravicini, *Solid State Physics*. Academic Press, 2000.

[36] R. J. D. Tilley, *Perovskites: Structure-Property Relationships*. John Wiley & Sons, Ltd, 2016.

[37] T. Hidaka and K. Oka, "Isotope effect on batio$_3$ ferroelectric phase transitions," *Phys. Rev. B*, vol. 35, pp. 8502–8508, Jun 1987.

[38] P. B. Allen, H. Berger, O. Chauvet, L. Forro, T. Jarlborg, A. Junod, B. Revaz, and G. Santi, "Transport properties, thermodynamic properties, and electronic structure of srruo$_3$," *Phys. Rev. B*, vol. 53, pp. 4393–4398, Feb 1996.

[39] R. Aleonard, R. Pauthenet, J. P. Rebouillat, and C. Veyret, "Interpretation of the magnetic properties of the rare earth chromites and the rare earth manganites," *Journal of Applied Physics*, vol. 39, no. 2, pp. 379–379, 1968.

[40] P. A. Lee, N. Nagaosa, and X.-G. Wen, "Doping a mott insulator: Physics of high-temperature superconductivity," *Rev. Mod. Phys.*, vol. 78, pp. 17–85, Jan 2006.

[41] J. R. Cooper, B. Alavi, L.-W. Zhou, W. P. Beyermann, and G. Grüner, "Thermoelectric power of some high-T_c oxides," *Phys. Rev. B*, vol. 35, pp. 8794–8796, Jun 1987.

[42] R. J. D. Tilley, "Perovskites: Structure-property relationships," *Wiley, 2016.*

[43] K. A. Müller, W. Berlinger, and F. Waldner, "Characteristic structural phase transition in perovskite-type compounds," *Phys. Rev. Lett.*, vol. 21, pp. 814–817, Sep 1968.

[44] L. Rimai and G. A. deMars, "Electron paramagnetic resonance of trivalent gadolinium ions in strontium and barium titanates," *Phys. Rev.*, vol. 127, pp. 702–710, Aug 1962.

[45] W. Luo, W. Duan, S. G. Louie, and M. L. Cohen, "Structural and electronic properties of n-doped and p-doped SrTio$_3$," *Phys. Rev. B*, vol. 70, p. 214109, Dec 2004.

[46] H. P. R. Frederikse, W. R. Thurber, and W. R. Hosler, "Electronic transport in strontium titanate," *Phys. Rev.*, vol. 134, pp. A442–A445, Apr 1964.

[47] K. van Benthem, C. Elsysser, and R. H. French, "Bulk electronic structure of srtio3: Experiment and theory," *Journal of Applied Physics*, vol. 90, no. 12, pp. 6156–6164, 2001.

[48] L. F. Mattheiss, "Energy bands for $knif_3$, $srtio_3$, $kmoo_3$, and $ktao_3$," *Phys. Rev. B*, vol. 6, pp. 4718–4740, Dec 1972.

[49] H. B. Horst Kppel, David R. Yarkony, "The jahn-teller effect-fundamentals and implications for physics and chemistry," *Springer Berlin, Heidelberg, 2009.*

[50] C. S. Koonce, M. L. Cohen, J. F. Schooley, W. R. Hosler, and E. R. Pfeiffer, "Superconducting transition temperatures of semiconducting $srtio_3$," *Phys. Rev.*, vol. 163, pp. 380–390, Nov 1967.

[51] O. N. Tufte and P. W. Chapman, "Electron mobility in semiconducting strontium titanate," *Phys. Rev.*, vol. 155, pp. 796–802, Mar 1967.

[52] K. A. G. Jr., J.-C. G. Bnzli, and V. K. Pecharsky, "Handbook on the physics and chemistry of rare earths," vol. 39, pp. v – viii, Elsevier, 2009.

[53] C. Mitra, C. Lin, J. Robertson, and A. A. Demkov, "Electronic structure of oxygen vacancies in $srtio_3$ and $laalo_3$," *Phys. Rev. B*, vol. 86, p. 155105, Oct 2012.

[54] S.-G. Lim, S. Kriventsov, T. N. Jackson, J. H. Haeni, D. G. Schlom, A. M. Balbashov, R. Uecker, P. Reiche, J. L. Freeouf, and G. Lucovsky, "Dielectric functions and optical bandgaps of high-k dielectrics for metal-oxide-semiconductor field-effect transistors by far ultraviolet spectroscopic ellipsometry," *Journal of Applied Physics*, vol. 91, no. 7, pp. 4500–4505, 2002.

[55] E. Cohen, L. A. Risberg, W. A. Nordland, R. D. Burbank, R. C. Sherwood, and L. G. Van Uitert, "Structural phase transitions in pralo$_3$," *Phys. Rev.*, vol. 186, pp. 476–478, Oct 1969.

[56] M. Wencka, S. Vrtnik, M. Jagodič, Z. Jagličić, S. Turczynski, D. A. Pawlak, and J. Dolinšek, "Observation of anomalous magnetism in the low-temperature monoclinic phase of single-crystalline pralo$_3$ perovskite," *Phys. Rev. B*, vol. 80, p. 224410, Dec 2009.

[57] T. Fix, F. Schoofs, Z. Bi, A. Chen, H. Wang, J. L. MacManus-Driscoll, and M. G. Blamire, "Influence of srtio3 substrate miscut angle on the transport properties of laalo3/srtio3 interfaces," *Applied Physics Letters*, vol. 99, no. 2, p. 022103, 2011.

[58] P. Brinks, W. Siemons, J. E. Kleibeuker, G. Koster, G. Rijnders, and M. Huijben, "Anisotropic electrical transport properties of a two-dimensional electron gas at srtio3laalo3 interfaces," *Applied Physics Letters*, vol. 98, no. 24, p. 242904, 2011.

[59] M. Huijben, A. Brinkman, G. Koster, G. Rijnders, H. Hilgenkamp, and D. H. A. Blank *Advanced Materials*, vol. 21, no. 17, pp. 1665–1677, 2009.

[60] A. F. Santander-Syro, O. Copie, T. Kondo, F. Fortuna, S. Pailhes, R. Weht, X. G. Qiu, F. Bertran, A. Nicolaou, A. Taleb-Ibrahimi, P. Le Fevre, G. Herranz, M. Bibes, N. Reyren, Y. Apertet, P. Lecoeur, A. Barthelemy, and M. J. Rozenberg, "Two-dimensional electron gas with universal subbands at the surface of srtio3," *Nature*, vol. 469, pp. 189–193, Jan. 2011.

[61] G. Herranz, F. Svnchez, N. Dix, M. Scigaj, and J. Fontcuberta, "High mobility conduction at (110) and (111) laalo3/srtio3 interfaces," vol. 2, p. 758, Oct. 2012.

[62] G. A. Baraff, J. A. Appelbaum, and D. R. Hamann, "Self-consistent calculation of the electronic structure at an abrupt gaas-ge interface," *Phys. Rev. Lett.*, vol. 38, pp. 237–240, Jan 1977.

[63] S. Thiel, G. Hammerl, A. Schmehl, C. W. Schneider, and J. Mannhart, "Tunable quasi-two-dimensional electron gases in oxide heterostructures," *Science*, vol. 313, no. 5795, pp. 1942–1945, 2006.

[64] A. Jost, V. K. Guduru, S. Wiedmann, J. C. Maan, U. Zeitler, S. Wenderich, A. Brinkman, and H. Hilgenkamp, "Transport and thermoelectric properties of the $laalo_3/srtio_3$ interface," *Phys. Rev. B*, vol. 91, p. 045304, Jan 2015.

[65] G. Herranz, M. Basletić, M. Bibes, C. Carrétéro, E. Tafra, E. Jacquet, K. Bouzehouane, C. Deranlot, A. Hamzić, J.-M. Broto, A. Barthélémy, and A. Fert, "High mobility in $laalo_3/srtio_3$ heterostructures: Origin, dimensionality, and perspectives," *Phys. Rev. Lett.*, vol. 98, p. 216803, May 2007.

[66] C. Cantoni, J. Gazquez, F. Miletto Granozio, M. P. Oxley, M. Varela, A. R. Lupini, S. J. Pennycook, C. Aruta, U. S. di Uccio, P. Perna, and D. Maccariello, "Electron transfer and ionic displacements at the origin of the 2d electron gas at the lao/sto interface: Direct measurements with atomic-column spatial resolution," *Advanced Materials*, vol. 24, no. 29, pp. 3952–3957, 2012.

[67] P. R. Willmott, S. A. Pauli, R. Herger, C. M. Schlepütz, D. Martoccia, B. D. Patterson, B. Delley, R. Clarke, D. Kumah, C. Cionca, and Y. Yacoby, "Structural basis for the conducting interface between laalo$_3$ and srtio$_3$," *Phys. Rev. Lett.*, vol. 99, p. 155502, Oct 2007.

[68] T. Fix, J. L. MacManus-Driscoll, and M. G. Blamire, "Delta-doped laalo3/srtio3 interfaces," *Applied Physics Letters*, vol. 94, no. 17, p. 172101, 2009.

[69] A. Brinkman, M. Huijben, M. van Zalk, J. Huijben, U. Zeitler, J. Maan, W. Wiel, G. Rijnders, D. Blank, and H. Hilgenkamp, "Magnetic effects at the interface between non-magnetic oxides," vol. 6, pp. 493–6, 08 2007.

[70] L. Li, C. Richter, J. Mannhart, and R. C. Ashoori, "Coexistence of magnetic order and two-dimensional superconductivity atalaalo3/srtio3 interfaces," vol. 7, p. 762, Sept. 2011.

[71] J. A. Bert, B. Kalisky, C. Bell, M. Kim, Y. Hikita, H. Y. Hwang, and K. A. Moler, "Direct imaging of the coexistence of ferromagnetism and superconductivity atathealaalo3/srtio3 interface," vol. 7, p. 767, Sept. 2011.

[72] J.-S. Lee, Y. W. Xie, H. K. Sato, C. Bell, Y. Hikita, H. Y. Hwang, and C.-C. Kao, "Titanium dxy ferromagnetism at the laalo3/srtio3ainterface," *Nat Mater*, vol. 12, pp. 703–706, Aug. 2013.

[73] N. Reyren, S. Gariglio, A. D. Caviglia, D. Jaccard, T. Schneider, and J.-M. Triscone, "Anisotropy of the superconducting transport properties of the laalo3/srtio3 interface," *Applied Physics Letters*, vol. 94, no. 11, p. 112506, 2009.

[74] H. Jeffrey Gardner, A. Kumar, L. Yu, P. Xiong, M. P. Warusawithana, L. Wang, O. Vafek, and D. G. Schlom, "Enhancement of superconductivity by a parallel magnetic field in two-dimensional superconductors," vol. 7, p. 895, Aug. 2011.

[75] S. N. Klimin, J. Tempere, J. T. Devreese, and D. van der Marel, "Interface superconductivity in $laalo_3 - srtio_3$ heterostructures," *Phys. Rev. B*, vol. 89, p. 184514, May 2014.

[76] C. Stephanos, T. Kopp, J. Mannhart, and P. J. Hirschfeld, "Interface-induced d-wave pairing," *Phys. Rev. B*, vol. 84, p. 100510, Sep 2011.

[77] M. S. Scheurer and J. Schmalian, "Topological superconductivity and unconventional pairing in oxide interfaces," vol. 6, p. 6005, Jan. 2015.

[78] R. Winkler, *Spin Orbit Coupling Effects in Two-Dimensional Electron and Hole Systems*. Springer, New York, 2003.

[79] G. Dresselhaus, "Spin-orbit coupling effects in zinc blende structures," *Phys. Rev.*, vol. 100, pp. 580–586, Oct 1955.

[80] Z. Zhong, A. Tóth, and K. Held, "Theory of spin-orbit coupling at $laalo_3/srtio_3$ interfaces and $srtio_3$ surfaces," *Phys. Rev. B*, vol. 87, p. 161102, Apr 2013.

[81] H. Uwe, T. Sakudo, and H. Yamaguchi, "Interband electronic raman scattering in srtio3," *Japanese Journal of Applied Physics*, vol. 24, no. S2, p. 519, 1985.

[82] Y. J. Chang, A. Bostwick, Y. S. Kim, K. Horn, and E. Rotenberg, "Structure and correlation effects in semiconducting $srtio_3$," *Phys. Rev. B*, vol. 81, p. 235109, Jun 2010.

[83] M. Marques, L. K. Teles, V. Anjos, L. M. R. Scolfaro, J. R. Leite, V. N. Freire, G. A. Farias, and E. F. da Silva Jr., "Full-relativistic calculations of the srtio3 carrier effective masses and complex dielectric function," *Applied Physics Letters*, vol. 82, no. 18, pp. 3074–3076, 2003.

[84] Y. Kim, R. M. Lutchyn, and C. Nayak, "Origin and transport signatures of spin-orbit interactions in one- and two-dimensional $srtio_3$-based heterostructures," *Phys. Rev. B*, vol. 87, p. 245121, Jun 2013.

[85] J. A. Sulpizio, S. Ilani, P. Irvin, and J. Levy, "Nanoscale phenomena in oxide heterostructures," *Annual Review of Materials Research*, vol. 44, no. 1, pp. 117–149, 2014.

[86] A. D. Caviglia, M. Gabay, S. Gariglio, N. Reyren, C. Cancellieri, and J.-M. Triscone, "Tunable rashba spin-orbit interaction at oxide interfaces," *Phys. Rev. Lett.*, vol. 104, p. 126803, Mar 2010.

[87] Y. Kim, R. M. Lutchyn, and C. Nayak, "Origin and transport signatures of spin-orbit interactions in one- and two-dimensional $srtio_3$-based heterostructures," *Phys. Rev. B*, vol. 87, p. 245121, Jun 2013.

[88] P. A. Lee and T. V. Ramakrishnan, "Disordered electronic systems," *Rev. Mod. Phys.*, vol. 57, pp. 287–337, Apr 1985.

[89] F. Evers and A. D. Mirlin, "Anderson transitions," *Rev. Mod. Phys.*, vol. 80, pp. 1355–1417, Oct 2008.

[90] P. W. Anderson, E. Abrahams, and T. V. Ramakrishnan, "Possible explanation of nonlinear conductivity in thin-film metal wires," *Phys. Rev. Lett.*, vol. 43, pp. 718–720, Sep 1979.

[91] A. I. L. L. P. Gorkov and D. Khmelnitzkii, "Particle conductivity in a two-dimentsional random potential," *Pis'ma Zh. Eksp. Teor. Fiz. 30 (1979) 248; JETP Lett. 30 (1979) 228.*

[92] H.-Z. Lu and S.-Q. Shen, "Finite-temperature conductivity and magnetoconductivity of topological insulators," *Phys. Rev. Lett.*, vol. 112, p. 146601, Apr 2014.

[93] D. Kim, P. Syers, N. P. Butch, J. Paglione, and M. S. Fuhrer, "Coherent topological transport on the surface of bi2se3," vol. 4, p. 2040, June 2013.

[94] K.-I. Imura, Y. Kuramoto, and K. Nomura, "Weak localization properties of the doped Z_2 topological insulator," *Phys. Rev. B*, vol. 80, p. 085119, Aug 2009.

[95] R. J. Elliott, "Theory of the effect of spin-orbit coupling on magnetic resonance in some semiconductors," *Phys. Rev.*, vol. 96, pp. 266–279, Oct 1954.

[96] Y. Yafet *Solid State Physics (Academic, New York, 1963).*

[97] P. G. Elliot *Sov. Phys. Solid State*, vol. 13, p. 3023, 1971.

[98] S. Maekawa and H. F. , "Magnetoresistance in two-dimensional disordered systems: Effects of zeeman splitting and spin-orbit scattering," *Journal of the Physical Society of Japan*, vol. 50, pp. 2516–2524, 1981.

[99] S. Hikami, A. I. Larkin, and Y. Nagaoka, "Spin-orbit interaction and magnetoresistance in the two dimensional random system," *Prog. Theor. Phys.*, vol. 63, no. 2, p. 707, 1980.

[100] Y. B. L.-G. S. V. Iordanskii and G. E. Pikus, "Weak localization in quantum wells with spin-orbit interaction," *Soviet Journal of Experimental and Theoretical Physics Letters*, vol. 60, p. 206, 1994.

[101] H. Nakamura, T. Koga, and T. Kimura, "Experimental evidence of cubic rashba effect in an inversion-symmetric oxide," *Phys. Rev. Lett.*, vol. 108, p. 206601, May 2012.

[102] M. Lee, J. R. Williams, S. Zhang, C. D. Frisbie, and D. Goldhaber-Gordon, "Electrolyte gate-controlled kondo effect in srtio$_3$," *Phys. Rev. Lett.*, vol. 107, p. 256601, Dec 2011.

[103] G. M. De Luca, R. Di Capua, E. Di Gennaro, F. M. Granozio, D. Stornaiuolo, M. Salluzzo, A. Gadaleta, I. Pallecchi, D. Marrè, C. Piamonteze, M. Radovic, Z. Ristic, and S. Rusponi, "Transport properties of a quasi-two-dimensional electron system formed in laalo$_3$/eutio$_3$/srtio$_3$ heterostructures," *Phys. Rev. B*, vol. 89, p. 224413, Jun 2014.

[104] S. Das, A. Rastogi, L. Wu, J.-C. Zheng, Z. Hossain, Y. Zhu, and R. C. Budhani, "Kondo scattering in δ-doped latio$_3$/srtio$_3$ interfaces: Renormalization by spin-orbit interactions," *Phys. Rev. B*, vol. 90, p. 081107, Aug 2014.

[105] M. Diez, A. M. R. V. L. Monteiro, G. Mattoni, E. Cobanera, T. Hyart, E. Mulazimoglu, N. Bovenzi, C. W. J. Beenakker, and A. D. Caviglia, "Giant negative magnetoresistance driven by spin-orbit coupling at the laalo$_3$/srtio$_3$ interface," *Phys. Rev. Lett.*, vol. 115, p. 016803, Jul 2015.

[106] K. X. Jin, W. Lin, B. C. Luo, and T. Wu, "Photoinduced modulation and relaxation characteristics in laalo3/srtio3 heterointerface," vol. 5, p. 8778, Mar. 2015.

[107] G. K. H. Douglas B. Chrisey, *Pulsed Laser Deposition of Thin Films*. John Wiley & Sons, Ltd, 1994.

[108] Y. Ota, *Growth Study of Cuprate Thin Films by PLD*. Master's thesis, The University of Tokyo, 2010.

[109] M. Kawasaki, K. Takahashi, T. Maeda, R. Tsuchiya, M. Shinohara, O. Ishiyama, T. Yonezawa, M. Yoshimoto, and H. Koinuma, "Atomic control of the srtio3 crystal surface," *Science*, vol. 266, no. 5190, pp. 1540–1542, 1994.

[110] J. G. Connell, B. J. Isaac, G. B. Ekanayake, D. R. Strachan, and S. S. A. Seo, "Preparation of atomically flat srtio3 surfaces using a deionized-water leaching and thermal annealing procedure," *Applied Physics Letters*, vol. 101, no. 25, p. 251607, 2012.

[111] G. Koster, G. Rijnders, D. H. Blank, and H. Rogalla, "Surface morphology determined by (001) single-crystal srtio3 termination," *Physica C: Superconductivity*, vol. 339, no. 4, pp. 215 – 230, 2000.

[112] L. J. van der Pauw, "A method of meansuring the resistivity and hall coefficient on lamellate of arbitrary shape," *Phillips Technical Review*, vol. 20, pp. 220–224, 1959.

[113] A. Annadi, A. Putra, Z. Q. Liu, X. Wang, K. Gopinadhan, Z. Huang, S. Dhar, T. Venkatesan, and Ariando, "Electronic correlation and strain effects at the interfaces between polar and nonpolar complex oxides," *Phys. Rev. B*, vol. 86, p. 085450, Aug 2012.

[114] C. Bell, S. Harashima, Y. Hikita, and H. Y. Hwang, "Thickness dependence of the mobility at the laalo3/srtio3 interface," *Applied Physics Letters*, vol. 94, no. 22, 2009.

[115] T. A. Costi, A. C. Hewson, and V. Zlatic, "Transport coefficients of the anderson model via the numerical renormalization group," *Journal of Physics: Condensed Matter*, vol. 6, no. 13, p. 2519, 1994.

[116] D. Goldhaber-Gordon, J. Göres, M. A. Kastner, H. Shtrikman, D. Mahalu, and U. Meirav, "From the kondo regime to the mixed-valence regime in a single-electron transistor," *Phys. Rev. Lett.*, vol. 81, pp. 5225–5228, Dec 1998.

[117] A. Annadi, A. Putra, A. Srivastava, X. Wang, Z. Huang, Z. Q. Liu, T. Venkatesan, and Ariando, "Evolution of variable range hopping in strongly localized two dimensional electron gas at ndalo3/srtio3 (100) heterointerfaces," *Applied Physics Letters*, vol. 101, no. 23, 2012.

[118] A. David, Y. Tian, P. Yang, X. Gao, W. Lin, A. B. Shah, J.-M. Zuo, W. Prellier, and T. Wu, "Colossal positive magnetoresistance in surface-passivated oxygen-deficient strontium titanite," *Scientific Reports*, vol. 5, pp. 10255–, May 2015.

[119] X. Wang, W. M. Lü, A. Annadi, Z. Q. Liu, K. Gopinadhan, S. Dhar, T. Venkatesan, and Ariando, "Magnetoresistance of two-dimensional and three-dimensional electron gas in $laalo_3/srtio_3$ heterostructures: Influence of magnetic ordering, interface scattering, and dimensionality," *Phys. Rev. B*, vol. 84, p. 075312, Aug 2011.

[120] B. Grbić, R. Leturcq, T. Ihn, K. Ensslin, D. Reuter, and A. D. Wieck, "Strong spin-orbit interactions and weak antilocalization in carbon-doped p-type GaAs/$al_xga_{1-x}As$

heterostructures," *Phys. Rev. B*, vol. 77, p. 125312, Mar 2008.

[121] X.-L. Qi and S.-C. Zhang, "Topological insulators and superconductors," *Rev. Mod. Phys.*, vol. 83, pp. 1057–1110, Oct 2011.

[122] S.-P. Chiu and J.-J. Lin, "Weak antilocalization in topological insulator bi_2te_3 microflakes," *Phys. Rev. B*, vol. 87, p. 035122, Jan 2013.

[123] C. Beenakker and H. van Houten, "Quantum transport in semiconductor nanostructures," *Solid State Physics*, vol. 44, p. 1, 1991.

[124] N. Andrei, K. Furuya, and J. H. Lowenstein, "Solution of the kondo problem," *Rev. Mod. Phys.*, vol. 55, pp. 331–402, Apr 1983.

[125] C. J. Lin, X. Y. He, J. Liao, X. X. Wang, V. S. IV, W. M. Yang, T. Guan, Q. M. Zhang, L. Gu, G. Y. Zhang, C. G. Zeng, X. Dai, K. H. Wu, and Y. Q. Li, "Parallel field magnetoresistance in topological insulator thin films," *Phys. Rev. B*, vol. 88, p. 041307, Jul 2013.

[126] A. G. Mal'shukov, K. A. Chao, and M. Willander, "Magnetoresistance of a weakly disordered iii-v semiconductor quantum well in a magnetic field parallel to interfaces," *Phys. Rev. B*, vol. 56, pp. 6436–6439, Sep 1997.

[127] S. Mozaffari, S. Guchhait, and J. T. Markert, "Spinorbit interaction and kondo scattering at the pralo 3 /srtio 3 interface: effects of oxygen content," *Journal of Physics: Condensed Matter*, vol. 29, no. 39, p. 395002, 2017.

[128] M. Ben Shalom, A. Ron, A. Palevski, and Y. Dagan, "Shubnikov˘de haas oscillations in $srtio_3/laalo_3$ interface," *Phys. Rev. Lett.*, vol. 105, p. 206401, Nov 2010.

[129] A. Jost, V. K. Guduru, S. Wiedmann, J. C. Maan, U. Zeitler, S. Wenderich, A. Brinkman, and H. Hilgenkamp, "Transport and thermoelectric properties of the $laalo_3/srtio_3$ interface," *Phys. Rev. B*, vol. 91, p. 045304, Jan 2015.

[130] V. K. Guduru, A. McCollam, A. Jost, S. Wenderich, H. Hilgenkamp, J. C. Maan, A. Brinkman, and U. Zeitler, "Thermally excited multiband conduction in $laalo_3/srtio_3$ heterostructures exhibiting magnetic scattering," *Phys. Rev. B*, vol. 88, p. 241301, Dec 2013.

[131] D. Fuchs, A. Sleem, R. Schäfer, A. G. Zaitsev, M. Meffert, D. Gerthsen, R. Schneider, and H. v. Löhneysen, "Incipient localization of charge carriers in the two-dimensional electron system in $LaAlo_3/SrTio_3$ under hydrostatic pressure," *Phys. Rev. B*, vol. 92, p. 155313, Oct 2015.

[132] M. Kargarian, D. K. Efimkin, and V. Galitski, "Amperean pairing at the surface of topological insulators," *Phys. Rev. Lett.*, vol. 117, p. 076806, Aug 2016.

Vita

Shirin Mozaffari was born in Tehran, Iran to Nosrat Bayati and Naser Mozaffari. She attended the University of Tehran until the August of 2004, where she obtained a Bachelor of Science in Physics. During her undergraduate studies, she was surrounded by an amazing support group of friends, with whom she enjoyed climbing some of the highest mountains in Iran, multiple times. She then attended Sharif University of Technology and obtained a Master's degree in Physics with special focus in Condensed Matter Physics under the direction of Professor Mohammad Akhavan, where she got familiar with the field of superconductivity. In the fall of 2011, she began her Ph.D. in the field of Condensed Matter Physics at the University of Texas at Austin under the supervision of Professor John T. Markert. Her Ph.D. work was focused on the field of oxide interfaces. After graduation, she will move to Tallahassee, Florida, for a postdoctoral studies with Dr. Luis Balicas.

Permanent address: mozaffari.shirin@gmail.com;
mozaffari@physics.utexas.edu

This dissertation was typeset with LaTeX[†] by the author.

[†]LaTeX is a document preparation system developed by Leslie Lamport as a special version of Donald Knuth's TeX Program.